DISS. ETH No. 18593

TRACEABLE S-PARAMETER MEASUREMENTS IN COAXIAL TRANSMISSION LINES UP TO 70 GHz

A dissertation submitted to the

SWISS FEDERAL INSTITUTE OF TECHNOLOGY ZURICH

for the degree of

Doctor of Sciences

presented by

JOHANNES HOFFMANN

Diplom Ingenieur
University of Stuttgart, Germany

Ingénieur des Télécommunications
École Nationale Supérieure des Télécommunications, France

born August 31, 1978
citizen of Germany

accepted on the recommendation of

Prof. Dr. Ch. Hafner, examiner
Prof. Dr. R. Vahldieck, co-examiner
Dr. U. Arz, co-examiner

2009

Acknowledgments

Abstract

Measuring the reflectivity and transmissivity of microwave devices has many applications in science and industry. Measurement tasks range from component testing for cell phones to characterizing carbon nano tube transistors. There are commercial solutions for most measurement tasks. Nonetheless, there will always be the question: What is the accuracy of such measurements and how can it be improved? In coaxial S-parameter measurements, the largest error contributions come from the connectors. The most precise connectors, laboratory precision connectors, have to be examined to improve measurement accuracy. A related topic is the question how reflection and transmission can be measured accurately with snap-on connectors.

Probably the most fundamental requirement to answer these questions is to understand how electromagnetic waves propagate in coaxial lines. There are many publications on this topic, but still the presented theories fail to accurately predict wave propagation in coaxial lines with plated rough surfaces for frequencies above $50\,\text{GHz}$. A new method to predict the phase constant and the losses in such realistic coaxial lines is presented. Using a 2D field simulator, the effects of roughness and plating are converted to artificial material parameters. These are used to define a coaxial line problem with smooth conductors, which can be solved with already known algorithms. The method presented here is far more accurate than existing techniques and can thus be used for the computation of calibration standards.

Here only standards which completely consist of metal are considered because they can be characterized most accurately. Air lines and offset shorts are such standards. Both are connected with a connector to the vector network analyzer (VNA). This connection is usually neglected for the calculation of calibration standard parameters, but it is essential for frequencies higher than $50\,\text{GHz}$. For this reason a 3 D field simulation of the slotted 1.85 mm connector is done. Careful validation of the simulation based on (A) comparing the results of two different numerical techniques, (B) parameter studies and (C) meshing convergence are essential for the

derived S-parameter model of the connector. With a software implementation of this model one can compute the reflection coefficient of a given connector within seconds. Cascading the model of the connector with the model of the transmission line yields the S-parameters of an air line standard. A similar combination, extended by the model of a short plane, yields the reflection coefficient of an offset short.

Such transmission and reflection standards are used for the calibration of a VNA. Thereby the VNA is described by a simplified model which contains the main paths of wave propagation in the VNA. Given the VNA model, calibration means finding the coefficients of wave propagation for each path. One often measures more standards than necessary to determine the coefficients. The inevitably occurring inconsistencies between standards, VNA model and measured raw S-parameters are usually attributed to the definition of the standards. The calibration algorithm presented here attributes the occurring errors not only to the definition of the standards but as well to the simplified model of the VNA. Temperature drift and cable movement are the most prominent among numerous reasons why the simplifying assumptions for the model of the VNA are not correct. Thus the new error model of calibration is closer to reality. As a next step, the error model is converted into an equation for calibration by the application of Bayes law. The resulting algorithm uses nonlinear optimization and Monte Carlo integration for the computation of the calibration coefficients. The realistic modeling of uncertainties results in a more stable and accurate calibration algorithm.

The calibration of a VNA with snap-on connectors requires special measures. In fact, performing a usual calibration with snap-on connectors is almost senseless because snap-on connections are much less repeatable than laboratory precision connections. It is shown that a much better approach is using a characterized adapter from precision to snap-on connector. The respective advantage in terms of accuracy is quantified by comparing various traditional calibration methods and the adapter method by Monte Carlo simulation (MCS). A crucial point is the characterization of the adapters. Two methods are investigated and compared against each other. The first is a method which uses only short, open and thru, the second is a method which uses beadless adapters. The beadless adapters are characterized by mechanical measurements and subsequent modeling. The accuracy achieved with the beadless adapter method is superior to the first method, which uses the short, open and thru standards.

Zusammenfassung

In Industrie und Wissenschaft müssen häufig Transmission und Reflexion an Mikrowellenkomponenten gemessen werden. Die Messaufgaben sind sehr vielfältig und reichen von Messungen an Mobilfunkkomponenten bis zur Charakterisierung von Carbon Nanotube Transistoren. Obwohl es für die meisten Messaufgaben kommerzielle Lösungen gibt, wird folgende Frage immer wieder gestellt: Was ist die Genauigkeit der Messungen und wie kann sie erhöht werden? Für koaxiale S-Parameter Messungen ergibt sich die Antwort meist aus einer genauen Analyse der Stecker. Durch eine Charakterisierung der Stecker kann die Messgenauigkeit meist deutlich erhöht werden, was sowohl für die genauesten verfügbaren Stecker, sogenannte Präzisionsstecker, als auch für auf Industrieanwendungen ausgelegte Schnappverschlussstecker funktioniert.

Da sich ein Stecker im Idealfall wie ein Stück Leitung verhält, ist es sinnvoll zunächst die Fortpflanzung elektromagnetischer Wellen in Koaxialleitungen zu studieren. Zu diesem Thema gibt es viele Veröffentlichungen, aber mit den gängigen Theorien kann man die Fortpflanzung von Wellen in Koaxialleitungen mit rauen beschichteten Oberflächen nur sehr ungenau berechnen. Eine neue und genauere Methode, um die Phasenkonstante und die Verluste einer solchen realitätsnahen Koaxialleitung zu bestimmen, besteht darin, die Auswirkungen von Rauhigkeit und Beschichtung mit einem 2D Feldsimulationsprogramm in künstliche Materialparameter zu konvertieren. Diese werden wiederum benutzt, um ein Koaxialleitungsproblem mit glatten Leitern zu definieren, welches mit schon bekannten Algorithmen gelöst werden kann. Die hier präsentierte Methode ist weitaus genauer als bestehende Techniken und kann deshalb zur Berechnung von Kalibrationsstandards eingesetzt werden.

Ganz aus Metall bestehende Standards wie Luftleitungen und Offset Shorts lassen sich am genauesten charakterisieren. Beiden Standardtypen ist gemein, daß sie mit Steckern an den Netzwerkanalysator (NWA) angeschlossen werden, welche allerdings bei der Berechnung von Kalibrationsstandards normalerweise nicht berücksichtigt werden. Um diesen Fehler in der Definition der Standards zu beheben, wurde eine 3D Feldsimu-

lation des geschlitzten 1.85 mm Steckers durchgeführt. Eine sorgfältige
Überprüfung der Simulationsergebnisse anhand von Vergleichen zwischen
verschiedenen numerischen Methoden, Parameterstudien und Konvergenz-
studien ist sehr wichtig für die Genauigkeit der Ergebnisse. Durch Varia-
tion der Steckerdimensionen kann aus den Simulationsergebnissen eine
Datenbank aufgebaut werden, die mittels Interpolation die S-Parameter
eines beliebigen Steckers innerhalb weniger Sekunden bereitstellt. Dieses
Modell erlaubt auf einfache Art und Weise die komplette Beschreibung
eines Standards. So wird für einen Luftleitungsstandard das Modell des
linken und rechten Steckers und der dazwischen liegenden Koaxialleitung
kaskadiert, um die S-Parameter des ganzen Standards zu berechnen. Das
Modell des Offset Shorts ist ähnlich, allerdings wird hier der zweite Stecker
durch eine Kurzschlussebene ersetzt.

Solche Transmissions- und Reflexionsstandards werden für die Kalibra-
tion eines NWAs benutzt. Das Ziel der Kalibration ist, die Koeffizienten
der Wellenhauptausbreitungspfade im NWA zu bestimmen. Dazu wer-
den häufig mehr Standards als nötig gemessen, was unweigerlich zu In-
konsistenzen zwischen Standards, NWA Modell und gemessenen rohen
S-Parametern führt. Diese Inkonsistenzen werden meist durch Fehler in
der Beschreibung der Standards erklärt, aber der hier beschriebene Kali-
brationsalgorithmus basiert auf einem allgemeineren Fehlermodell. Durch
Temperaturdrift und Kabelbewegungen verändern sich die als konstant
angenommenen Koeffizienten der Ausbreitungspfade im NWA, was ein um
Fehler im NWA Modell erweitertes Fehlermodell motiviert. Dieses erwei-
terte Fehlermodell wird mit dem Bayesschen Gesetz in eine Kalibrations-
gleichung umgewandelt. Der auf dieser Gleichung basierende Algorithmus
verwendet nichtlineare Optimierung und Monte Carlo Integration, um
die Kalibrationskoeffizienten zu berechnen. In einem Vergleich mit ande-
ren Kalibrationsalgorithmen hat sich gezeigt, daß der neue Algorithmus
stabiler und präziser als die getesteten Algorithmen ist.

Die bisher beschriebene Strategie, bestehend aus genauer Modellie-
rung der Standards und Minimierung des Fehlereinflusses durch stati-
stische Modellierung, ist von begrenztem Nutzen für Messobjekte mit
Schnappverschlusssteckern. Die Längenvarianz solcher Steckverbindungen
ist so groß, daß eine Kalibration mit Schnappverschlussstandards nicht
die geforderte Genauigkeit liefern kann. Allerdings hat eine Monte Carlo
Simulation des Kalibrationsprozesses gezeigt, daß eine viel höhere Mess-
präzision durch eine vorhergehende Kalibration mit Präzisionssteckern

und nachfolgendem Anbringen von Adaptern erzielt werden kann. Die dabei erforderlichen Adapter müssen möglichst genau charakterisiert sein, was mit zwei hier untersuchten Methoden erreicht werden kann. Die erste Methode benötigt die Schnappverschlusstandards Short, Open und Thru zur Charakterisierung der Adapter, während die zweite Methode mit stützscheibenlosen Adaptern arbeitet. Experimente haben gezeigt, daß die Methode mit den stützscheibenlosen Adaptern genauer ist als die erste Methode.

Contents

x

List of Figures

List of Tables

List of Acronyms and Abbreviations

BA . . . . beadless adapter

DUT . . . . device under test

FDTD . . . . finite difference time domain

FEM . . . . finite element method

FIT . . . . finite integration time domain

GUM . . . . guide to the expression of uncertainty in measurement

LRL . . . . line reflect line

MCS . . . . Monte Carlo simulation

MMP . . . . multiple multipole

NWA . . . . Netzwerkanalysator

pdf . . . . probability density function

PEC . . . . perfect electric conductor

QTEM . . . . quasi transversal electromagnetic

RF . . . . radio frequency

SOLT . . . . short open load thru

SOT . . . . short open thru

TE . . . . transversal electric

TEM . . . . transversal electro magnetic

TM . . . . transversal magnetic

TRL . . . . thru reflect line

VNA . . . . vector network analyzer

VSWR . . . . voltage standing wave ratio

1 Introduction

1.1 Background

A measurement process can be seen as a practical realization of a physical theory. For coaxial S-parameter measurements the theory is well known. The ratio of reflected or transmitted waves to incoming waves defines the reflection and transmission coefficients respectively. The theoretical concept of S-parameter measurements is embodied in coaxial standards. It is not trivial to define coaxial standards, because the relationship between geometry, material parameters and the resulting S-parameters has to be established for this purpose. A further difficulty is that it is not possible to measure how accurate such definitions are because the measurement itself depends on the standard which should be measured. Thus, it is only possible to detect errors in the definition of standards by comparing different standards. Coaxial standards which are computed from geometry and conductivity are seldom available for frequencies up to 70 GHz. Most available standards for this frequency range are simply declared to have ideal values, e.g. loads have zero reflection.

1.2 Motivation

The ability to execute accurate coaxial S-parameter measurements is a key competence for the development of new microwave products. Accurate and precise microwave measurements provide the feedback link between prototyping and design. Such S-parameter measurements are done routinely up to frequencies of 50 GHz in 2.4 mm systems. Applications like automotive radar and advanced cordless telecommunication systems, which make use of oxygen attenuation, operate at higher frequencies. The reduced wavelength requires smaller connectors. Small snap-on connectors or 1.85 mm connectors can handle frequencies up to 70 GHz. Snap-on connectors are designed to be connected in a fast and easy way, whereas 1.85 mm connectors are intended for applications where accuracy and precision are very important.

Coaxial S-parameter measurements of a device under test (DUT) with snap-on connectors or 1.85 mm connectors are done with a VNA, which is calibrated with standards for the respective connector type. Several standards, DUTs with known S-parameters, are measured for calibration. The differences between known S-parameters of the standards and raw S-parameters displayed on the not yet calibrated VNA determine the error terms in a model of the VNA. This model accounts for the most important systematic imperfections of the VNA. Thus the goal of calibration is to find a model which describes the relationship between S-parameters of the DUT and raw S-parameters as accurately and precisely as possible.

In a next step, the model of the VNA is reversed to deduce the S-parameters of a DUT from the raw S-parameters of the VNA. Obviously the accuracy of the final measurement result depends solely on this correction process. The correction process itself is prescribed by the model which represents the VNA. The coefficients of this model are in turn determined by the used standards.

Thus higher measurement accuracy and a quantification of measurement uncertainty can be achieved by more accurate models of standards and a more accurate model of the VNA. While the production process of standards results in given mechanical tolerances, usually the dimensions of a standard can be measured with significantly lower uncertainty. It is possible to accurately compute the S-parameters of the standard by using such dimensional measurements as input to modern field solvers. Especially the connector and the surface roughness of the standard have a strong impact on the outcome of the calculation. Nonetheless, many not controllable parameters like cable movement or limited accuracy of the standards degrade the accuracy of the calibration. State of the art statistical methods can be used to minimize the impact of such error sources. In this thesis, both tools field solvers and statistical methods are used to improve the accuracy of VNA measurements and to provide starting points for the calculation of the expected error margins.

1.3 Objective

The objective of this thesis is to illustrate the computational process from material parameters and dimensions of standards via the statistical properties of the VNA to traceable S-parameters in coaxial devices up

to 70 GHz. New techniques of electromagnetic simulation and statistical modeling are required to achieve high measurement accuracy at such high frequencies.

While the influence of the connector was simply neglected in former times, this is no longer advisable for the frequencies under consideration. The small snap-on connectors and 1.85 mm connectors for frequencies up to 70 GHz can only be produced with slotted female contacts, whereas larger connectors for lower frequencies are available as slotless designs. The slotted connectors have noticeable influence on the S-parameters. Thus an accurate model which relates the geometry of a slotted connector to its S-parameters is needed.

Nearly all coaxial standards contain a section of coaxial transmission line after the connector. For lower frequencies one usually assumed the surface of this transmission line to be smooth. Now the frequency is increased but the mechanical production process of standards and thus the surface roughness stay the same. This results in a situation where one can observe noticeable effects of surface roughness on the propagation constant for frequencies above 50 GHz. A method to compute the propagation constant of a transmission line with rough surfaces is needed to calculate the S-parameters of standards containing transmission line sections.

Another effect of the increase in frequency are shorter wavelengths. Thus even very small mechanical instabilities of the VNA and the measurement cables or dimensional inaccuracies of the standards have a noticeable impact on the measurement results. A calibration algorithm which allows to minimize the influence of such statistical errors is needed to make measurements more precise.

The shorter wavelengths are as well a reason for the instable S-parameters of snap-on connectors. This strong variance poses a problem for VNA calibration because multiple connections are required to calibrate a VNA. Conventional calibration methods are useless in this context because the connector variability makes the calibration result highly random. A calibration method which minimizes the influence of these instabilities is required to measure S-parameters of DUTs with snap-on connectors accurately.

1.4 Outline

This thesis is subdivided into four technical chapters.

The first technical chapter is about S-parameters and how they are linked to the electromagnetic modes in coaxial transmission lines. The introduction of this chapter sketches all terms and concepts which are needed to define S-parameters. The most basic concept covered are modes in transmission lines. Consequently the well known formulas for modes in coaxial air lines with smooth surfaces are discussed. The following section describes a novel method of computing the influence of surface roughness and plating on the electromagnetic fields. Finally, the terms propagation constant, characteristic impedance, port and S-parameters are defined. The limits of these definitions with respect to rough air lines are emphasized.

The introduction of the second chapter gives a short overview over the most popular calibration standards. The influence of the connector on the S-parameters of the standard has been neglected in the past. For this reason, two new methods to compute the S-parameters of the slotted 1.85 mm connector are described. The thorough validation of the methods is followed by the presentation of a tool which computes the S-parameters of a connector within seconds. In the last section of this chapter, it is shown how to compute the S-parameters of offset shorts and transmission line standards. The model of the connector is used for this purpose but new techniques to compute the S-parameters of plain coaxial lines and short planes are illustrated as well.

A new calibration algorithm is described in the third chapter. It takes the errors of standard definitions and the errors of the VNA model into account. Among many factors, temperature drift and bending the cables are the most prominent reasons for discrepancies between the model of the VNA and reality. Using Bayes' law, the error model of calibration is converted to a calibration algorithm. The numerical implementation requires constrained nonlinear optimization and Monte Carlo Integration. These constraints are imposed by the passivity of the standards. They increase the accuracy and stability of the calibration algorithm. A far more important reason for the superior stability and accuracy of the new algorithm is the error model which captures the most important error sources.

Finally the fourth chapter contains solutions to the calibration problem

with snap-on connectors. Owing to their low repeatability, snap-on connectors require a non standard calibration procedure. Comparing traditional calibration methods and adapter de-embedding by a Monte Carlo simulation (MCS) showed the superiority of adapter de-embedding. A crucial step in the adapter de-embedding method is the characterization of the adapters. Two new methods for adapter characterization are implemented. First, a method which uses only short, open and thru and which relies additionally on the reciprocity of the adapters was implemented and tested. Secondly, a method utilizing beadless adapters which can be characterized numerically was tested. The beadless adapter method proofed to be more accurate than the short open thru method.

2 Coaxial Modes, Characteristic Impedance and S-parameters

Abstract — In the first sections of this chapter, the modes of coaxial transmission lines with smooth surfaces are described and computed. Then a novel method for the computation of modes in rough plated coaxial lines is presented. After this a short introduction to transmission line theory is given. The therewith associated characteristic impedances are derived from the previously computed modes. The concept of S-parameters and ports is explained in the last part.

2.1 Introduction

A VNA measures the reflectivity and transmissivity of a DUT. The concepts of reflection and transmission measurement require two waves[1] respectively. One which travels towards the DUT and one which is reflected or transmitted. These waves are measured on planes (ports) which are perpendicular to the direction of propagation. The outcome of the VNA measurement are reflection coefficients and transmission coefficients, i.e., ratios of received and transmitted wave amplitudes.

The same physical facts are described by transmission line theory. It models the mechanisms of propagation on homogenous line sections with propagation constants and wave amplitudes. A common simplification is the assumption of a single mode on each line section. This assumption is based on the fact that only the so called fundamental mode propagates with low attenuation. Reflection and transmission at the endpoints of line sections are modeled with characteristic impedances. Hereby network theory is used to compute reflection and transmission. These simplifications are in general inexact but provide in many cases useful values.

---

[1]The term wave represents a certain pattern of electromagnetic fields (mode) which propagates in a coaxial transmission line with given speed and losses (propagation constant) in a given direction. The strength of the wave is described by its complex amplitude.
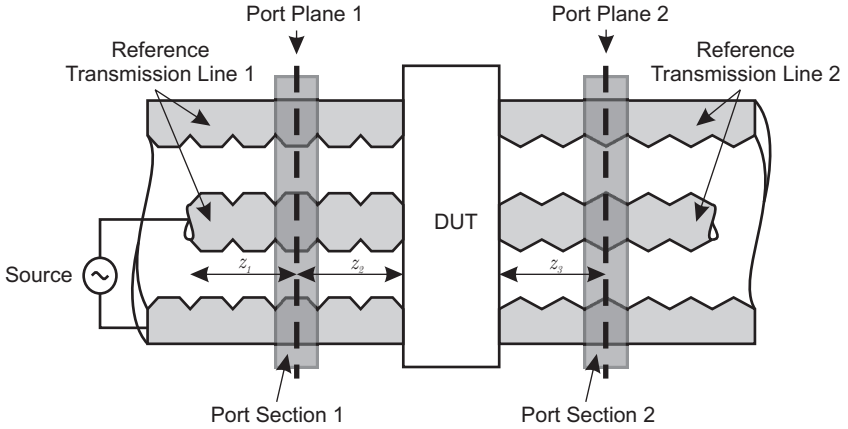
Figure 2.1: The ports are cross-sections of the reference transmission lines. The reference transmission line determines the mode which is measured at a port.

An even more abstract description of reflection and transmission is given by S-parameters. They are reflection and transmission coefficients which are measured with a virtual measurement system. The reference impedance characterizes the virtual measurement system. Transmission line theory allows one to convert S-parameters from one reference impedance to another.

Traceable S-parameters are S-parameters which are linked to the SI units with a given uncertainty. To establish this link, it is necessary to state the material properties and dimensions of the coaxial waveguide in SI units with associated uncertainties. Once this is done, traceable modes, characteristic impedances and finally S-parameters can be computed. Obviously the first step for the measurement of traceable S-parameters is to properly define what a mode is.

2.2 Modes

There are several definitions of modes in literature, [1], [2], [3]. Here a mode is defined as an eigen solution of Maxwell's equations in a waveguide which can not be decomposed into other independent eigen solu-

tions. Note that modes propagating on the outside of transmission lines are not treated here. A mode consists of field pattern and propagation constant, whereas for a wave additionally the wave amplitude and propagation direction are given. If every Maxwellian field in a transmission line can be written as a superposition of modes, these modes are called a complete basis. The mode properties depend on the type of transmission line.

Lossless smooth transmission lines consist of perfect conductors and lossless dielectrics. They are perfectly straight in z-direction and support modes which span a complete basis of the solution space, [1]. The same holds for transmission lines with perfect conductors but lossy dielectrics. In practical cases coaxial transmission lines are usually used in a frequency range (monomode regime) where only one mode (the fundamental mode) propagates inside the transmission line.

Lossy smooth transmission lines consist of lossy conductors and lossy or lossless dielectrics. It is at least challenging if not impossible to show in a mathematically rigorous way that modes of the type

$$\vec{F}(x,y,z) = \vec{F}(x,y)e^{-\gamma z} \tag{2.1}$$

span a complete basis of the solution space. Here $\vec{F}(x,y,z)$ are the electromagnetic fields in the transmission line and $\vec{F}(x,y)$ is the form function of the mode. The propagation constant γ defines attenuation and phase velocity of the mode. In the monomode regime, the fundamental mode has far lower attenuation than higher modes.

Lossy periodic transmission lines are axisymmetric structures with a periodic pattern in z-direction. They consist of lossy conductors and lossy or lossless dielectrics. Depending on the type of roughness, one can approximate rough transmission lines by periodic transmission lines. With Floquet's theory one can show that periodic transmission lines support modes according to the here used definition of modes. A periodic line supports modes of the type

$$\vec{F}(x,y,z) = \sum_{n=-\infty}^{\infty} \vec{F}_n(x,y)e^{-(\gamma + j2\pi n/p)z}. \tag{2.2}$$

Here p is the length of the roughness pattern. Again the proof that these modes span a complete basis of the solution space is not known. However, all practical experiences show that rough lines with reasonably small roughness, i.e., the deviations from the smooth structure are small compared to the cross sectional dimensions, behave like a smooth transmission line with a single fundamental mode.

A practical definition of what the VNA measures is chosen due to the mathematical problems in showing the completeness of the solutions for lossy lines. A VNA measures the mode which has the lowest attenuation in the reference transmission line, see Fig. 2.1. In the case of a smooth line, this means the field pattern of the measured mode is the one towards which the electromagnetic field in the port plane converges if the distances z_1, z_2 and z_3 are increased equally. In the case of rough lines, the field pattern of the measured mode is the one towards which the electromagnetic field in the port section converges if the distances z_1, z_2 and z_3 are increased by similar numbers of roughness patterns. A port plane is a plane which is perpendicular to the z-direction of the smooth waveguide. The port section is essentially one roughness pattern.

The assumption that a VNA measures the mode with the lowest attenuation in the reference transmission line and that there is only one such mode is supported by the following observations. Different VNAs yield very similar measurement results if they are used with identical test ports and calibration kits. In other words, different excitations of a reference line lead to one single field pattern. It is found by measurements that the attenuation characteristics of the modes which occur in coaxial transmission lines are of the type $e^{-\gamma z}$. Modes with these attenuation characteristics will be computed in the following.

2.3 Coaxial lines with perfect conductors

The coaxial line with perfect conductors and a possibly lossy dielectric is used as a theoretical model. The cross section which is enclosed by the outer conductor supports an infinite number of modes which form a complete set. At very low frequencies only one mode (the fundamental TEM-mode) can propagate. The higher modes are capable to propagate only above a mode specific cut-off frequency. A short overview on these
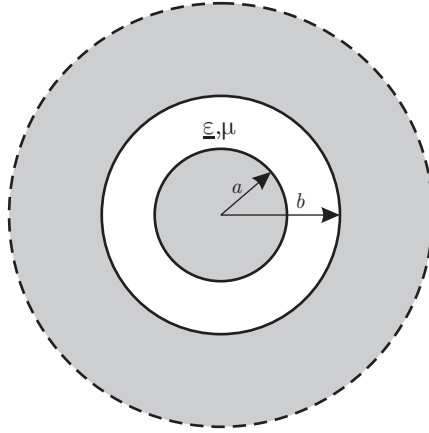
Figure 2.2: Cross section of an ideal coaxial line with dielectric. The gray areas designate perfect electric conductors (PECs) and the white area the dielectric.

higher modes is given here in order to set the cornerstones for monomode operation.

The geometry of a coaxial transmission line with perfect conductors and a dielectric specified by $\underline{\epsilon}, \mu$ is depicted in Fig. 2.2. The permeability μ is a real variable, whereas the permittivity

$$\underline{\epsilon} = \epsilon + \frac{\sigma}{j\omega} \tag{2.3}$$

is complex and linked to the real valued permittivity ϵ, the conductivity σ, the angular frequency ω and j the imaginary unit, assuming $e^{j\omega t}$ time dependence for all fields, voltages and currents.

As described in [4], an infinite number of modes with different cutoff frequencies exists in such a coaxial transmission line. The electromagnetic fields of the transversal electro magnetic (TEM) mode are depicted in Figs. 2.3a and 2.3b. The first higher non rotational symmetric mode is the transversal electric (TE)$_{11}$-mode which is depicted in Figs. 2.4a and 2.4b. It can be excited by non rotational symmetric discontinuities in the coaxial transmission line. The first higher rotational symmetric mode is the transversal magnetic (TM)$_{01}$-mode. It is depicted in Figs. 2.5a and

$2.5b$ and it can be excited by rotational symmetric discontinuities in the coaxial line.
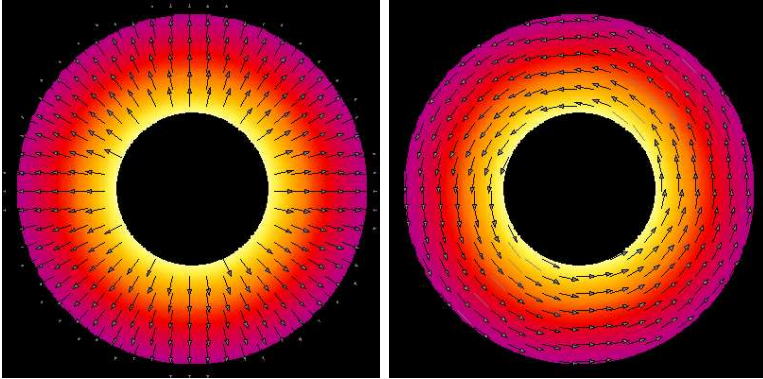
Figure 2.3a: Electric field of TEM-mode. The intensity $|\vec{E}|$ is indicated by colors. Brighter colors correspond to higher field strength. The direction $\vec{E}/|\vec{E}|$ is indicated by arrows.

Figure 2.3b: Magnetic field of TEM-mode. The intensity $|\vec{H}|$ is indicated by colors. Brighter colors correspond to higher field strength. The direction $\vec{H}/|\vec{H}|$ is indicated by arrows.

Usually coaxial transmission lines are used below the cutoff frequency of the first higher mode. The propagation constant of the TEM-mode

$$\gamma = j\omega\sqrt{\mu\underline{\epsilon}} \tag{2.4}$$

describes with which phase and attenuation constant the electromagnetic fields propagate. Table 2.1 gives the cutoff frequencies and the attenuation at $f = 70\,\text{GHz}$ of some modes in a $50\,\Omega$, $1.85\,\text{mm}$ coaxial system with air as dielectric. In the following, only modes which are very similar to the TEM mode are treated.

2.4 Coaxial lines with lossy conductors

The TEM mode does not exist in a coaxial line with lossy conductors. Instead of the TEM mode there is the quasi transversal electromagnetic (QTEM) mode. Its field distribution in the dielectric is very similar to
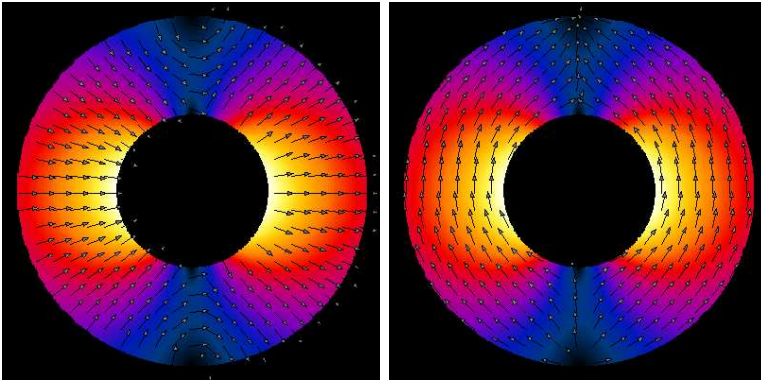
Figure 2.4a: Electric field of TE_{11}-mode. The field is represented in the same way as in Fig. 2.3a.

Figure 2.4b: Magnetic field of TE_{11}-mode. The field is represented in the same way as in Fig. 2.3b.
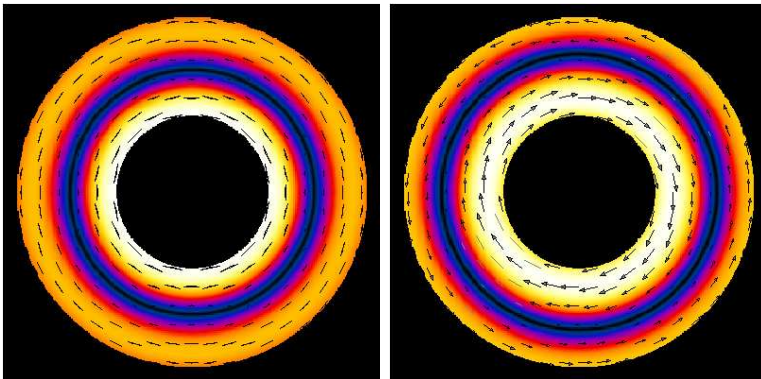
Figure 2.5a: Electric field of TM_{01}-mode. The field is represented in the same way as in Fig. 2.3a. Note that the dominant part of the electric field points in longitudinal direction.

Figure 2.5b: Magnetic field of TM_{01}-mode. The field is represented in the same way as in Fig. 2.3b.

Table 2.1: Modes in 1.85 mm coaxial transmission line with perfect conductors.

mode	TEM	TE_{11}	TM_{01}
cutoff frequency	0	73.4 GHz	284.08 GHz
attenuation at $f = 70$ GHz	0	9.27 dB/mm	115.4 dB/mm
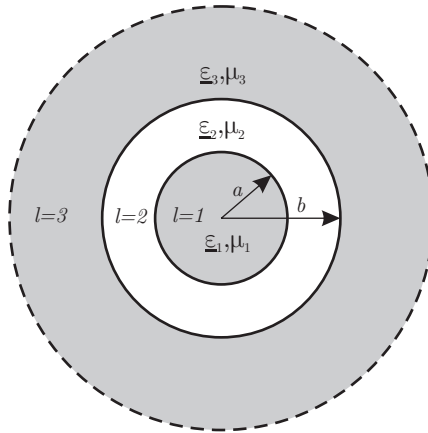
Figure 2.6: Cross section of lossy coaxial line with dielectric. The gray areas designate the conductors and the white area the dielectric.

the TEM mode. The electromagnetic fields of the fundamental mode, the QTEM mode, are described in [4], [5], [6] and [7]. In fact, the solution of the differential equation which describes the QTEM mode is not trivial and requires a special algorithm. The algorithm presented in the following is similar to the one described in [6].

As in [6] it is assumed that the thickness of the outer conductor exceeds the penetration depth of electromagnetic fields by far. This assumption is

valid down to frequencies of $f = 1\,\mathrm{MHz}$ where the skin depth $\delta = 159\,\mu\mathrm{m}$ of a base material with conductivity[2] $\sigma = 10^7\,\mathrm{S/m}$ is small compared to the thickness of the outer conductor. Consequently, for higher frequencies it can be assumed with good accuracy that the outer conductor extends to an infinite radius. This is indicated by the dashed line which delimits the outer conductor in Fig. 2.6.

Maxwell's equations in frequency domain are used to compute the fundamental mode

$$\mathrm{rot}\vec{H} = j\omega\underline{\epsilon}\vec{E} \tag{2.5}$$

$$\mathrm{rot}\vec{E} = -j\omega\mu\vec{H}. \tag{2.6}$$

Here $\vec{E}$ and $\vec{H}$ denote the complex electric and magnetic field. In a cylindrical coordinate system, the fundamental mode has only three non-zero field components: the longitudinal electric field E_z, the transversal electric field E_r and the transversal magnetic field H_ϕ. Rewriting Maxwell's equations (2.5) and (2.6) for the three non-zero field quantities yields

$$-\frac{\partial}{\partial z}H_\phi = j\omega\underline{\epsilon}E_r \tag{2.7}$$

$$\frac{\partial}{\partial z}E_r - \frac{\partial}{\partial r}E_z = j\omega\mu H_\phi \tag{2.8}$$

$$\frac{\partial}{\partial r}H_\phi + \frac{H_\phi}{r} = j\omega\underline{\epsilon}E_z. \tag{2.9}$$

Restricting (2.7)-(2.9) to the l-th region, see Fig. 2.6, and decoupling of the equations yields Bessel's differential equation for the transversal magnetic field

$$r^2\frac{\partial^2 H_\phi^{(l)}}{\partial^2 r} + r\frac{\partial H_\phi^{(l)}}{\partial r} + (h^{(l)2}r^2 - 1)H_\phi^{(l)} = 0. \tag{2.10}$$

The parameter $h^{(l)2}$ is defined as

$$h^{(l)2} = \gamma^2 - \omega^2\mu^{(l)}\underline{\epsilon}^{(l)}. \tag{2.11}$$

---

[2] Copper has a conductivity of $\sigma \approx 5\times10^7$ S/m. Usually parts are made from beryllium copper, which has lower conductivity. Conductivity is difficult to predict because stresses introduced by machining change the conductivity.

A solution of the above given Bessel's differential equation can be expressed by the following linear combination of Hankel functions of first and second kind

$$Z_k^{(l)}(h^{(l)}r) = A^{(l)} H_k^{(1)}(h^{(l)}r) + H_k^{(2)}(h^{(l)}r). \tag{2.12}$$

Where $A^{(l)}$ is a complex constant which has to be determined by the boundary conditions. The index k depends on the differential equation which has to be solved. In the case of (2.10) this would be $k = 1$ because of $\ldots + (h^{(l)2}r^2 - 1)H_\phi^{(l)} = 0$.

Using (2.7), (2.8), (2.9) and (2.12), the electromagnetic fields in the l-th region can be written as

$$H_\phi^{(l)}(r) = B^{(l)} Z_1^{(l)}(h^{(l)}r) \tag{2.13}$$

$$E_r^{(l)}(r) = \frac{B^{(l)}\gamma}{j\omega\underline{\epsilon}^{(l)}} Z_1^{(l)}(h^{(l)}r) \tag{2.14}$$

$$E_z^{(l)}(r) = \frac{B^{(l)}h^{(l)}}{j\omega\underline{\epsilon}^{(l)}} Z_0^{(l)}(h^{(l)}r). \tag{2.15}$$

$B^{(l)}$ is a complex constant which has to be determined like $A^{(l)}$ by the boundary conditions. Note that $k = 1$ for the transversal components and $k = 0$ for the longitudinal component. The arguments of the Hankel functions become rather large for the resulting $h^{(l)}$. For the evaluation of the Hankel functions, one can use the formulas (B.1) and (B.2) in appendix B.

In each of the three layers in Fig. 2.6, the field is described by (2.13), (2.14) and (2.15). The constants $A^{(l)}$, $B^{(l)}$ and the eigenvalue γ are still unknown. To solve the eigenvalue problem, the following well known approach is made:

a) Layer one has the solution $Z_k^{(1)}(h^{(1)}r) = J_k(h^{(1)}r)$ because the Neuman function diverges for a zero argument. This requires $A^{(1)} = 1$.

b) The outermost layer has the solution $Z_k^{(3)}(h^{(3)}r) = H_k^{(2)}(h^{(3)}r)$ because the second Hankel function does not diverge for infinite arguments in the upper right complex plane. This requires $A^{(3)} = 0$

c) The layer in-between has the already mentioned general solution (2.12).

Using the boundary conditions for the continuity of E_z and H_ϕ on the boundary between center conductor and dielectric, one obtains after canceling of the amplitudes $B^{(1)}$ and $B^{(2)}$

$$\frac{Z_1^{(1)}(h^{(1)}a)}{Z_0^{(1)}(h^{(1)}a)} = \frac{Z_1^{(2)}(h^{(2)}a)}{Z_0^{(2)}(h^{(2)}a)} \frac{h^{(1)}\underline{\epsilon}^{(2)}}{h^{(2)}\underline{\epsilon}^{(1)}}. \tag{2.16}$$

The second boundary gives the second equation

$$\frac{Z_1^{(2)}(h^{(2)}b)}{Z_0^{(2)}(h^{(2)}b)} = \frac{Z_1^{(3)}(h^{(3)}b)}{Z_0^{(3)}(h^{(3)}b)} \frac{h^{(2)}\underline{\epsilon}^{(3)}}{h^{(3)}\underline{\epsilon}^{(2)}}. \tag{2.17}$$

Utilizing (2.16) and (2.17), the eigenvalue problem can be solved in an iterative algorithm:

a) Start with an estimated value for γ. This estimate can come from approaches like [4] or [5].

b) Starting with (2.16) for the innermost layer $A^{(2)i}$ can be computed.

c) $A^{(2)o}$ can be computed using (2.17) for the outermost layer.

d) This gives rise to an error term $E = A^{(2)i} - A^{(2)o}$

e) The derivative $\Delta = \frac{\partial E}{\partial \gamma}$ can be approximated numerically.

f) A better γ can be guessed by $\gamma_{new} = \gamma_{old} - \frac{E}{\Delta}$.

The presented algorithm can compute the propagation constant up to 70 decimal digits. The numerical implementation of this algorithm is straight forward except for the involved Hankel functions. The evaluation of Hankel functions for large arguments requires the approximations described in Appendix B.

2.5 Coaxial lines with rough lossy conductors

Lossy smooth transmission lines (see previous section) are an idealization of practical transmission lines which are lossy and have rough surfaces. The manufacturing steps of a transmission line cause the roughness. In the production process of an air line, the most relevant machining steps
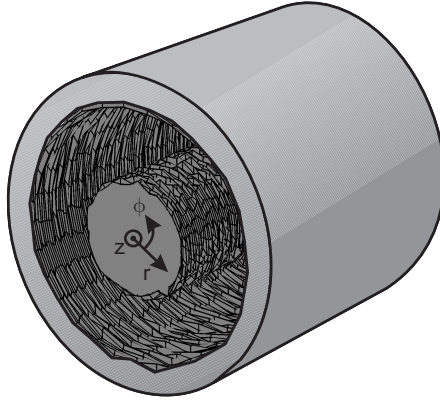
Figure 2.7: Rough conductor surfaces of a coaxial line with cylindrical coordinate system

involve rotating tools or rotating work pieces in conjunction with an automatic feed. The result is a helix pattern on the surfaces of the air line. This pattern can be approximated as a periodic ring pattern because the pitch of the helix is approximately $1\,\mu$m and the diameters are larger than $800\,\mu$m. The approximation as a periodic ring pattern simplifies the problem considerably because now Floquet's theorem and the axial symmetry can be exploited.

The fundamental mode of a lossy coaxial line with periodic rough surfaces is characterized by an eigenvalue which has similar properties as the propagation constant. One can compute this eigenvalue with a perturbation calculation based on the solution for a smooth problem. In [8] such a perturbation calculation is described:

a) For center and outer conductor, the perturbation terms should be derived respectively from a cylinder or bore with rough surfaces. Nonetheless, Sanderson [8] uses a flat periodic roughness profile which is illuminated by a plane wave which causes a scattered field limited to the close vicinity of the surface. This approach gives inaccurate but acceptable perturbation results under the condition that the skin depth is much smaller than the cross sectional dimensions
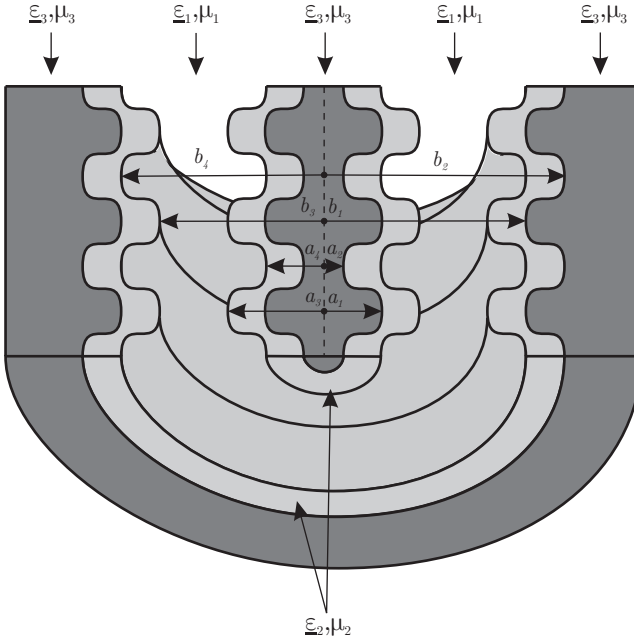
Figure 2.8: A longitudinal section of the coaxial transmission line. The different materials are characterized by complex permittivity $\underline{\epsilon}_l$, and permeability μ_l. Dark gray, light gray and transparent indicate base metal ($l = 3$), plating ($l = 2$) and dielectric ($l = 1$) respectively. For the sake of visibility, the relation between roughness and diameters is exaggerated. Maximum and minimum radii of the center conductor are designated by a_i, whereas the b_i are used for the respective radii of the outer conductor.

of the transmission line.

b) The flat field problem is solved by using an infinite sum of Rayleigh waves. The condition $2\pi h/p \leq 0.448$ ([9, 10]) for the applicability of the Rayleigh hypothesis on sinusoidal roughness with amplitude h and roughness period p is violated for some of the surfaces which are depicted in [8]. A comparison of surface impedances predicted by the method presented in [8] and computed with the multiple multipole (MMP) method shows significant differences for roughness

profiles with $2\pi h/p > 0.448$.

c) Use the mean value of the electric field above the rough surface to obtain a virtual surface displacement d_e such that it describes the influence of the roughness on a fictitious plate capacitor.

d) Use the mean surface impedance on the rough surface to obtain a complex surface displacement d_i which describes the influence of the roughness on a fictional parallel plate inductor.

e) Compute the propagation constant from the transmission line parameters which are perturbed by d_e and d_i. However, it has to be mentioned that this is a non physical way of computing the propagation constant as the transmission line parameters are not uniquely defined for lossy lines, see [11].

In the following, a new and more accurate method for the computation of the eigenvalue of a rough lossy coaxial transmission line is presented. First, the coaxial line including roughness and plating is described as a whole. A theoretical discussion using Floquet's theory shows that roughness has only local influence on the electromagnetic fields. This shows that the inner and outer surface of a coaxial line can be treated separately from each other. The second subsection is dedicated to the computation of the electromagnetic fields of a separate rough plated surface which is illuminated by a plane wave. Utilizing the MMP method in combination with the Rayleigh method cancels the original restriction $2\pi h/p \leq 0.448$ of the Rayleigh hypothesis for such problems. Equivalent material parameters are extracted from the results of the auxiliary planar problem. These parameters describe the conductors in a coaxial line problem with smooth surfaces, which is finally solved in a way similar to Daywitt's approach [6]. Moreover, the angle of incidence used in the planar auxiliary problem is coupled to the result of the equivalent coaxial problem. In the last subsection, the bounds of accuracy are discussed and the solution is compared against Daywitt's formula, Sanderson's formula and against measurements of the propagation constant made with Multical, see [12] and [13].

2.5.1 The electromagnetic field problem

The electromagnetic field problem of a coaxial transmission line is defined by the production process of its center conductor and outer conductor. The center conductor is usually produced by lathing or centerless grinding, whereas the outer conductor requires drilling and honing. The required machining steps involve either rotating tools or a rotating work piece in conjunction with an automatic feed. This is the reason why the resulting surfaces have a helix like pattern. Due to the small helix pitch (approx. $1\,\mu$m) and the large helix diameter (larger than $800\,\mu$m) one can approximate the helix as a sequence of grooves in ϕ-direction, see Fig. 2.7 and 2.8. The depth of the grooves is approx. $1\,\mu$m. To prevent corrosion, the surfaces of center and outer conductor are plated with a layer of precious metal. During the plating process the grooves are enlarged or smoothed in dependence of the plating process and the plating material. A typical hard gold plating is approximately $1\,\mu$m thick and barely deepens or flattens the grooves of the base metal, see Fig. 2.8.

The following assumptions are made to compute the eigenvalue γ of the fundamental mode in a transmission line with grooves:

a) The grooves are assumed to be in ϕ-direction, i.e., axisymmetric, and strictly periodic, see Fig. 2.8 and 2.9. Grooves which have other directions are neglected because in most coaxial transmission lines the amount of grooves in other directions is small. The use of a strictly periodic roughness profile is close to reality.

b) The used metals and the air enclosed in the transmission line are assumed to be linear. This is a valid assumption for typical field strengths in S-parameter measurements.

c) In the following, it is assumed that the thickness of the outer conductor exceeds the penetration depth of electromagnetic fields by far. This assumption is valid down to frequencies of $1\,$MHz where the skin depth $\delta = 159\,\mu$m of a base material with conductivity $\sigma_3 = 10^7\,$S/m is small compared to the thickness of the outer conductor. Consequently it can be assumed with good accuracy for higher frequencies that the outer conductor extends to infinity.

The QTEM mode of a smooth coaxial line is similar to the fundamental mode of a axisymmetric, periodic, coaxial transmission line. The latter
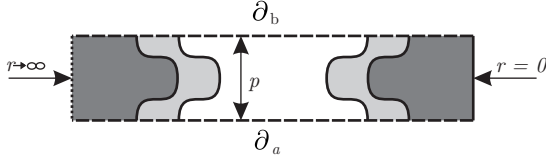
Figure 2.9: The period of the axisymmetric eigenvalue problem is p. The boundaries ∂_a and ∂_b are subject to Floquet's boundary conditions $\vec{F}_b = \vec{F}_a e^{-\gamma p}$ where $\vec{F}_a$ is the field on ∂_a and $\vec{F}_b$ is the field on ∂_b. The eigenvalue of the fundamental mode is γ.

has three non-zero field components: the longitudinal electric field E_z, the transversal electric field E_r and the transversal magnetic field H_ϕ. Like for the smooth lossy coaxial line, the field components are coupled by (2.7-2.9). The components are merged to simplify notation

$$\vec{F}(r, \phi, z) = \begin{pmatrix} E_z(r, \phi, z) \\ E_r(r, \phi, z) \\ H_\phi(r, \phi, z) \end{pmatrix}. \tag{2.18}$$

The eigenvalue problem which has to be solved for the fundamental mode is depicted in Fig. 2.9. Its boundary conditions at $r = 0$ and $r \to \infty$ are given by the axisymmetric nature of the problem. The boundary conditions between the different materials are given by the continuity conditions for electric and magnetic fields. Floquet's theorem, [14], guarantees that a nonzero solution which fulfills the periodic boundary conditions

$$\vec{F}_b = \vec{F}_a e^{-\gamma p} \tag{2.19}$$

at ∂_a and ∂_b exists. $\vec{F}_{a,b}$ denotes the electromagnetic field on the boundaries and p is the period. Furthermore, Floquet's theory allows one to write the electromagnetic field of the fundamental mode as

$$\vec{F}(r, \phi, z) = \sum_{n=-\infty}^{\infty} \vec{F}_n(r, \phi) e^{-(\gamma + j2\pi n/p)z}. \tag{2.20}$$

The structure functions $\vec{F}_n(r,\phi)$ consist of structure functions for electric and magnetic fields

$$
\vec{F}_n(r,\phi) = \begin{pmatrix} E_{zn}(r,\phi) \\ E_{rn}(r,\phi) \\ H_{\phi n}(r,\phi) \end{pmatrix}.
\tag{2.21}
$$

Next it is shown that each Floquet term fulfills Maxwell's equations in regions which are homogenous in z-direction. For this purpose the differential equations (2.7), (2.8) and (2.9) are multiplied by $e^{(\gamma+j2\pi m/p)z}$ and integrated over one period in z-direction

$$
\int_z^{z+p} \frac{1}{r}\frac{\partial}{\partial r} r H_\phi e^{(\gamma+j2\pi m/p)z} dz = \int_z^{z+p} (\sigma + j\omega\epsilon) E_z e^{(\gamma+j2\pi m/p)z} dz
\tag{2.22}
$$

$$
-\int_z^{z+p} \frac{\partial}{\partial z} H_\phi e^{(\gamma+j2\pi m/p)z} dz = \int_z^{z+p} (\sigma + j\omega\epsilon) E_r e^{(\gamma+j2\pi m/p)z} dz
\tag{2.23}
$$

$$
\int_z^{z+p} \frac{\partial}{\partial z} E_r e^{(\gamma+j2\pi m/p)z} dz \quad - \quad \int_z^{z+p} \frac{\partial}{\partial r} E_z e^{(\gamma+j2\pi m/p)z} dz
$$
$$
= \int_z^{z+p} j\omega\mu H_\phi e^{(\gamma+j2\pi m/p)z} dz.
\tag{2.24}
$$

Depending on the radii a_n and b_n, the coaxial line can be subdivided in L regions where the material does not change in z-direction. These regions are delimited by the r-coordinate, e.g. $a_3 < r < b_3$. Using the orthogonality properties of the exponential function, one obtains from

(2.22), (2.23) and (2.24)

$$(\sigma^{(l)} + j\omega\epsilon^{(l)})E_{zm}^{(l)}(r,\phi) = \frac{1}{r}\frac{\partial}{\partial r}rH_{\phi m}^{(l)}(r,\phi) \qquad (2.25)$$

$$(\sigma^{(l)} + j\omega\epsilon^{(l)})E_{rm}^{(l)}(r,\phi) = (\gamma + j2\pi m/p)H_{\phi m}^{(l)}(r,\phi) \qquad (2.26)$$

$$j\omega\mu^{(l)}H_{\phi m}^{(l)}(r,\phi) = -(\gamma + j2\pi m/p)E_{rm}^{(l)}(r,\phi)$$

$$-\frac{\partial}{\partial r}E_{zm}^{(l)}(r,\phi). \qquad (2.27)$$

This means that Maxwell's equations hold for each Floquet component $\vec{F}_m^{(l)}e^{-(\gamma+j2\pi m/p)z}$ in the l-th region.

This is the reason why the Bessel differential equation is useful to describe the electromagnetic fields of a single Floquet term. Note that this differential equation is already known from the smooth problem. In other words, equations (2.10)-(2.15) describe the electromagnetic fields of a single Floquet term in a homogenous subdomain. The only difference with respect to the mentioned smooth problem concerns the transversal wave number $h_m^{(l)}$ which is defined in (2.11) for the smooth problem. For the rough problem, it is defined as

$$h_m^{(l)2} = \left(\gamma + \frac{j2\pi m}{p}\right)^2 + j\omega\mu^{(l)}(j\omega\epsilon^{(l)} + \sigma^{(l)}) \qquad (2.28)$$

for the l-th homogeneous subdomain and the m-th Floquet term. Approximate numerical values of h_m for air as dielectric and $p = 1\,\mu$m are given in Table 2.2.

Due to the small value of p, the values in Table 2.2 become large. Now it is obvious that fields of the first order Floquet components decay to $1/e$ in a depth of less than $\delta < 1\,\mu$m for $f = 1$ GHz and $\delta < 100$ nm for $f = 70$ GHz. In other words, the field of the higher Floquet modes is concentrated around the boundaries of each region l. This shows that the field coupling between inner conductor and outer conductor happens only with the zero order Floquet term. A consequence of this finding is that it is sufficient to characterize the effects of roughness without considering the interaction between inner and outer conductor. The interaction is governed by the zero order Floquet term and can be treated separately. A closer look on the zero order Floquet term shows that it consists of two Hankel functions. The Hankel function of the first kind is a cylindrical

Table 2.2: Numerical Values of h_m

Number m of Floquet component	Frequency f	h_m
0	1 GHz	$-8.8 \times 10^2 + j4.2$
1	1 GHz	$-3.9 \times 10^{13} + j1.2 \times 10^6$
0	70 GHz	$-4.4 \times 10^6 + j3.0 \times 10^3$
1	70 GHz	$-3.9 \times 10^{13} + j1.2 \times 10^7$

wave which contracts towards the z-axis, whereas the Hankel function of the second kind expands from the z-axis. Thus the zero order Floquet term describes two cylindrical waves of opposite direction. The angles of incidence of both cylindrical waves on the boundaries of region l are identical.

The above motivates the separation of the complete field into a rapidly varying field $\vec{F}_f$ which is expressed by

$$\vec{F}_f = \sum_{n=-\infty}^{-1} \vec{F}_n(r, \phi)e^{-(\gamma+j2\pi n/p)z} + \sum_{n=1}^{\infty} \vec{F}_n(r, \phi)e^{-(\gamma+j2\pi n/p)z}. \quad (2.29)$$

The remaining fundamental Floquet component is the relatively slowly varying field $\vec{F}_s$ which is similar to a mode in a smooth waveguide

$$\vec{F}_s = \vec{F}_0(r, \phi)e^{-\gamma z}. \quad (2.30)$$

2.5.2 The numerical solution

In the dielectric of the coaxial transmission line, the "slow" fields $\vec{F}_s$ dominate, whereas the "fast" fields $\vec{F}_f$ are concentrated around the surfaces of

the conductors. The "slow" field consists of two cylindrical waves which illuminate the conductors of the transmission line under the same angle of incidence. These findings lead to the following numerical solution strategy:

a) The fields of a plane wave, illuminating a rough metallic surface under five given angles, are computed. The resulting surface impedances contain the effects of all higher Floquet components.

b) The surface impedances are transformed to five equivalent complex permittivities of smooth materials. Using equivalent materials instead of using the surface impedance corrects at least in first order for using a planar problem instead of a cylindrical one, see section 2.5.3.

c) The QTEM modes of five coaxial transmission lines made of the smooth materials are computed. These computations result in five angles of incidence of the cylindrical waves and five propagation constants.

d) Now one can interpolate between the five coaxial lines in such a way that the angle of incidence of the original plane wave equals the angle of incidence of the cylindrical wave. This quadratic interpolation provides the correct propagation constant.

The quadratic interpolation is chosen because numerical experiments showed approximately quadratic dependence on the typical angles of incidence. Thus at least three different angles of incidence are required for the interpolation. Using more different angles of incidence is a tradeoff between higher accuracy due to over-determination and longer computation time.

Plane wave incident on a rough surface

The field problem of a plane wave hitting a rough metallic surface is depicted in Fig. 2.10. The problem is solved with the MMP method, see [15]. The advantage of this method in a 2D application is that it satisfies the boundary conditions of electric and magnetic field equally well. Many commercial solvers compute the scalar magnetic potential and derive the electric field from the magnetic potential. Such a solution resolves the
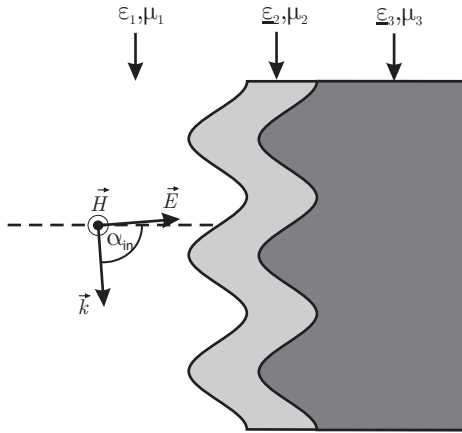
Figure 2.10: A plane wave hits a rough plated metallic surface. The vector $\vec{k}$ denotes the direction of propagation, whereas $\vec{E}$ and $\vec{H}$ designate the electric and magnetic field of the incident wave. Material 1 is the dielectric of the transmission line, material 2 is the plating metal and material 3 is the base metal. Typical values for the angle of incidence α_{in} are between $85°$ and $90°$.

magnetic boundary conditions well but the electric boundary conditions are resolved poorly. This disparity becomes crucial for problems where the geometrical features are much smaller than the wavelength.

The basis functions used by the MMP method, e.g., Rayleigh expansions and multipoles, are solutions of Maxwell's equations. The Rayleigh expansions are a sum of plane waves with different propagation directions, whereas multipole expansions are sums of Hankel functions of different order. In a first step, the locations of the multipoles and Rayleigh expansions are fixed. Next, matching points are distributed on the boundaries. The boundary conditions in each matching point give, depending on the type of boundary, several equations, which contain the amplitudes of multipoles and Rayleigh expansions. Writing the equations for all matching points results in an over-determined matrix because the MMP method uses more matching points than required. The over-determined system is solved in a way that the weighted square error is minimized. The weighting allows one to control the importance of boundary conditions for a specific matching point and field component. This control over the enforcement
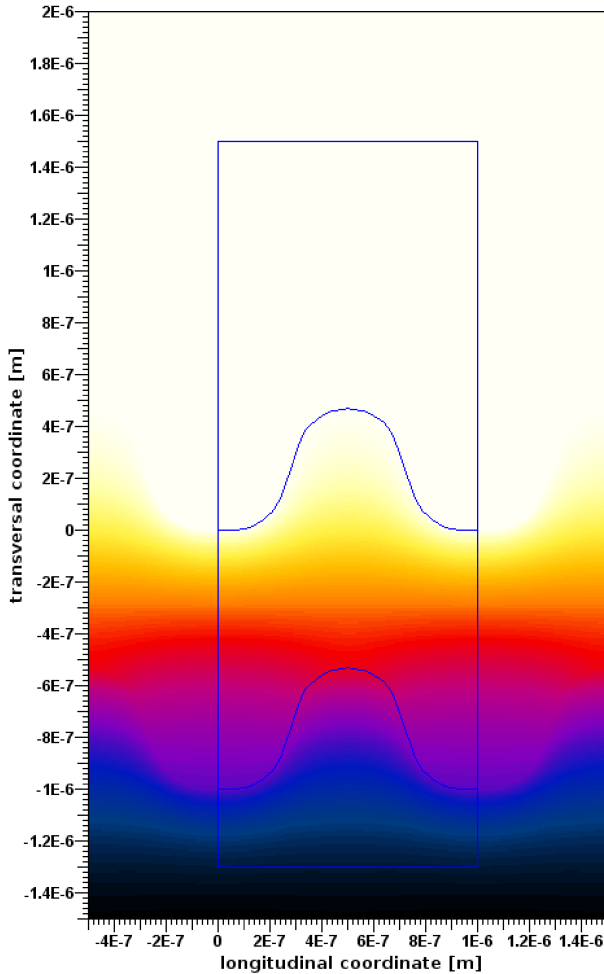
Figure 2.11: Magnetic field strength in a logarithmic color scale. The setup is the same as given in Fig. 2.10 with an angle of incidence of $\alpha_{in} = 89.75°$. As in Fig. 2.10 the plane wave is incident from the right. The frequency is 70 GHz. The shape of the roughness mimics experimentally observed roughness profiles.
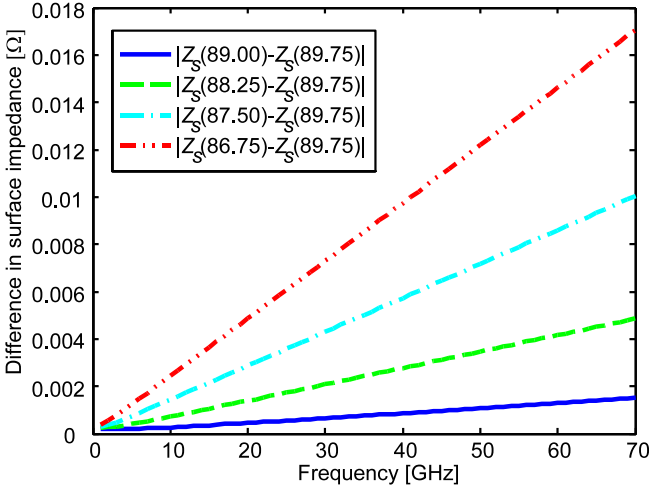
Figure 2.12: Differences of surface impedance measured $1.3\,\mu$m above the center of the roughness profile as a function of frequency and angle of incidence.

of boundary conditions is important to solve the given problem. As a last step, the system of equations has to be solved.

Figure 2.11 shows the computed magnetic field of a plane wave hitting a rough metallic surface. Such computations yield a relative error of the electromagnetic fields in the matching points below 0.13 percent for all frequencies and angles of incidence. The assumption that the "fast" field decays very rapidly towards the dielectric can be verified by reading the coefficients of the according Rayleigh expansions. It was observed that the amplitudes of the first and second order in the Rayleigh expansion differ by at least four orders of magnitude from each other. This is true for all used frequencies and angles of incidence at $d = 1.3\,\mu$m above the center of the roughness profile, $(a_4 + a_3)/2$ and $(b_4 + b_3)/2$. At this location the surface impedance is measured. It depends on the angle of incidence, see Fig. 2.12.
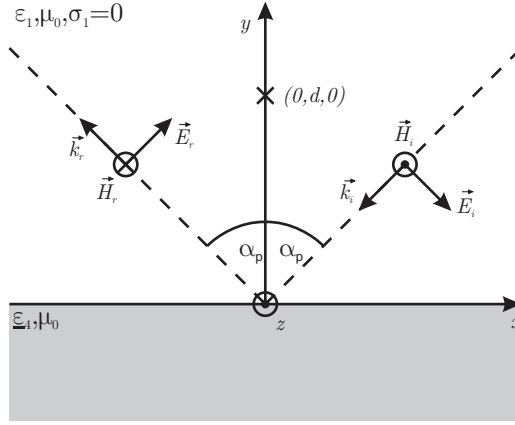
Figure 2.13: A plane wave in a known dielectric medium is reflected on an unknown second nonmagnetic conductive medium. In the point $(0, d, 0)$, situated in a distance d above the center of the roughness profile, the surface impedance is known. The second material has the permeability of vacuum but its complex permittivity is derived from the known surface impedance Z_s.

Extraction of the artificial material parameters

The next step in the computation of the eigenvalue of the fundamental mode is to convert the surface impedance Z_s, produced by a plane wave hitting a rough surface, to equivalent material parameters. The equivalent smooth material is designed in such a way that it replaces the original rough metallic surface without changing the surface impedance. Figure 2.13 illustrates the problem of finding the equivalent material parameters.

The permeability of vacuum is assumed for the artificial medium but its complex permittivity is determined by Z_s. The electric and magnetic field of the incident wave are

$$\vec{E}_i = E_i(\cos\alpha_p \vec{e}_x - \sin\alpha_p \vec{e}_y)e^{jk_1(\cos\alpha_p y + \sin\alpha_p x)} \quad (2.31)$$

$$\vec{H}_i = \frac{E_i}{Z_1}\vec{e}_z e^{jk_1(\cos\alpha_p y + \sin\alpha_p x)}. \quad (2.32)$$

Here α_p is the angle of incidence, the wave number is $k_1 = \sqrt{\omega^2\mu_0\epsilon_1}$ and

the characteristic impedance is $Z_1 = \sqrt{\frac{\mu_0}{\epsilon_1}}$. The reflected wave is

$$\vec{E}_r = E_r(\cos\alpha_p\vec{e}_x + \sin\alpha_p\vec{e}_y)e^{jk_1(\sin\alpha_px-\cos\alpha_py)} \qquad (2.33)$$

$$\vec{H}_r = \frac{E_r}{Z_1}\vec{e}_ze^{-jk_1(\sin\alpha_px-\cos\alpha_py)}. \qquad (2.34)$$

The observed surface impedance is

$$Z_s = \frac{\left(\vec{E}_i(0,d,0) + \vec{E}_r(0,d,0)\right)\vec{e}_x}{\left(\vec{H}_i(0,d,0) + \vec{H}_r(0,d,0)\right)\vec{e}_z}. \qquad (2.35)$$

From the surface impedance Z_s, one can find the reflection coefficient at the coordinate origin

$$\Gamma = \frac{Z_s - Z_1\cos\alpha_p}{Z_s + Z_1\cos\alpha_p}e^{j2k_1\cos\alpha_pd}. \qquad (2.36)$$

With

$$\Gamma = \frac{Z_4\cos\beta - Z_1\cos\alpha_p}{Z_4\cos\beta + Z_1\cos\alpha_p} \qquad (2.37)$$

one obtains

$$\cos\beta = \cos\alpha_p\frac{Z_1(1+\Gamma)}{Z_4(1-\Gamma)} \qquad (2.38)$$

where β is the complex transmission angle and $Z_4 = \sqrt{\frac{\mu_0}{\underline{\epsilon}_4}}$. Now the fact that

$$\frac{Z_1}{Z_4} = \frac{\sin\alpha_p}{\sin\beta} \qquad (2.39)$$

is used to obtain via a trigonometric identity

$$\sin 2\beta = \sin 2\alpha_p\frac{1+\Gamma}{1-\Gamma}. \qquad (2.40)$$

Finally, the equivalent complex permittivity is given by

$$\underline{\epsilon}_4 = \left(\frac{\sin\alpha_p}{\sin\beta}\right)\epsilon_1. \qquad (2.41)$$
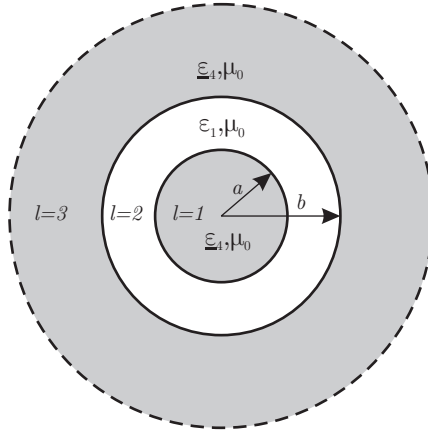
Figure 2.14: Coaxial transmission line consisting of three layers.

With the equivalent material parameters a smooth coaxial transmission line is defined, see Fig. 2.14. Its QTEM mode represents the "slow" field. To solve the three layer model, the algorithm in section 2.4 is used.

From the resulting propagation constant γ and the wave number in the dielectric k_1 one can compute the angle of incidence of the cylindrical wave

$$\alpha_c = \arcsin\left(\frac{\text{Re}\{j\gamma\}}{\text{Re}\{k_1\}}\right). \qquad (2.42)$$

Correcting the angle of incidence

Repeating the procedure, outlined in the preceding sections, for five different angles of incidence α_p, yields five different angles of incidence α_c of the cylindrical wave and five different propagation constants γ. As the solved plane wave problem should approximate the original problem with cylindrical waves as closely as possible, it is reasonable to require $\alpha_c = \alpha_p$. This requirement can be fulfilled by using a quadratic approximation of the function which relates α_p to α_c. The resulting correct angle α_p' is used to find the correct propagation constant γ' via another quadratic function.

As already mentioned, the angle of incidence of the plane wave should

be the same as the angle of incidence of the cylindrical wave. By assuming α_c to be a quadratic function of α_p, the correct angle of incidence α'_p of the plane wave is computed

$$
\begin{aligned}
\alpha_c &= q_{a1}\alpha_p^2 + q_{a2}\alpha_p + q_{a3} & (2.43) \\
\alpha'_p &= q_{a1}\alpha_p'^2 + q_{a2}\alpha'_p + q_{a3}. & (2.44)
\end{aligned}
$$

Where the q_{an} are coefficients which have to be determined. In a second step, a quadratic function relating α_p and propagation constant γ is used to compute the correct propagation constant γ'

$$
\begin{aligned}
\gamma &= q_{b1}\alpha_p^2 + q_{b2}\alpha_p + q_{b3} & (2.45) \\
\gamma' &= q_{b1}\alpha_p'^2 + q_{b2}\alpha'_p + q_{b3}. & (2.46)
\end{aligned}
$$

Again the q_{bn} are factors which have to be determined.

For the determination of the q_{an} and q_{bn}, a standard least squares approach is used. First the α_p are written as a matrix

$$
\mathbf{A} = \begin{pmatrix} \alpha_{p1}^2 & \alpha_{p1} & 1 \\ \alpha_{p2}^2 & \alpha_{p2} & 1 \\ \vdots & \vdots & \vdots \end{pmatrix}. \tag{2.47}
$$

Then the resulting angles of incidence of the cylindric wave are written as the vector $\vec{\alpha}_c$ and the respective propagation constants are written as $\vec{\gamma}$. The pseudo inverse of the matrix $\mathbf{A}$ is

$$
\mathbf{A}^+ = (\mathbf{A}^T\mathbf{A})^{-1}\mathbf{A}^T. \tag{2.48}
$$

The coefficients $\vec{q}_a$ and $\vec{q}_b$ are computed with this pseudo inverse

$$
\begin{aligned}
\vec{q}_a &= \mathbf{A}^+\vec{\alpha}_c & (2.49) \\
\vec{q}_b &= \mathbf{A}^+\vec{\gamma}. & (2.50)
\end{aligned}
$$

The q_{an} and q_{bn} are the components of $\vec{q}_a$ and $\vec{q}_b$.

2.5.3 Error Analysis

To specify the remaining errors of the described technique, one first sub-
divides the errors in numerical errors and systematic errors. Numerical
errors are the result of the precision of computations, whereas systematic
errors are a result of solving approximate equations.

To quantify these errors, recall the fact that the field of the higher order
Floquet terms is strongly concentrated around the conductor surfaces.
This fact renders the following virtual algorithm almost perfect.

a) Illuminate the rough outer and inner conductor with a cylindrical
   wave with a given γ_0 and compute their surface impedances accord-
   ingly.

b) Convert the surface impedances to material parameters of smooth
   surfaces.

c) Compute γ_s for the smooth surface problem using the procedure
   described in section 2.4.

d) Adjust γ_0 in a) in such a way that steps a)–c) produce a value
   $\gamma_s = \gamma_0$.

The essential difference between the real and the virtual algorithm consists
in the use of a rough planar surface instead of rough cylinders. Comparing
the second step of the virtual algorithm with the real algorithm leads to an
approximated systematic error of the algorithm. First, suppose that the
solution of the cylindrical rough problem and of the planar rough problem
are given. In both cases the surface impedance can be measured at a
distance $d = 1.3\,\mu\mathrm{m}$ above the center of the roughness profile. Obviously,
both surface impedances will be different. Secondly, one can de-embed
the surface impedances towards the center of the roughness profile. This
involves the use of Hankel functions for the cylindrical problem while plane
waves are used for the planar problem. Third, artificial smooth materials
are computed which will cause the same reflection as in the respective
original rough problem. Both materials are different because they are the
solution to different problems.

To give a conservative estimate of the systematic error, one assumes that
both problems should have the same electromagnetic fields and evaluate
the actual differences of the resulting fields. These fields are the solution

of two different systems of differential equations. In the case of the planar problem, the following system is solved

$$-\frac{\partial}{\partial z}H_y = j\omega\underline{\epsilon}E_x \tag{2.51}$$

$$\frac{\partial}{\partial z}E_x - \frac{\partial}{\partial x}E_z = j\omega\mu H_y \tag{2.52}$$

$$\frac{\partial}{\partial x}H_y = j\omega\underline{\epsilon}E_z, \tag{2.53}$$

whereas in the cylindric case the system (2.7)-(2.9) is solved. One can associate the directions r and x. The direction z has the same meaning in both coordinate systems and y replaces ϕ. Then both systems of equations are identical except for (2.53) and (2.9), which differ by the term H_ϕ/r. Considering a typical skin depth for $1\,\text{GHz}$ and the radius of a $1.85\,\text{mm}$ center conductor, one can see that the Cartesian field components in the conductor (i.e., below $x = -1.3\,\mu\text{m}$ in Fig. 2.11) differ not more than $0.5\,\%$ from the respective field components in the cylindrical problem. This error is smaller for higher frequencies and also for the outer conductor. As already mentioned, the sampling of the surface impedance takes place at $x = +1.5\,\mu\text{m}$. Again, using the term H_ϕ/r in (2.9) as an error term one can conclude that the planar field will deviate at $x = +1.5\,\mu\text{m}$ by $1.2\,\%$ from the cylindrical field. This estimate is conservative because plane waves are used instead of cylindrical waves for converting the surface impedance to an artificial material parameter. In case of a rough coaxial line, this partly corrects for the erroneous field, whereas the correction would be perfect in the case of a smooth coaxial line.

The main reasons for using a rough planar surface instead of a cylindrical one are the high accuracy, the numerical efficiency and the intrinsic error estimation of the multiple multipole solver. The numerical error of the field solver for the planar problem is 0.13% of the field values. The combined numerical and systematic error of the surface impedance is approximately 1.33%. At $f = 70\,\text{GHz}$ this leads to an uncertainty in the computed propagation constant of $\pm 0.02\frac{1}{\text{m}}$ for the attenuation constant and $\pm 0.06\frac{1}{\text{m}}$ for the phase constant.

Note that the errors due to the other steps of the real algorithm are comparatively small. The algorithm for the solution of the smooth transmission line problem has a numerical accuracy of more than 70 decimal

Table 2.3: Error Budget of 1.85 mm line at $f = 70\,\text{GHz}$

Type of Error	Effect on $\gamma\left[\frac{1}{\text{m}}\right]$
Surface Impedance	$\pm 0.02 \pm 0.06j$
Quadratic Approximation	$\pm 0.0001 \pm 0.02j$
Smooth Problem	$\pm 10^{-70} \pm 10^{-70}j$
Total Error	$\pm 0.02 \pm 0.08j$

digits. Obviously, this is much more than ever needed since neither the diameters nor the material properties are known so precisely.

Finally, the quadratic approximation in section 2.5.2 has some impact. The respective numerical error is less than $\pm 0.0001\frac{1}{\text{m}}$ for the real part and less than $\pm 0.02\frac{1}{\text{m}}$ for the imaginary part of the propagation constant.

An overview of the errors is given in Table 2.3. Obviously the error of the surface impedance determines the limits of accuracy. Smaller conductor diameters will increase the systematic error of the surface impedance, whereas higher frequencies will reduce its numerical error.

2.5.4 Measurement

This section describes the measurements which have been performed to verify the calculations described in the previous sections. For the sake of completeness, a comparison to other computational approaches is given.

The propagation constants of 2.4 mm and 1.85 mm coaxial transmission lines are measured with a VNA and the Multical computer program, see [12] and [13]. In both cases the propagation constant is determined by a line reflect line (LRL) calibration which does not make use of the thru standard. This is important to minimize the effects of connectors.
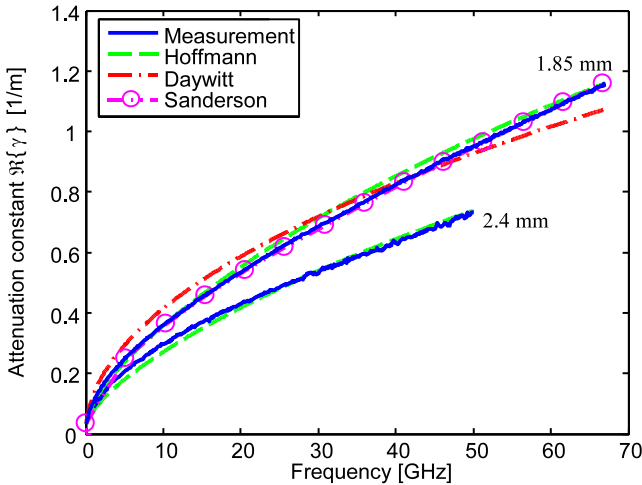
Figure 2.15: Attenuation constant Re $\{\gamma\}$ of 1.85 mm and 2.4 mm coaxial transmission lines over frequency. Curves ending at 50 GHz refer to 2.4 mm lines. Note that the traces Measurement, Hoffmann, Daywitt and Sanderson for 1.85 mm lines overlay each other. For the 2.4 mm lines, only the traces Measurement and Hoffmann are depicted.

Nonetheless, the lines within a calibration kit show slightly different propagation constants due to variances in the connectors of the lines and in the lines themselves, see Fig. 2.15 and 2.16. The transmission lines are part of Agilent LRL calibration kits. The mechanical and electrical data of the lines are given in appendix C.

The parameters listed in Table C.3 in appendix C are used to compute the propagation constant. All quantities listed in the first column are defined in Figs 2.8 and 2.9. The columns Daywitt and Sanderson refer to algorithms described in [5] and [8].

Figure 2.15 shows the attenuation of the lines, whereas Fig. 2.16 gives the difference Im $\{\gamma - jk_0\}$ (phase constant of the lines minus vacuum wave number). The conductivity[3] in Daywitt's algorithm has been tuned such that the attenuation matches the measurement. However, it is not possible to achieve the measured phase constant with the same conduc-

---

[3]The conductivity does not depend on the frequency.
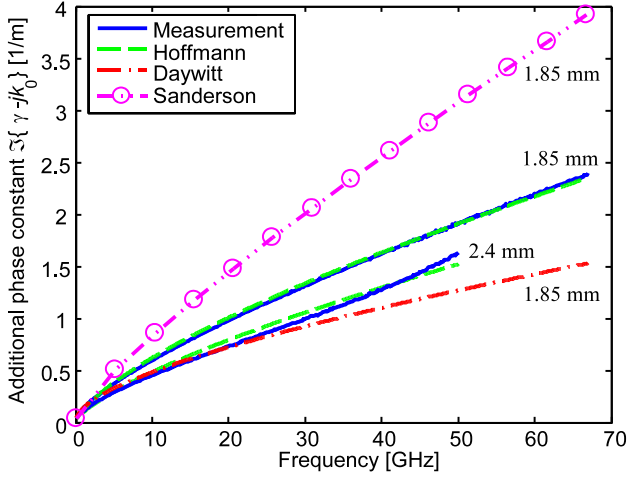
Figure 2.16: Phase constant $\mathrm{Im}\left\{\gamma\right\}$ of $1.85\,\mathrm{mm}$ and $2.4\,\mathrm{mm}$ coaxial transmission lines minus vacuum wave number k_0 over frequency. Curves ending at $50\,\mathrm{GHz}$ refer to $2.4\,\mathrm{mm}$ lines. The number of traces is the same as in Fig. 2.15.

tivity. This also holds for Sanderson's formulas. Contrary to these approaches the algorithm described here matches both quantities. Among all input parameters only the unknown conductivity of beryllium copper was tuned to match the experiment. The tuning can be used as an indirect measurement of the base material conductivity. The result of the indirect measurement is $\sigma_3 = 1.6 \times 10^7 \frac{\mathrm{S}}{\mathrm{m}}$, see as well Table C.3.

For some frequencies the deviations between the computed propagation constant and the measured propagation constant are larger than predicted in Table 2.3. This can be attributed mainly to connector effects. A less important factor are incorrect material parameters or dimensions.

2.6 Transmission line theory, ports and S-parameters

In the previous sections, the electromagnetic fields of the fundamental modes in cylindrical structures were computed. Depending on the direction of propagation the electromagnetic fields of one mode are called

forward or backward wave. Transmission line theory models these forward and backward waves by the propagation constant, which has been computed in the previous sections, and the characteristic impedance.

The characteristic impedance is the ratio of line voltage and line current of a single wave. The line current is defined as the current in one conductor and the line voltage is defined as the voltage between the conductors. This definition of the characteristic impedance is only unique for the TEM mode. In the TEM regime the characteristic impedance is

$$Z_0 = \frac{1}{2\pi} \sqrt{\frac{\mu}{\epsilon}} \ln \frac{b}{a}. \tag{2.54}$$

For lossy lines with a QTEM mode, the voltage and current of the line are no longer stringently defined. E.g., the current in the center conductor and outer conductor of a lossy coaxial line are not equal due to the displacement current in the dielectric. Thus a more general definition of the characteristic impedance is needed. As proposed in [4], the line current is defined as

$$I_s = 2\pi a H_\phi(a). \tag{2.55}$$

Where a is the radius of the center conductor and H_ϕ the tangential magnetic field. The average power of the mode is defined on a cross section of the coaxial transmission line as

$$P_s = \frac{1}{2} \int\limits_0^\infty \int\limits_0^{2\pi} \left(\vec{E}_r \times \vec{H}_\phi^* \right) \cdot \vec{n} \; r \; d\phi \; dr. \tag{2.56}$$

Where $\vec{n}$ is the normal vector of the cross section pointing in the direction of propagation. With the average power of the mode, one can compute the characteristic impedance

$$Z_{0s} = \frac{2P_s}{|I_s|^2}. \tag{2.57}$$

In the case of rough conductors, the concept of characteristic impedance has to be further adapted. For the periodic line, the mean value of characteristic impedance is defined by using the radius of the center conductor a_r and the magnetic field of the "slow" component for the measurement of the current

$$I_r = 2\pi a_r H_{\phi 0}(a_r). \tag{2.58}$$

The radius a_r is the distance between the center of the inner conductor and the center of the roughness profile. Here, the mid between the highest peak and the deepest valley of the roughness profile is called the center of the roughness profile. Note that definition (2.58) implies a non causal characteristic impedance, [16]. The differences between (2.58) and a definition according to [16] are negligible. Thus, simplicity and sufficient accuracy justify the use of (2.58). The power of the mode is defined and computed from the "slow" electromagnetic field in the dielectric

$$P_r = \frac{1}{2} \int\limits_0^\infty \int\limits_0^{2\pi} \left(\vec{E}_{r0} \times \vec{H}_{\phi 0}^* \right) \cdot \vec{n} \ r \ d\phi \ dr. \qquad (2.59)$$

Again, from current and power the characteristic impedance can be computed

$$Z_{0r} = \frac{2P_r}{|I_r|^2}. \qquad (2.60)$$

It should not be concealed that the definitions of the characteristic impedance for lossy smooth and lossy rough transmission lines are not stringent. The main motivation for defining a characteristic impedance is the possibility to compute reflection coefficients which should be as accurate as possible. The goal of accurate reflection coefficients renders some definitions of the characteristic impedance more suitable than others, but it does not designate one correct definition. This can be easily demonstrated on the choice of the integration path for the current. The goal of accurate reflection coefficients clearly shows that the integration path should be somewhere in the dielectric but it does not define at which radius it should be. A similar reasoning holds for the characteristic impedance of rough lossy lines.

Characteristic impedance and propagation constant are linked to the four parameters: inductance L', resistance R', capacitance C' and conductance G' per unit length. These parameters are combined to $Z' = R' + j\omega L'$ and $Y' = G' + j\omega C'$. They are defined as

$$Z' = \gamma Z_0, \ Y' = \frac{\gamma}{Z_0}. \qquad (2.61)$$

Transmission line theory assumes monomode operation of the coaxial line. In reality there are always electromagnetic fields of higher modes in

a transmission line. In VNA measurements they are weak compared to the electromagnetic fields of the fundamental mode, see section 2.2. The complete electromagnetic field on an area i can be projected on forward and backward waves

$$\vec{F}_i = a_i \vec{F}_i^+ + b_i \vec{F}_i^- + \vec{X}_i, \tag{2.62}$$

where $\vec{F}_i^+$ and $\vec{F}_i^-$ are the electromagnetic fields of the forward and backward wave respectively. The practically very small field $\vec{X}_i$ stems from other modes with stronger attenuation characteristic. The area i is called port area. It delimits a region which is orthogonal to the direction of propagation. The forward and backward waves are normalized to transmit one Watt through the port area. This can be written as

$$P_i^+ = \mathrm{Re} \left\{ \frac{1}{2} \int_S \left(\vec{E}_i^+ \times \vec{H}_i^{+*} \right) \cdot d\vec{S} \right\} = 1\,\mathrm{W} \tag{2.63}$$

$$P_i^- = \mathrm{Re} \left\{ \frac{1}{2} \int_S \left(\vec{E}_i^- \times \vec{H}_i^{-*} \right) \cdot d\vec{S} \right\} = -1\,\mathrm{W}. \tag{2.64}$$

Here S denotes the port area. The projection of the total field on forward wave, backward wave, and remaining field is made in such a way that the remaining field carries minimum power.

Now several ports of a device can be considered. The ports are defined in such a way that the forward wave injects power to the device. Injecting power at one port and observing the backward waves at all ports defines the ratios

$$S_{ji} = \frac{b_i}{a_j}, \tag{2.65}$$

where i is the output port and j is the input port. More such ratios are defined by consecutively exciting all ports and measuring the resulting backward waves. The double index ji can be used to arrange the ratios into a matrix of quadratic shape. This matrix becomes an S-matrix by specifying the characteristic impedance of each port. The S-matrix can be transformed in such a way that the characteristic impedance of each port is set to a prescribed reference impedance, see appendix A. In [11] the transformed S-matrix is called pseudo S-matrix and the original traveling

wave S-matrix is just called S-matrix. Here both types are called S-matrix and if necessary the reference impedance is given.

From the above one can conclude that S-parameters are a very abstract measure. First, one has the electromagnetic fields in a port area. They are projected on modes. From this projection the wave amplitudes a_i and b_i are defined. They define scattering ratios S_{ji} which in turn are assembled to a matrix. Then the characteristic impedances of the transmission lines at the port areas are evaluated. With these characteristic impedances the previously defined matrix is converted to a normalized S-matrix.

For the computation of traceable S-parameters, it is necessary to state uncertainties for the normalized S-matrix. The required input data for this computation are the uncertainties of the involved dimensions, of the material parameters, and the uncertainties of the computational methods. The final computation of uncertainties is quite complicated and is not further pursued here. For further information see [17] and [18].

3 Coaxial Connectors and Standards

Abstract — The introduction of this chapter lists all commonly available coaxial standards and gives their respective advantages and disadvantages. The first section is dedicated to the modeling of plain transmission lines. After this, two models of the $1.85\,$mm connector are presented: a 3D electromagnetic simulation model and a mixed approach consisting of a 3D electromagnetic simulation plus 2D capacitance calculations. Next, an interpolation tool for a database is described. The database consists of S-parameters resulting from different connector geometries. The last section is dedicated to the modeling of offset short and air line standards.

3.1 Introduction

An uncalibrated VNA is a very precise but not very accurate measurement instrument. This means it will always give nearly the same measurement result for a given DUT but the measurement result may be far away from the true value. This unpleasant fact is removed by calibration of the VNA. In other words, one has to measure DUTs with known S-parameters, called standards, to correct for the systematic errors of the VNA.

To cover frequencies up to $70\,$GHz in a $Z_0 = 50\,\Omega$ system, one has to use coaxial standards, which have a center conductor diameter of less than $0.81\,$mm. It is nearly impossible to manufacture slotless connectors with such small diameters. However, slotted connectors have to be characterized because they have non negligible influence on the S-parameters of standards. New concepts for modeling slotted connectors have been developed. The resulting models are used to make the models of calibration standards more accurate.

There are many different kinds of coaxial standards for VNA calibration. Fixed load and sliding load are energy absorbing standards. A fixed load consists generally of a connector, a piece of transmission line and a load element, see Fig. 3.1a. The sliding load is constructed in the same

Reference Plane   Connector   Offset Line   Load Element
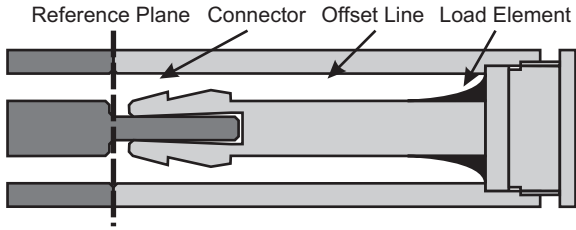
Figure 3.1a: Longitudinal cut through a female load. The load consists of a connector, a piece of transmission line and a load element. In the case of a sliding load, the load element is moveable.

Reference Plane   Connector   Offset Line   Dielectric Support
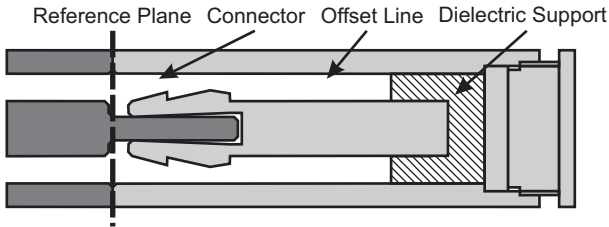
Figure 3.1b: Longitudinal cut through a female open. The open consists of a connector, a piece of transmission line and the dielectric support of the center conductor.

Reference plane   Connector   Offset Line   Short Plane
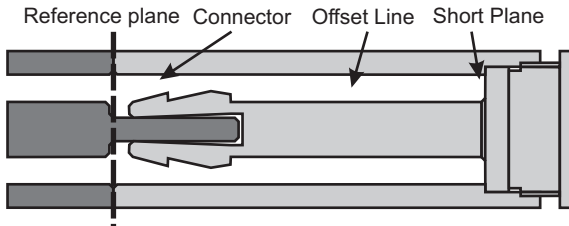
Figure 3.1c: Longitudinal cut through a female short. The short consists of a connector, a piece of transmission line and the short plane.

way as the fixed load but the load element is movable, thus the length of the transmission line between connector and load element is adjustable.

Open and short are energy reflecting standards. An open consists of a connector, a piece of transmission line and an insulating piece of plastic which keeps the center conductor in place without making galvanic contact to the outer conductor, see Fig. 3.1*b*. The short does not require the insulating plastic because the center conductor makes direct galvanic contact to the short plane. There are two types of shorts: offset shorts and flush shorts. Offset shorts have an offsetting line section. Line section and short plane are often manufactured as a single piece, see Fig. 3.1*c*. The flush short is a short where the short plane is located on the reference plane of the connector. The phase response of the flush short is mainly determined by the surface impedance of the short plane, whereas the phase of the offset short moves as a function of the offset length.

Standards which do not entirely consist of metal often show considerable differences between their computed S-parameters and actual S-parameters. These differences arise because of the inexact characterization of the non metallic parts. E.g., the insulating plastic of an open is quite difficult to characterize because the permittivity of the plastic depends largely on the way the part was manufactured. For this reason, only standards which consist of metal, i.e., shorts and air lines, are treated here. These are so called primary standards which can be used for traceable calibrations.

Air lines are two port standards. They consist of a connector on each side and a piece of transmission line in-between. The thru, a direct connection of the VNA test ports, can be considered as a special kind of air line with one connector and zero length. The concepts propagation constant and characteristic impedance were discussed in the previous chapter and are now used for the definition of standards.

3.2 Plain transmission line

The plain coaxial line of an air line standard is not completely uniform but shows diameter variations, eccentrically placed inner conductor and deformed cross sections. According to [19] the diameter variations are the most important parameters. Diameter profiles of center and outer conductor are depicted in Fig. 3.2 and 3.3. Note that the measured diameter

variations of the slotted section will be taken into account by the model of the connector. To account for the remaining diameter variations, the line is sliced into segments of 0.1 mm length. This fine discretization guarantees that each line segment is very uniform. The propagation constant $\gamma_r(a, b)$ of a rough transmission line with radii a and b and its characteristic impedance $Z_{0r}(a, b)$ are needed to write the S-matrix of each segment. To compute these quantities, the propagation constant $\gamma_r(a_0, b_0)$ and characteristic impedance $Z_{0r}(a_0, b_0)$ of a rough air line with $a_0 = 0.8036\,\mathrm{mm}/2$ and $b_0 = 1.85\,\mathrm{mm}/2$ are computed. Then the propagation constant γ_s and characteristic impedance Z_{0s} of a smooth air line with radii a_0 and b_0 are computed with [5]

$$\delta = \sqrt{\frac{2}{\sigma\omega\mu}} \tag{3.1}$$

$$k = \omega\sqrt{\mu\epsilon} \tag{3.2}$$

$$d_0 = \frac{\delta\left(1 + \frac{b}{a}\right)}{4b\ln\left(\frac{b}{a}\right)} \tag{3.3}$$

$$F_0 = \frac{\frac{b^2}{a^2} - 1}{2\ln\left(\frac{b}{a}\right)} - \frac{\frac{b}{a}\ln\left(\frac{b}{a}\right)}{\frac{b}{a} + 1} - \frac{1}{2}\left(\frac{b}{a} + 1\right) \tag{3.4}$$

$$C_0' = \frac{2\pi\epsilon}{\ln\left(\frac{b}{a}\right)} \tag{3.5}$$

$$L_0' = \frac{\mu\ln\left(\frac{b}{a}\right)}{2\pi} \tag{3.6}$$

$$R' = 2\omega L_0' d_0\left(1 - \frac{k^2 a^2 F_0}{2}\right) \tag{3.7}$$

$$L' = L_0'\left(1 + 2d_0\left(1 - \frac{k^2 a^2 F_0}{2}\right)\right) \tag{3.8}$$

$$G' = \omega C_0' d_0 k^2 a^2 F_0 \tag{3.9}$$

$$C' = C_0'\left(1 + d_0 k^2 a^2 F_0\right) \tag{3.10}$$

$$Z' = R' + j\omega L' \tag{3.11}$$

$$Y' = G' + j\omega C' \tag{3.12}$$

$$\gamma_s = \sqrt{Z'Y'} \tag{3.13}$$

$$Z_{0s} = \sqrt{\frac{Z'}{Y'}}. \tag{3.14}$$

The characteristic impedance Z_{0r} and propagation constant γ_r of a line with inner and outer radii a and b are then interpolated by

$$Z_{0r}(a,b) = Z_{0r}(a_0,b_0) + Z_{0s}(a,b) - Z_{0s}(a_0,b_0) \tag{3.15}$$

$$\gamma_r(a,b) = \gamma_r(a_0,b_0) + \gamma_s(a,b) - \gamma_s(a_0,b_0). \tag{3.16}$$

With these values the S-matrix of each transmission line segment is computed

$$\mathbf{S}_i = \begin{pmatrix} 0 & e^{-\gamma_r(a,b)l_i} \\ e^{-\gamma_r(a,b)l_i} & 0 \end{pmatrix}. \tag{3.17}$$

Where l_i is the length of the i-th segment and $\gamma_r(a,b)$ is the propagation constant of the rough coaxial line in the i-th segment. Note that the S-matrices can not be cascaded yet because of differing reference impedance $Z_{refi} = Z_{0r}(a,b)$. Therefore, one transforms all S-matrices with (A.3) and (A.1) to $Z_{ref} = 50\,\Omega$. Finally, one converts these S-matrices to T-parameters (A.4), cascades them (A.5), and converts back to the total S-parameters of the entire transmission line (A.6). How to model the connectors at the ends of such a line will be discussed next.

3.3 The slotted 1.85 mm connector

Historically, electrical characteristics of coaxial connectors are first computed by Whinnery et al. [20], [21]. Mode matching theory was used to develop simple equivalent circuits for steps in wave guides and coaxial lines. Mode matching can be used to compute the S-parameters of simple geometries like steps, whereas in particular narrow gaps pose a problem. [20] and [21] are the basis for the chapter on coaxial discontinuities in [22]. Somlo [23] used [21] to provide computer calculated and therefore more accurate charts and tables of the step capacitance.

MacKenzie and Sanderson [24] gave another formula to compute the voltage standing wave ratio (VSWR) of a pin gap in conjunction with a slotted female contact. The assumption, that only the TEM mode exists in the coaxial line, leads to a formula based on capacitance computation of
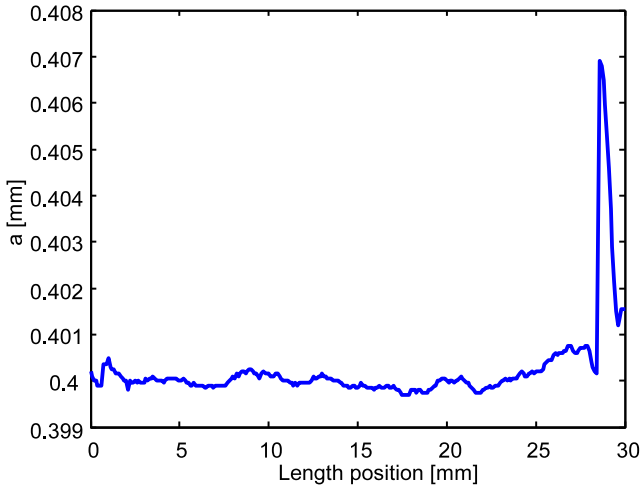
Figure 3.2: Radius of center conductor of a 1.85 mm air line. The bump on the right side is the female connector. The U95 measurement uncertainty for the radius is approximately 0.5 μm.

the different sections of the coaxial connector. The approach of computing the capacitance per unit length is useful in the case of TEM-like wave propagation, but it is not very accurate if the electromagnetic fields under consideration are very different from the TEM mode.

Later, computer simulations were used to solve coaxial field problems. Gwarek [25] used the finite difference time domain (FDTD) method to investigate coaxial discontinuities. For the finite element method (FEM) a formulation for coaxial problems was found by Wilkins [26]. Results were cross-checked with the mode matching method. Szendrenyi [27] used a commercial FEM field solver (HFSS) to investigate the effects of pin gaps in cylindrically symmetric structures.

General information on coaxial connectors can be obtained from the P287 standard [28]. A literature list with papers on coaxial connectors is given in [29].

In [30] non cylindrically symmetric connectors are investigated with FDTD and FEM methods. The results are used to generate a database which allows to determine the S-parameters of a slotted connector without
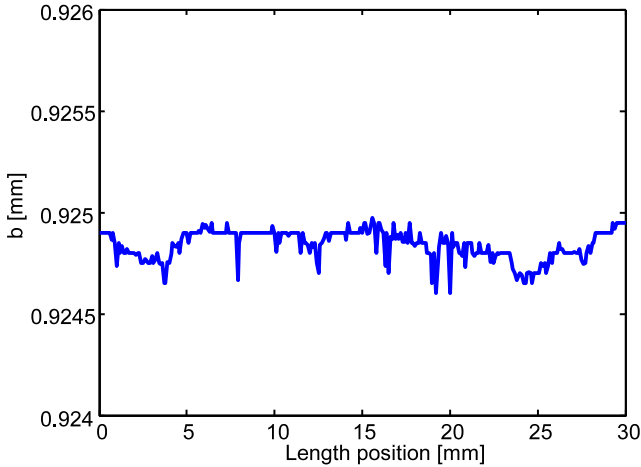
Figure 3.3: Radius of outer conductor of a 1.85 mm air line. The U95 measurement uncertainty for the radius is approximately $0.75\,\mu$m.

using an electromagnetic field simulator. Using this database the effects of very narrow pin gaps are investigated. The following is a more detailed version of [30].

3.3.1 Geometry of the connector

Each manufacturer has its own design of the 1.85 mm connector because the P287 standard does not define the shape of the female contact fingers. Even connectors from one manufacturer differ among each other due to tolerances in production. These two sources of dimension variability motivate the following definition of parameterized geometries.

The geometry of the slotted connector shown in Figs 3.4-3.9 is best described by its production process. The production of the male side of the connector is rather trivial. To manufacture the female part of the connector, one usually lathes the end of the center conductor to the shape depicted in Fig. 3.4. Next, the borehole is drilled and chamfered and slots are cut according to Fig. 3.5. Finally, the contact fingers are bent to the right position. The assembled connector is depicted in Figs. 3.6, 3.7 and 3.8. Fig. 3.6 shows a longitudinal cut while Fig. 3.7 gives a lateral cut
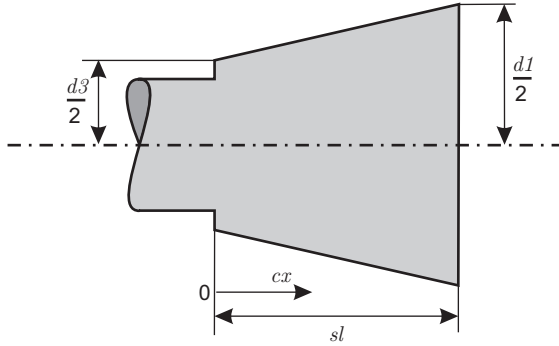
Figure 3.4: Lathing cross section for the female part of a 1.85 mm connector. The coordinate cx is used to designate positions in the slotted section. For better visibility the differences between d_1 and d_3 are exaggerated.
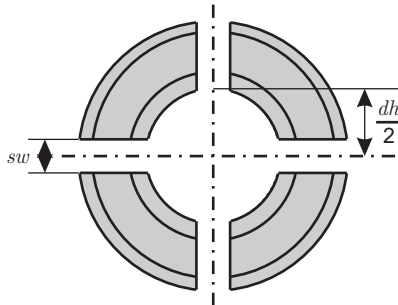
Figure 3.5: Front of female part after drilling the hole and cutting the slots.
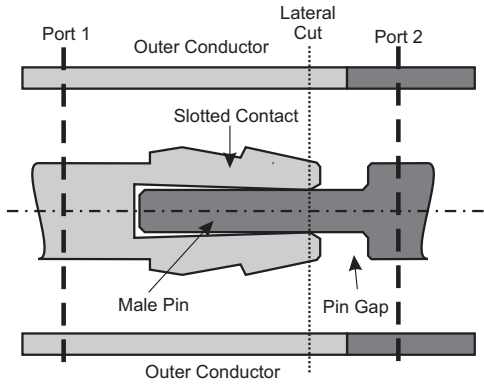
Figure 3.6: Longitudinal cut through the connector. The lateral cut shown in Fig. 3.7 lies in-between the S-parameter ports. The main elements of the geometry are the pin gap and the slotted female contact. The height profile of the slotted female contact is exaggerated for reasons of visibility.
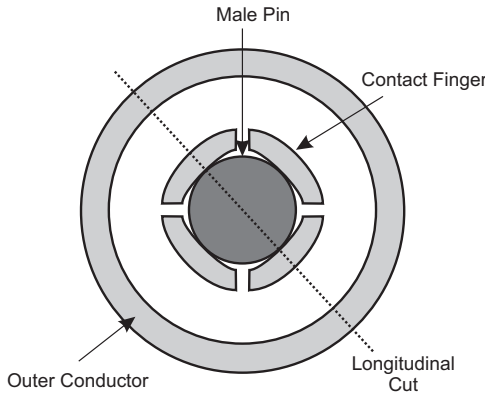
Figure 3.7: Lateral cut through the symmetry axis on the height, where the female contact fingers make galvanic contact to the male pin. The diagonal dotted line indicates the cut shown in Fig. 3.6 and Fig. 3.8.
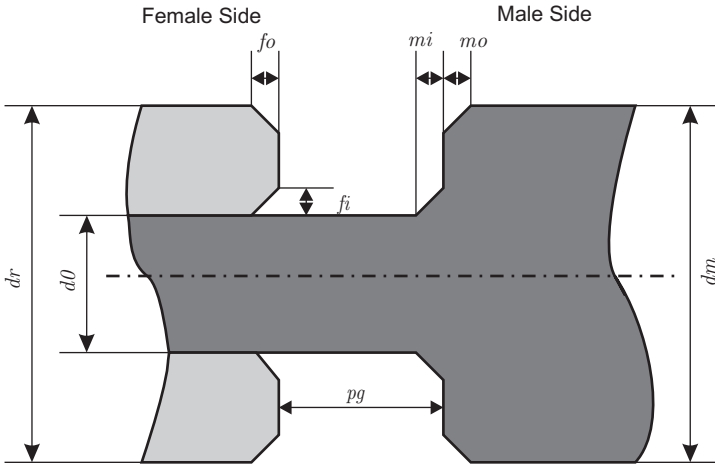
Figure 3.8: Details of the pin gap. All edges are chamfered to 45 degrees. See Table 3.1 for the naming and range of the geometry parameters.
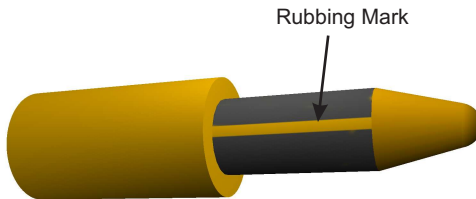
Figure 3.9: Model of a male pin with rubbing mark. The male pin was covered with Prussian blue. The thin, bright rubbing mark is a result of repeated connections.

through the slotted female contact. Further geometrical details of the pin gap region are given in Fig. 3.8.

A last detail of the connector geometry, which can not by illustrated with the production process, is the width of the contact between contact finger and male pin, see Fig 3.9. The contact-width was measured with Prussian blue, i.e., the male pin was covered with a thin layer of Prussian blue and the mating process was repeated several times in the same angular position using a watchmakers lathe. Afterwards the contact-width was determined by inspection with a microscope to be approx. $80\,\mu$m.

The variables mentioned in the previous description and figures are listed with the according ranges in table 3.1.

Table 3.1: Meaning of Variables

Parameter	Range	Full name
sl	$0\ldots2000\,\mu$m	Slot Length
sw	$30\ldots150\,\mu$m	Slot Width
$d1$	$800\ldots880\,\mu$m	Top End Diameter
$d3$	$800\ldots880\,\mu$m	Bottom End Diameter
dh	$511\ldots652\,\mu$m	Hole Diameter
fo	$5\ldots30\,\mu$m	Female Outer Chamfer
fi	$30\ldots110\,\mu$m	Female Inner Chamfer
pg	$1\ldots100\,\mu$m	Pin Gap
mi	$9\ldots30\,\mu$m	Male Inner Chamfer
mo	$5\ldots30\,\mu$m	Male Outer Chamfer

Table 3.1: Continuation

Parameter	Range	Full name
f	$0 \ldots 71\,\text{GHz}$	Frequency

3.3.2 Electromagnetic simulation

The EM-simulation of the setup given in Fig. 3.6 was carried out with two different simulation tools. CST Microwave Studio[1] is a finite integration time domain (FIT) code, which uses structured grids. The FIT technique is very similar to the FDTD technique. HFSS[2] is a finite element frequency domain code using unstructured meshes.

Under HFSS it is important to mesh the curved surfaces sufficiently fine. We found that at least 90 nodes on the circumference of conductors are needed. Otherwise the field simulator produced modes strongly different from the coaxial TEM mode thus falsifying the result. The standard rule that regions with big field gradients should have finer meshing than other regions applies as well. In contrast, Microwave Studio yields good results with automatic meshing.

Numerical simulations will hardly ever deliver exact results. Therefore it is important to validate the numerical results. Evidence for accurate simulation results are (1) convergence with finer mesh, (2) plausibility of obtained S-parameters and (3) agreement of the results from both approaches. Simulation results from both programs converged with finer mesh and also the S-parameters appeared plausible when changing the geometry. For example using bigger outer chamfers has a similar effect as a bigger pin gap. Results of both simulation programs showed an agreement for representative samples $|S_{11\text{HFSS}} - S_{11\text{CST}}| < 0.001$. These observations lead to the conclusion that the results have an uncertainty of ± 0.001 over the whole frequency range.

Using a PC of the latest generation, the simulation of one geometry takes between 20 min and 5 h depending on the pin gap. Small pin gaps

---

[1]CST Microwave Studio Version 5.1.3 June 27. 2005
[2]Ansoft HFSS Version 9.2.1 May 7. 2004
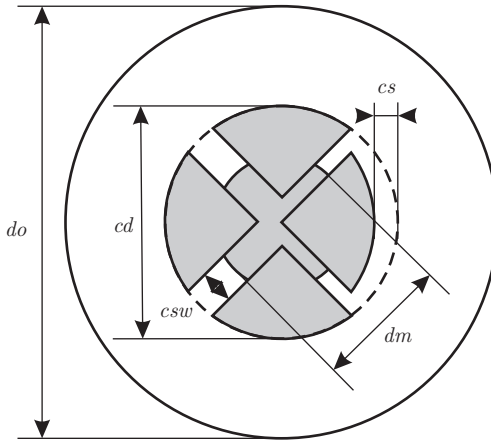
Figure 3.10: Geometry of cross section of a coaxial 1.85 mm connector. The dimensions $do = 1.85$ mm and $dm = 511\,\mu$m are standardized in [28]. The diameter of the disk sections cd and the spacing csw between them is given in (3.19) and (3.18). The disk sections are moved towards the center by cs, see (3.20). Here only one section is moved to illustrate the process.

need very fine meshing, and in the time domain simulation also very fine time steps. Therefore simulation time increases with decreasing pin gap.

For parameter studies these simulation durations would be too long, thus the connector is split into two parts. The first part is the section of the connector which is slotted and the second part contains the pin gap. The subdivision is motivated by the fact that the electromagnetic fields of the slotted part are TEM-like, whereas the fields in the pin gap section can be regarded as nearly static. Comparison of S-parameters which are computed for the complete connector as depicted in Fig. 3.6 and S-parameters which are computed with the subdivided connector showed an agreement of $|S_{11\text{div}} - S_{11\text{CST}}| < 0.001$.

3.3.3 The subdivided model

The electrical model of the slotted section depends on the dimensions of the contact fingers and of the male pin. These dimensions can either come from measurements or they are a result of a simplified model. In
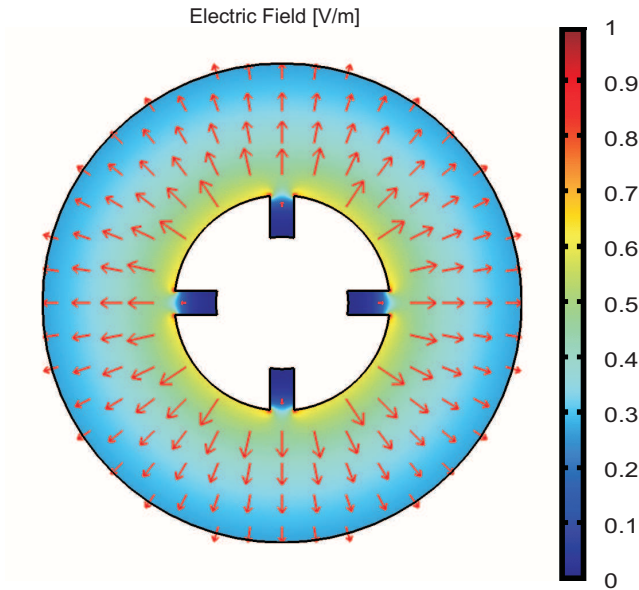
Figure 3.11: Absolute electric field in the slotted section of a coaxial 1.85 mm connector. The color indicates the absolute electric field $|\vec{E}|$ and the arrows indicate strength and direction of the electrical field $\vec{E}$.

the simplified model of the geometry, the parameters sl, sw, $d1$, $d3$ and dh have to be set (Fig. 3.10). The dimensions of the cross section as a function of the longitudinal position cx are given by

$$csw = sw \tag{3.18}$$

$$cd = \frac{d1 - d3}{sl}cx + d3 \tag{3.19}$$

$$cs = \frac{dh - dm}{2}(1 - \frac{cx}{sl}). \tag{3.20}$$

The variable cx is defined in Fig. 3.4. Next, the capacity per unit length of the cross section is computed, see Fig. 3.11. From the capacitance an equivalent diameter can be computed

$$a' = b\,e^{-\frac{2\pi\epsilon}{C'}}. \tag{3.21}$$
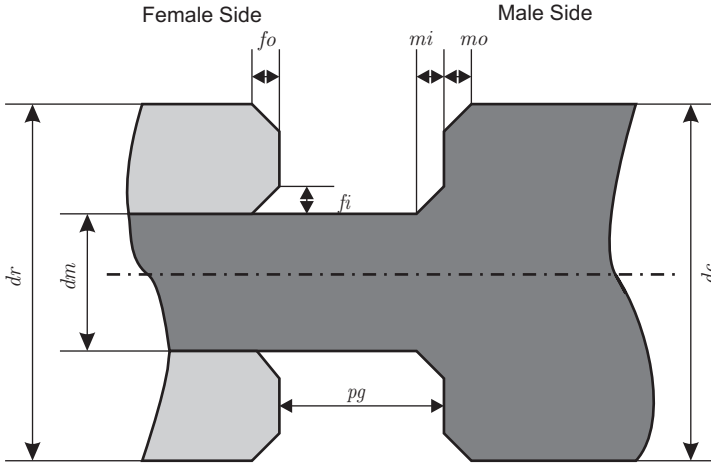
Figure 3.12: Geometrical model of pin gap section. The diameter dr replaces the slotted section, see (3.21). The diameters $dm = 511\,\mu\text{m}$ and $dc = 803.6\,\mu\text{m}$ are set to the values specified in [28].

Here C' is the capacitance of the cross section per meter and $\underline{\epsilon}$ is the permittivity of the dielectric. Again b designates the radius of the outer conductor. Using b and a' with the transmission line algorithm described in section 3.2 yields the S-parameters of the slotted section.

The model of the pin gap shows a circular symmetry. It is depicted in Fig. 3.12. The diameter of the coaxial line which replaces the slotted section is set to $dr = 2a'$, where a' is the equivalent radius at the top of the slotted contact. The S-parameters of this section are computed with CST Microwave Studio. Finally, the S-parameters of the slotted section and of the pin gap are cascaded.

3.3.4 Database lookup

An interpolation tool has been developed to even further speed up the computation of connector S-parameters. The interpolation tool requires only the geometry parameters listed in Table 3.1 to calculate the S-parameters in a few seconds. The resulting speed up factor is about 3000 as opposed to brute force EM-simulation.
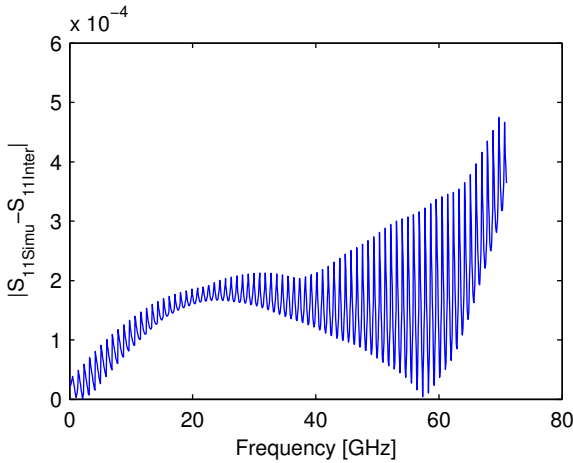
Figure 3.13: Absolute error of the interpolation tool versus CST Microwave Studio simulation results $|S_{11\mathrm{Simu}} - S_{11\mathrm{Inter}}|$ over the frequency. The ripple stems from the search to the closest point in the database.

The interpolation tool consists of two databases. One for the capacitances per meter of the cross sections and another for the S-parameters of the pin gap. There are 153 capacitances of different cross sections stored and 384 S-matrices of pin gap sections.

The database contains samples arranged in a grid where each grid point is a geometrically possible combination of values given in Table 3.2. E.g. csw = $50\,\mu$m and cs = $70.7\,\mu$m is not a possible combination, see Fig. 3.10. The interpolation algorithm uses the data points in the database, which are closest to the requested parameter combination and performs an n-th degree polynomial interpolation for each of the parameters. The polynomial degree is $n = 1$ (linear interpolation) if only two values are available in the database. If 3 values are available, $n = 2$ is used and for 4 available values $n = 3$ is used. If 5 values are available, $n = 3$ is used and the coefficients of the polynomial are determined with a least squares fit. If more than 5 values are available, $n = 3$ is used and the coefficients are determined with a least squares fit from the 5 values which are closest to the requested point. The used order of the polynomial and the number of computed values per parameter are a result of practical experiments.

Thereby it was observed that additional computed values are only helpful if they are in the neighborhood of the requested point. Another practical observation is that increasing the order of the polynomial is useful up to $n = 3$, but using $n = 4$ degraded the accuracy of the approximation.

Table 3.2: Points in Database

Parameter	Points	Interpolation Order
csw	$30, 50, 110, 150\,\mu\mathrm{m}$	3
cd	$0.8, 0.8036, 0.81, 0.82, \ldots, 0.88\,\mathrm{mm}$	3
cs	$0, 14.1, \ldots, 70.7\,\mu\mathrm{m}$	3
dr	$0.78, 0.80, 0.82, 0.84\,\mathrm{mm}$	3
fo	$5, 30\,\mu\mathrm{m}$	1
fi	$30, 70, 110\,\mu\mathrm{m}$	2
pg	$1, 34, 67, 100\,\mu\mathrm{m}$	3
mi	$9, 30\,\mu\mathrm{m}$	1
mo	$5, 30\,\mu\mathrm{m}$	1
f	$0, 0.071, 0.142, \ldots, 71\,\mathrm{GHz}$	3

In order to verify this approach, the reflection coefficient $S_{11\mathrm{Simu}}$ of a connector with parameters given in Table 3.3 has been computed with Microwave Studio and compared with the respective quantity $S_{11\mathrm{Inter}}$ obtained by the interpolation tool.

The quality of the interpolation tool can be assessed by the quantity $|S_{11\mathrm{Simu}} - S_{11\mathrm{Inter}}|$ plotted in Fig. 3.13. The ripple in Fig. 3.13 stems

Table 3.3: Parameter Settings for Examples

Parameter	Fig. 3.13	Fig. 3.14	Fig. 3.15
sl	$1.4\,\mathrm{mm}$	$1.4\,\mathrm{mm}$	$1.4\,\mathrm{mm}$
sw	$30\,\mu\mathrm{m}$	$30\,\mu\mathrm{m}$	$30\,\mu\mathrm{m}$
$d1$	$854\,\mu\mathrm{m}$	$854\,\mu\mathrm{m}$	$854\,\mu\mathrm{m}$
$d3$	$803.6\,\mu\mathrm{m}$	$803.6\,\mu\mathrm{m}$	$803.6\,\mu\mathrm{m}$
dh	$540\,\mu\mathrm{m}$	$540\,\mu\mathrm{m}$	$540\,\mu\mathrm{m}$
fo	$10\,\mu\mathrm{m}$	$5\,\mu\mathrm{m}$	$5\,\mu\mathrm{m}$
fi	$50\,\mu\mathrm{m}$	$100\,\mu\mathrm{m}$	$30\,\mu\mathrm{m}$
pg	$50\,\mu\mathrm{m}$	$1,\ldots,100\,\mu\mathrm{m}$	$1,\ldots,100\,\mu\mathrm{m}$
mi	$10\,\mu\mathrm{m}$	$20\,\mu\mathrm{m}$	$20\,\mu\mathrm{m}$
mo	$10\,\mu\mathrm{m}$	$5\,\mu\mathrm{m}$	$5\,\mu\mathrm{m}$
f	$0,\ldots,71\,\mathrm{GHz}$	$0,\ldots,71\,\mathrm{GHz}$	$0,\ldots,71\,\mathrm{GHz}$

from the search to the closest point in the database. Errors are relatively big each time the requested parameter combination is in the mid between two database points on the frequency axis. The error becomes smaller when the requested parameter combination is close to a database point on the frequency axis.

3.3.5 Narrow pin gaps

Motivated by reports [31] on calibration inconsistencies between LRL calibration and Offset Short calibration, the effects of very small pin gaps were investigated. In the Offset Short calibration, the pin gaps are always well controlled. In the LRL calibration, depending on the operator, very small pin gaps can occur due to the floating center conductors of air lines. Departing from the trivial assumption: the smaller the pin gap the smaller the reflection factor, it was found that by careful design of the slotted female section it is possible to put the minimum reflection coefficient to a specific pin gap size. This is well known and called compensation, [24]. But very small pin gaps in combination with big female inner chamfers were found to provoke S-parameters, which are not conform to the afore mentioned reasoning. A drastic increase of the reflection factor at frequencies above $50\,$GHz can be observed for decreasing pin gaps. In Fig. 3.14 and 3.15 the effect is clearly visible for the $1\,\mu$m and $5\,\mu$m pin gaps. Note that both figures use the same setup except for differences in the female inner chamfer.

The phenomenon can be explained by field plots obtained from the EM-simulation. The skin effect restricts the current to the surface of the conductor. Due to the female inner chamfer, there is an empty volume with a surface current. Energy is stored in this volume in form of a magnetic field. The narrow pin gap between male side and female side stores energy in form of an electric field. The female inner chamfer volume and the pin gap can be seen as a resonant circuit. This resonant circuit is the explanation of the atypical S-parameters for narrow pin gaps.

3.4 Standards

3.4.1 Air line

Air lines and offset shorts can be decomposed to the building blocks connector, plain coaxial line and short plane. The S-parameter model of the connector and of the plain coaxial transmission line have already been described in the previous sections. Thus one can readily compute the S-parameters of an air line standard by cascading the S-parameters of its connectors and of the plain transmission line. This yields the S-parameters of the air line standard with attached connectors. Depending on the defi-
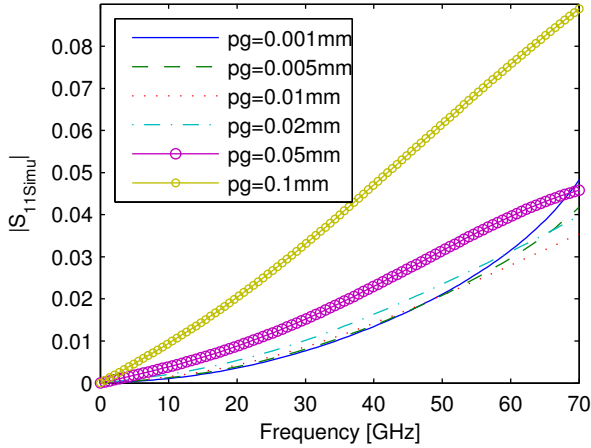
Figure 3.14: Reflection coefficient of connector with big female inner chamfer. The geometry parameters are given in Table 3.3.

nition of the port some parts, e.g. a slotted section, have to be subtracted from this model.

3.4.2 Offset short

The S-parameter model of the offset short is very similar to the model of an air line standard. The connector and the offsetting plain coaxial line are modeled with the already known S-parameter building blocks. The combination of these two building blocks yields S-parameters **S**. As a last building block, the short plane has to be added. Its reflection coefficient is computed according to [32]

$$Z_s = (1+j)\sqrt{\frac{\omega\mu}{2\sigma}} \tag{3.22}$$

$$Z_{0p} = \frac{Z_s}{2\pi}\ln\left(\frac{b}{a}\right) \tag{3.23}$$

$$\Gamma = \frac{Z_{0p} - Z_0}{Z_{0p} + Z_0} \tag{3.24}$$
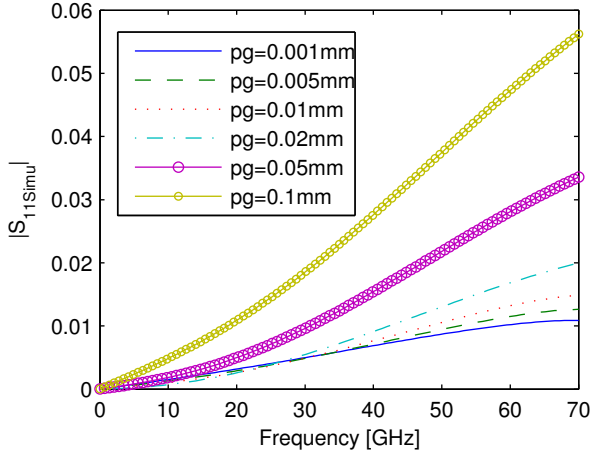
Figure 3.15: Reflection coefficient of connector with small female inner chamfer. The geometry parameters are given in Table 3.3.

This reflection coefficient is computed with the characteristic impedance of the line Z_0. Thus the reflection coefficient has to be normalized to $Z_{ref} = 50\,\Omega$. After this the system of equations which describes connector and line ($\mathbf{S}$) and the equation which contains the reflection coefficient Γ are written as one system. Finally, this system is solved for the input reflection coefficient.

Another less accurate possibility to compute the S-parameters of an offset short is to prescribe its model and to determine the parameters of the model during calibration, see [33]. This approach is particularly interesting if no reliable mechanical dimensions of the offset short are known.

4 Calibration Algorithms

Abstract — In the introduction of this chapter, the concepts of VNA calibration are sketched. Then a more detailed explanation of the VNA architecture and its modeling are given. In the subsequent section, some well known statistical models commonly used for VNA calibration are compared with the new statistical model. Next, the new statistical model is explained in detail. Then this statistical model is converted into a formula for calibration. As one of the last steps, the formula for calibration is solved numerically. Finally, the new algorithm and some well known calibration algorithms like Multical are tested for accuracy and stability.

4.1 Introduction

An uncalibrated VNA is a measurement instrument which gives raw S-parameters of a DUT. Raw means in this context that there is no correction applied to the S-parameters. The correction is required because the technical realization of the VNA maps the S-parameters of the DUT to the raw S-parameters. This mapping is of central interest for VNA measurements because if it is known, one can invert it and thus deduce the S-parameters of the DUT from the raw S-parameters.

The mapping can be represented as an S-matrix. A m-port VNA can be represented by a $2m \times 2m$ S-matrix. Depending on the architecture of the VNA some of the elements of the $2m \times 2m$ S-matrix will be set to zero. The remaining elements are depending on many factors and have to be determined. An underlying assumption of the representation of the VNA as a S-matrix is that all components of the VNA are linear.

Here, the position of the zero elements of the S-matrix describing the VNA is called structure of the VNA S-matrix. It depends on the architecture of the VNA and the measurement setup. In former times some two port VNAs had three directional couplers and three receivers. Now almost all two port VNAs have four receivers and couplers. In the following this modern two port VNA will be treated in detail. Nonetheless the presented

concepts are applicable to VNAs with arbitrary architecture and number of ports.

Once the structure of the VNA S-matrix is known, one has to determine the non-zero elements of the S-matrix. One can extract the coefficients by measuring standards and reading the raw S-parameters. After performing a sufficient number of measurements, one can write a system of equations which contains the S-parameters of the standard, the measured raw S-parameters and the non-zero elements of the VNA S-matrix. Depending on the structure of the VNA S-matrix and the used standards, the system of equations is often non-linear and thus not trivial to solve.

If additional standards are measured, one is confronted with an over-determined non-linear system of equations. Usually such a system has no exact solution. Nonetheless, it is useful to measure more standards than necessary because this allows one to correct for errors. The new Bayesian calibration algorithm, presented here, is derived from a statistical model of the calibration process. It uses this model to find a solution of the over-determined non-linear system. The presented algorithm is not restricted to a special kind of VNA architecture. Another important feature of the presented algorithm is its accuracy and robustness against poorly defined standards.

4.2 VNA architecture

The architecture of a two port VNA with four receivers is depicted in Fig. 4.1. The ports are the interface between the VNA and the DUT. The place where the S-parameters are physically measured in the VNA are the receivers. They digitize the amplitude and phase of the electromagnetic signal at their input ports and produce the raw S-parameters.

The relationship between the raw S-parameters and the S-parameters of the DUT is described by the VNA S-matrix. It is constructed from the S-parameters of the individual building blocks of the VNA, see Fig. 4.1.

The radio frequency (RF) source of the VNA is usually a temperature controlled crystal oscillator or an Yttrium Iron Garnett oscillator. The source signal frequency is usually multiplied or divided by adjustable phase locked loops. In terms of S-parameters, a source is a simple one port device which exhibits some reflectivity.

The transmission lines which connect the different building blocks are
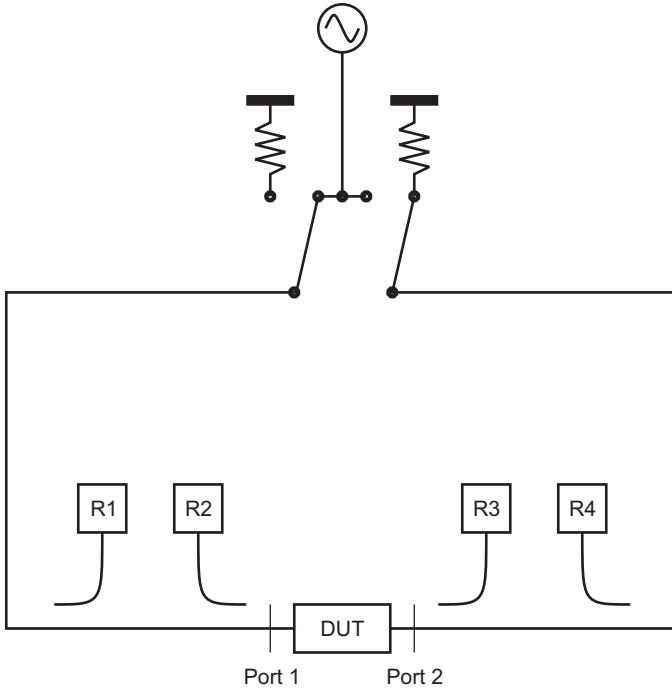
Figure 4.1: Schematic diagram of a two port VNA. The source can be switched either to port one or two. The signal is then split up via two directional elements to the receivers and to the DUT. The reference receivers R1 and R4 measure the amplitude and phase of the incoming wave, whereas the receivers R2 and R3 measure the reflected and transmitted waves.

usually semi rigid cables. They can be described with 2×2 S-matrices.

The directional elements are usually VSWR bridges or directional couplers. VSWR bridges are used up to approximately $f = 4\,\mathrm{GHz}$ and directional couplers are typically used for frequencies in the range of $f = 1 \ldots 100\,\mathrm{GHz}$. For high power applications, a circulator can be used as directional element. All these implementations of directional elements can be described with a 3×3 S-matrix.

The switch is either a mechanical one or a solid state switch. In both cases the switch can be described by a 3×3 S-matrix. Note that each

state of the switch requires one complete S-matrix for its description. If solid state switches are temperature controlled, they are more repeatable than mechanical switches.

The receivers are usually heterodyne receivers, but for economic reasons sometimes homodyne receivers are used. Both realizations are used to measure wave intensities. The ratios of the measured wave intensities are the raw S-parameters. In terms of S-parameters, a receiver is a reflective one port device.

The VNA S-matrix can be computed by writing all S-matrices of the components into one system of equations and solving for the incoming and outgoing wave quantities at the test ports and the sums of incoming and reflected wave quantities at the receivers. By rearranging, the S-matrix of the VNA can be constructed. The single elements of this matrix are often called error terms. The VNA S-matrix is not a classical S-matrix. While the test ports are classical ports with a characteristic impedance, the ports where the raw S-parameters can be read are logical ports. They consist of two separately measured wave intensities which are mathematically combined to form S-parameters.

Due to variations such as, e.g., temperature drift, cable bending, instable test port cables etc., it is not possible to compute one fixed S-matrix for a given VNA. Instead, the S-matrix of the VNA has to be determined for each measurement setup separately. This means the non-zero elements of the VNA S-matrix have to be determined or in other words the VNA has to be calibrated.

4.3 Introduction to calibration algorithms

Calibration consists of the measurement of standards and subsequently calculating the correction coefficients of the VNA. During the measurement of standards (Fig. 4.2) three different types of errors occur. First, the calibration standards introduce errors due to differences between the standards and their definitions (*error in standards*). Errors in standards are partly systematic but unknown and partly random. Second, the measurement instrument itself introduces random errors because the properties of the instrument change from measurement to measurement (*instrumentation error*). Third, reading the scales of the VNA introduces errors because only a finite number of digits are considered. This random error
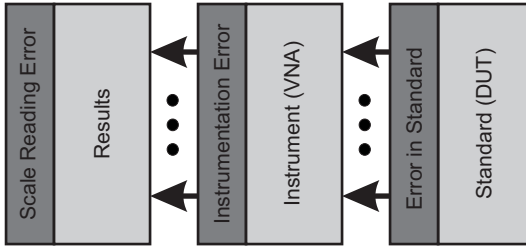
Figure 4.2: Model of the measurement process: The standard influences the VNA which produces raw S-parameters. Each part in this chain may potentially contribute errors (dark grey fields) which can be taken into account by the calibration algorithm.

is called the *scale reading error*.

Calibration schemes differ in how they treat these errors. Some schemes, e.g. the plain LRL in [34], simply ignore the errors and use a minimum number of standards. More advanced over-determined calibration schemes utilize an increased number of standards and minimize some of the errors to increase the measurement accuracy. Among microwave measurement instruments this principle was first applied to slotted lines and six port reflectometers, [35], [36] and [37].

For VNAs an over-determined version of the LRL scheme is given in [12]. It assumes and minimizes Gaussian errors in LRL standards but does not account for instrumentation errors. The Multical [13] computer program is based on this minimization technique. A more general calibration algorithm can be constructed by minimizing both Gaussian scale reading errors and Gaussian errors in the standards. Statistical^{TM} is a software program that uses this principle, [38] and [39]. As the impact of the different types of errors varies for different calibration schemes, it is sometimes reasonable to ignore some of these errors.

The algorithm presented here, see [40], minimizes instrumentation errors and errors in the standards because those are the most important errors. Scale reading errors are negligible for VNA measurements. The errors are described by an arbitrary (possibly non-Gaussian) probability density function (pdf). Utilizing Bayes' formula, a minimum variance un-

biased estimator for the VNA correction coefficients is developed. The numerical implementation of this estimator makes use of optimization techniques and Monte-Carlo integration. The algorithm is tested with the LRL calibration. In-house versions of Statistical$^{\text{TM}}$, Multical and a plain LRL algorithm are developed and compared to the new algorithm. The comparison highlights differences in accuracy and stability for extremely high or low system impedance, non-Gaussian S-parameter distribution of standards and poorly defined standards. It was found that the new algorithm is more stable and more accurate in all cases investigated.

4.4 Models of measurement and calibration

In this section a new mathematical model of the VNA measurement process is described. This model is used as a starting point for describing the calibration procedure which is essentially a measurement of known devices.

4.4.1 Model of the measurement process

Vector network analysis is a measurement process, in which the VNA interacts with the DUT. The outcome of this interaction is a set of measurement data which consists — assuming an m-port VNA — of the m^2 raw S-parameters of the DUT. For a mathematical description of the measurement process, three sets of variables are defined:

$\tilde{r}$: The m^2 raw S-parameters given by the VNA with $\tilde{r} \in \mathbb{C}^{m^2}$ or $\dim(\tilde{r}) = m^2$.

$\tilde{v}$: A set of n complex parameters describing the VNA, e.g., the well known 8-term model or the 12-term model of a 2-port VNA, which both assume linearity of the VNA. It is $\tilde{v} \in \mathbb{C}^n$ or $\dim(\tilde{v}) = n$.

$\tilde{s}$: The m^2 S-parameters of the standard or DUT. As for $\tilde{r}$ it is $\tilde{s} \in \mathbb{C}^{m^2}$ and $\dim(\tilde{s}) = m^2$.

These sets of variables are similar to vectors and at this point they can be actually seen as vectors. However, in the following their definition will be enhanced in a way, which makes clear that they have properties which are not vector-like.
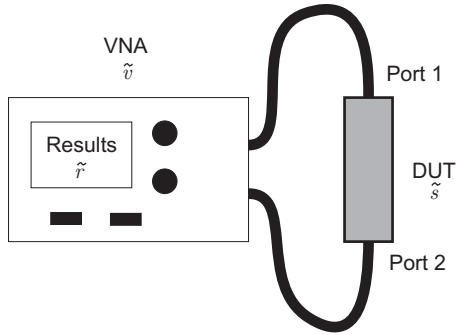
Figure 4.3: 2-Port measurement setup consisting of DUT, VNA, and measurement results. The measurement process involves three sets of true parameters:
$\tilde{r}$ True raw S-parameters (4 for a 2-port calibration)
$\tilde{v}$ True parameters of the VNA error model (typically 7...15 for a 2-port calibration)
$\tilde{s}$ True S-parameters of the DUT (4 for a 2-port DUT)

A particular measurement set-up is depicted in Fig. 4.3 and can be described by

$$\tilde{r} = g(\tilde{v}, \tilde{s}), \tag{4.1}$$

where $\tilde{r}$, $\tilde{v}$ and $\tilde{s}$ are the true values for one particular measurement. The system function $g()$ of the measurement process reflects the S-parameter model of the VNA. It is effectively a set of m^2 different complex valued functions of the common $n + m^2$ variables $\tilde{v}$ and $\tilde{s}$. Note that $g()$ takes only the true parameters (with tilde) as arguments.

True parameters (with tilde) designate the results of a virtually perfect computational process executed for each single measurement. This process includes the definition of ports and the perfect solution of Maxwell's equations for the whole setup consisting of VNA and DUT.

One can neither determine nor observe the absolutely true $\tilde{r}$, $\tilde{v}$ and $\tilde{s}$ due to finite accuracy and precision in mechanical and electrical measurements. These variables change from measurement to measurement.

For this reason, the whole measurement process is considered a statistical process. One introduces the variables $r \in \mathbb{C}^{m^2}$, $v \in \mathbb{C}^n$ and $s \in \mathbb{C}^{m^2}$ which are defined to be invariant during several subsequent measurements. The relation between the stable quantities r, v and s and the true values

$\tilde{r}$, $\tilde{v}$ and $\tilde{s}$ is given by

$$\tilde{r} = r, \tag{4.2}$$

$$\tilde{v} = v + \beta, \tag{4.3}$$

$$\tilde{s} = s + \varsigma. \tag{4.4}$$

Thereby the (most likely small) uncertainty variables $\beta \in \mathbb{C}^n$ and $\varsigma \in \mathbb{C}^{m^2}$ represent the following shortcomings of VNA calibration:

Instrumentation errors β

Temperature drift, cable movement, mechanical shock, nonlinearities, quantization errors of the analog-to-digital converter, noise etc. result in differences β between the VNA parameters v, which are defined to be invariant, and the true parameters $\tilde{v}$.

Errors in standards ς

Limited connector repeatability, dimensional uncertainties, inexact conductivity, uncertainties in the computation of standards etc. result in differences ς between the calculated value of the standard s and its true value $\tilde{s}$.

Scale reading errors

Typically more than 8 digits of the raw S-parameters r can be read from the VNA. DUTs and VNA setups with the best available repeatability show measured raw S-parameters r which are only stable up to the fourth digit. This is the reason why scale reading errors are considered negligible. Consequently there is no uncertainty variable in (4.2).

The graphical representation in Fig. 4.4 shows how the uncertainty variables influence the measurement.

In its initial state a VNA is not calibrated. In other words, the VNA parameters v are unknown.

One can calibrate a VNA by measuring standards. They are essentially DUTs with known S-parameters s. The measurements of the standards produce raw S-parameters r. The raw S-parameters r and the S-parameters s of the standards are the input to the calibration algorithm. As output the calibration algorithm determines an estimate $\bar{v}$ of the VNA parameters.

Once the VNA parameters v are estimated a partially inverted form of (4.1) can be used to determine the S-parameters of any given DUT

$$\tilde{s} = G(\tilde{r}, \tilde{v}). \tag{4.5}$$
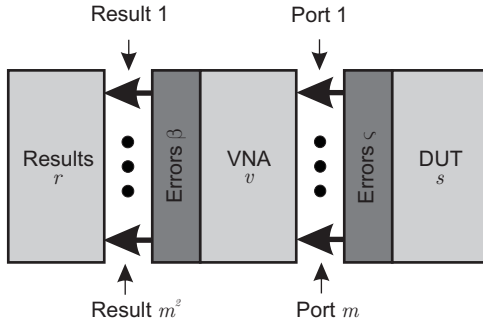
Figure 4.4: The measurement model for over-determined calibration includes errors in the calibration standards and in the VNA.

The variables $\tilde{s}$, $\tilde{r}$ and $\tilde{v}$ in (4.5) have to be replaced by s, r and v because the true parameters are not known. Now (4.5) results in s and thus the S-parameters of the DUT can be computed from r and v.

4.4.2 The system of equations used for calibration

Since $\dim(v)$ (number of VNA parameters to be determined by the calibration) is larger than $\dim(r)$ (number of raw values obtained by a single measurement) it is clear that several standards are needed to find all VNA parameters. If one uses more standards than required, the calibration is called over-determined. The advantage of an over-determined calibration is that it accounts for the aforementioned uncertainties.

Measuring an appropriate set of l standards yields raw S-parameters r for each standard. Substituting (4.2...4.4) into (4.1) results in a system of $\dim(r) = m^2$ equations for each measurement. These l systems of equations for individual measurements can be combined to form one larger system of equations which is referred to as function g'. To write the function g' properly, one must distinguish between the variables of all l measurements. For compact notation the primed variables r', s' and β', ς' are introduced, where r' is a short notation for all raw values of l standards and s' is a short notation for all S-parameters of l standards. Therefore, $\dim(r') = \dim(s') = lm^2$. Consequently the uncertainty variables are built the same way, thus β' and ς' are short notations of the uncertainty variables of all l measurements. Therefore, $\dim(\varsigma') = lm^2$ and $\dim(\beta') = $

ln.

This notation and (4.1)-(4.4) are used to describe the measurement of several standards

$$r' = g'(v, s', \beta', \varsigma').\qquad(4.6)$$

Due to the non linear nature of the function g' it is difficult to solve (4.6) directly for the VNA parameters v. Moreover, the structure of the function can vary significantly when different sets of standards are used. In fact, while the raw values r' are easily obtained by merely reading the display of the VNA, the S-parameters of the standards s' can be computed by solving Maxwell's equations for the geometry and material parameters of the standard. However, these computations are of finite precision.

For certain calibration methods, it is common practice to leave some unknown parameters in s' and to find them later as part of the result of the calibration. In such cases one can write the S-parameters s' as

$$s' = s'_d + S(s'_u).\qquad(4.7)$$

Thereby s'_d denotes the known S-parameters of the standards while s'_u stands for some (complex) quantities yet to be determined, e.g., a propagation constant of a line. The function $S()$ converts the parameters s'_u to S-parameters of the standards. Note that $s'_d \in \mathbb{C}^{lm^2}$ and $s'_u \in \mathbb{C}^q$ where q depends on the type and number of the partly described standards.

Based on the above it can be stated that calibration is a procedure which determines v or s'_u out of the raw values r' which are read from the VNA display and the known S-parameters s'_d of the standards. Thereby the uncertainties β' and ς' are treated according to their statistical behavior.

4.4.3 Statistical description of measuring standards

Consider a given VNA with given standards as a starting point. The standards s' and the complex parameters v describing the VNA are set to fixed values, whereas the uncertainties β' and ς' are random variables. The function g' results in the raw S-parameters r' in dependence of v, β', s' and ς'. The set $U_{v,s'}$ contains all tuples (β', ς') which are allowed by the models of the standards and the VNA. Therefore, $(\beta', \varsigma') \in U_{v,s'}$. The conditional pdf[1] $p(\beta', \varsigma'|s', v)$ assigns a probability density to each point in

---

[1]The notation $p(\beta', \varsigma'|s', v)$ is shorter than the standard notation for pdfs. It is used because the distinction between random variables and integration variables is not
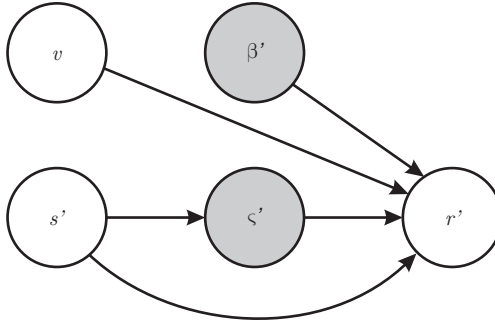
Figure 4.5: Bayesian Network from which the pdf $p(\beta', \varsigma'|s')$ is derived. White variables are observable whereas gray variables are not observable. The arrow direction indicates the causality in the interaction between variables.

$U_{v,s'}$. This pdf of β', ς' under the condition of s', v is nonnegative and its integral on $U_{v,s'}$ equals one. Note that dependence of $p(\beta', \varsigma'|s', v)$ on s', v makes it possible to account for nonlinearities of the VNA. The Bayesian network shown in Fig. 4.5 describes the probabilistic dependencies (and independencies) of the variables involved. Although the structure of the Bayesian network does not account for nonlinearities of the VNA, one could easily include these by adding arrows from v, s' and ς' to β'. In the following a linear VNA is assumed although one could easily extend the presented algorithm to nonlinear VNAs. A practical reason for this restriction is that it is quite challenging to define $p(\beta', \varsigma'|s', v)$ for a nonlinear VNA. In the linear case, β' and ς' do not depend on v. Thus the pdf $p(\beta', \varsigma'|s')$ is used instead of $p(\beta', \varsigma'|s', v)$.

The pdf $p(\beta', \varsigma'|s')$ reflects uncertainties in the standards as well as uncertainties in the VNA. Those two groups of parameters are treated in a slightly different way. The VNA parameters $\tilde{v} = v + \beta$ are assumed to be unconstrained and there are no reliable a priori known values for v. The only assumption is that $\tilde{v}$ is fairly stable and varies from measurement to measurement with a standard deviation which does not depend on the yet unknown value v. On the other hand, the parameters $\tilde{s}' = s' + \varsigma'$ often have known expectation. Moreover, restrictions due to passivity

---

necessary in the context of this thesis. An example for the standard notation would be a pdf $p_A(a)$ where A is the random variable and a the integration variable.

and reciprocity of the standards affect $U_{v,s'}$. The resulting dependence of ς' on s' is reflected by the direct arrow from s' to ς' in the Bayesian network (Fig. 4.5) as well as in the notation $p(\ldots|s')$.

Since many physical factors affect the VNA parameters v it is reasonable to assume a multivariate Gaussian distribution for β' (central limit theorem [41]). The mean values of β' are set to zero in order to obtain unbiased results. The choice of the respective covariance matrix is based on a physical analysis of the calibration setup as well as on experience. A procedure for defining the covariance matrix of the VNA is described in section 4.8.1.

Typical metrology models of calibration standards depend on more than 20 geometry and material parameters. The large number of different contributions to the uncertainties of the standards ς' leads to a nearly multivariate Gaussian distribution for each component of ς'. However, for passive standards the components of $\tilde{s} = s' + \varsigma'$ must satisfy the classical restrictions of passive reciprocal systems, [42], [43] and [44]. This implies that the absolute value of the respective components in $s' + \varsigma'$ must not exceed one. As a consequence the set $U_{v,s'}$ is restricted to tuples (β', ς') where passivity of the standards is guaranteed. This can lead to a truncated multivariate Gaussian distribution as shown in Fig. 4.6. The first step to define the ς' dependence of $p(\beta', \varsigma'|s')$ is to compute the S-parameters of the standard from a physical model. The same model is also used in a Monte-Carlo simulation to compute the pdf of the physical model. As a second step, one assumes a multivariate Gaussian distribution $p^0(\beta', \varsigma'|s')$ for the S-parameters of the standard. Next, $p^0(\beta', \varsigma'|s')$ is truncated. Then the covariance matrix and the mean values of the original pdf $p^0(\beta', \varsigma'|s')$ are adjusted in such a way that the truncated distribution matches the distribution of the physical model. Finally, the truncated pdf is multiplied with a constant to set its integral on $U_{v,s'}$ to one.

Since usual standard deviations of precision metrology components are fairly small it is possible to omit the truncation for those components of ς' which are associated to s'-components with absolute values significantly smaller than one.

The versatility of the statistical model can be demonstrated with a typical measurement setup where one port is connected to the VNA via a semi-rigid cable (high stability of cable S-parameters) and the other port is connected to the VNA by a flexible cable (low stability of cable S-parameters). In this case one can attribute a high uncertainty to
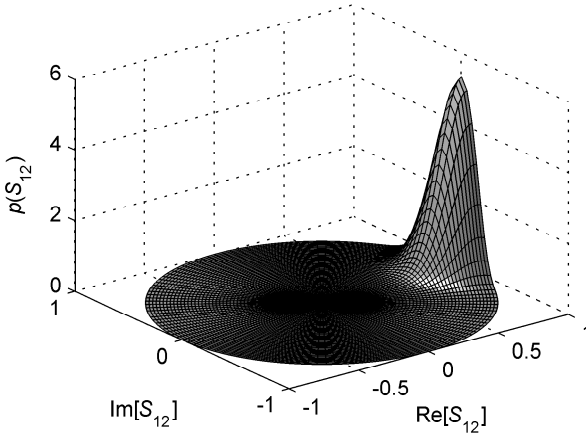
Figure 4.6: The not truncated 2D Gaussian pdf with mean value $\mu = 1 + j0$ and standard deviation $\sigma = 0.15$ is truncated at the unit circle to yield the pdf of S_{12} of the thru. For the sake of visibility, σ is here much larger than in practical applications. Note that the pdf $p(\beta', \varsigma'|s')$ is a function of the uncertainties only and not a function of the S-parameters (s') as it is plotted in this picture.

those components of v which are associated with the flexible cable and a lower uncertainty to components associated with the semi-rigid cable. The measurement model not only takes into account unequal uncertainties for both cables of the VNA, but as there are separate components in β' for each measurement, one can attribute higher uncertainties to measurements, which are subject to more cable movement due to standards being much longer or shorter than the DUT.

4.5 Theoretical solution of the calibration problem

As described in the previous sections, VNA measurement and calibration is understood as a statistical process. The underlying physics of this process is formally characterized by the pdf $p(\beta', \varsigma'|s')$ and the function g' given in (4.6). Based on these two characteristics one can develop the new pdf $p(v, s_u'|r', s_d')$ for VNA parameters v or s_u' under the condition of

given r', s'_d. This pdf finally dictates the mean value of v and/or s'_u, i.e., the solution of the calibration problem.

A first substantial step towards the solution is to compute $p(r'|v, s'_u, s'_d)$. The pdf to observe r' under the condition of given v and s' is obtained by integrating $p(\beta', \varsigma'|s')$ over the subset $\mathbb{A}$ of $U_{v,s'}$.

$$\mathbb{A} = \{(\beta', \varsigma') : g'(v, s'_d, s'_u, \beta', \varsigma') = r'\} \tag{4.8}$$

$$p(r'|vs'_u, s'_d) = \int_{\mathbb{A}} p(\beta', \varsigma'|s') \, d\mathbb{A} \tag{4.9}$$

The subset $\mathbb{A}$ is defined as all pairs (β', ς') which fulfill g' for one fixed r', v, s'. In other words, $\mathbb{A}$ contains all tuples (β', ς') which can explain the observed raw S-parameters r' if a VNA v with standards s' is used. The dimension of $\mathbb{A}$ equals the number of variables in β' which is lower than the dimension of $U_{v,s'}$. The already-mentioned integral can be extended to compute the pdf $p(r'|s'_d)$ of reading raw S-parameters r' on a VNA measuring the standards s'_d by

$$p(r'|s'_d) = \int_{\mathbb{C}^n} \int_{\mathbb{C}^q} p(r'|v, s'_u, s'_d) \, p(v, s'_u) \, dv \, ds'_u$$

$$= \int_{\mathbb{C}^n} \int_{\mathbb{C}^q} \int_{\mathbb{A}} p(\beta', \varsigma'|s') \, d\mathbb{A} \, p(v, s'_u) \, dv \, ds'_u. \tag{4.10}$$

As already mentioned after (4.7), q denotes the number of unknown parameters in the standards, i.e., $q = \dim(s'_u)$. Note that the exact knowledge of the pdf $p(v, s'_u)$ is not very critical because one wants to determine v, s'_u by calibration and not by prior knowledge. Depending on what is known about v and s'_u, a rather wide, e.g., a uniform distribution can be chosen, which then makes the infinite range of integration $\mathbb{C}^{n+q}$ to become finite. Now, the conditional pdf of observing v and s'_u under the condition r' is given by Bayes law as

$$p(v, s'_u|r', s'_d) = \frac{p(r'|v, s'_u, s'_d) \, p(v, s'_u)}{p(r'|s'_d)}. \tag{4.11}$$

The process of finding the values v and s'_u from the pdf given in eq. (4.11) is called estimation and is denoted by the estimator

$$E(r', s'_d) = (\bar{v}, \bar{s}'_u). \tag{4.12}$$

Thereby $\bar{v}$ and $\bar{s}'_u$ are estimates of the VNA parameters v and of the parameters s'_u of the standards respectively.

Criteria like unbiasedness and minimum variance can be applied to rate an estimator, see [45]. As shown in Appendix D, a minimum variance unbiased estimator for the calibration problem is

$$E(r', s'_d) = \int\limits_{\mathbb{C}^{n+q}} (v, s'_u)\, p(v, s'_u | r', s'_d)\, dv\, ds'_u. \tag{4.13}$$

Substituting (4.9), (4.10) and (4.11) into (4.13) yields

$$E(r', s'_d) = \frac{\int\limits_{\mathbb{C}^{n+q}} (v, s'_u) \int\limits_{\mathbb{A}} p(\beta', \varsigma' | s')\, d\mathbb{A}\, p(v, s'_u)\, dv\, ds'_u}{\int\limits_{\mathbb{C}^{n+q}} \int\limits_{\mathbb{A}} p(\beta', \varsigma' | s')\, d\mathbb{A}\, p(v, s'_u)\, dv\, ds'_u}. \tag{4.14}$$

In the case of l standards, n complex VNA model parameters and q complex standard parameters the outer integrals in (4.14) show $n+q$ complex dimensions. The integrands differ only by the factor (v, s'_u) but consist of a further integral with ln complex dimensions. Note that the inner range of integration $\mathbb{A}$ depends on the outer integration variables v and s'_u. Numerically, the evaluation of numerator and denominator are performed simultaneously.

For instance, a LRL calibration with four lines and one reflect standard ($l = 5$) with unknown reflection coefficient and propagation constant ($q = 2$) using an 8-term VNA model ($n = 7$) requires the evaluation of a complex $ln + n + q = 44$-dimensional integral. This can be a very tedious task mainly due to the complicated shape of $\mathbb{A}$ but also because the integrand takes appreciable values only in a very small region. In such cases appropriate numerical integration techniques first search the global maximum of the integrand and then use some approximations on the integrand to obtain the final result. Further details on how to compute points in $\mathbb{A}$ and appropriate numerical integration techniques are given in section 4.6.2.

4.6 Computation of the estimator

The evaluation of the estimator (4.14) is not straight forward. Hurdles include the very narrow pdf $p(\beta', \varsigma' | s')$ and the shape of the inner integration range $\mathbb{A}$ which varies with v and s'_u. The following describes how
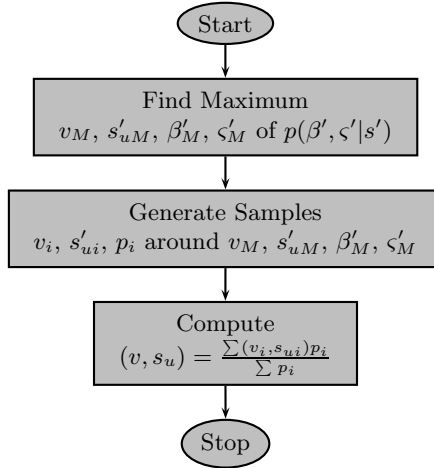
Figure 4.7: Flowchart for the computation of the estimator. The first step of the algorithm is to find the solution of the calibration problem which is the most probable. The following step is to generate the samples for the Monte-Carlo integration which is executed in the last step.

these obstacles are overcome. First, a combination of optimization techniques is used to find the maximum of the inner integrand. Subsequently, the integrals are computed with Monte-Carlo integration. The flowchart of the complete algorithm is given in Fig. 4.7.

4.6.1 Finding the solution with maximum probability

The first step in the flowchart in Fig. 4.7 is finding the maximum of $p(\beta', \varsigma'|s')$. The crucial points are that this maximum must be found on $\mathbb{A}$ only and that the shape of $\mathbb{A}$ varies with v and s'. In a more formal way, one can describe the desired maximum by

$$\max_{v, s'_u, \beta', \varsigma'} \left[p(\beta', \varsigma'|s') : g'(v, s'_u, s'_d, \beta', \varsigma') = r' \right]. \tag{4.15}$$

From (4.15) it is obvious that for a given r' and s'_d one must find not only some dedicated values β'_M and ς'_M being associated with the desired maximum of $p(\beta', \varsigma'|s')$, but also the values v_M and s'_{uM}. There is no

need to search in the full space spanned by $v, s'_u, \beta', \varsigma'$ but only in the subset v, s'_u, β'. The reason for this is the function g'. All variables in ς' can be directly computed from any given v, s'_u, β' by (4.5).

Due to the non linear character of the underlying equations and the constraints of the components of ς' (passive standards) it is still difficult to find this maximum. In general, it can be stated that the high dimensional and non linear optimization problem has several local maxima, i.e., it is not convex. This means that local optimizers which can reliably solve only convex problems may not be suitable [46]. However, if the objective function — pdf $p(\beta', \varsigma'|s')$ — was continuously differentiable, a local optimizer fed with a good starting point would work fine [38]. Here, the quadratic local optimizer `lsqnonlin`[2] from the Matlab$^{\text{TM}}$ optimization toolbox is used. A good starting point can be obtained by performing a calibration which is not over-determined, see [34] for details. However, here the objective function is not continuous due to the passivity constraints on $\tilde{s}' = s' + \varsigma'$. The resulting constraints on ς' which truncate the underlying multivariate Gaussian pdf $p^0(\beta', \varsigma'|s')$ can be treated by the barrier algorithm [47]. The essential idea here is to "continuously truncate" $p^0(\beta', \varsigma'|s')$.

Let $\tilde{s}_i = s_i + \varsigma_i$ be the i-th parameter in the list $\tilde{s}'$. If $|\tilde{s}_i| \leq 1$ holds, then the difference $\delta_i = (1 - |s_i + \varsigma_i|) - |1 - |s_i + \varsigma_i||$ is zero and the modified objective function

$$f(\sigma_c, \beta', \varsigma') = p^0(\beta', \varsigma'|s') \cdot e^{-\frac{\delta_i^2}{2\sigma_c^2}} \tag{4.16}$$

equals the original objective function. Wherever $|s_i + \varsigma_i| > 1$ holds the original objective function is pushed down. The parameter σ_c determines the slope beyond the border. For very small values of σ_c, the function $f(\sigma_c, \beta', \varsigma')$ approaches a (not yet normalized) pdf which is truncated by the restriction $|\tilde{s}_i| \leq 1$. More restrictions of the same kind are taken into account by defining the vector $\mathbf{d}(s', \varsigma') = (\delta_1, \delta_2, \ldots)$ and using the square of its Euclidian norm $\|\mathbf{d}\|^2$ in the exponent in (4.16).

Since a local optimizer works more efficiently for smoother objective functions and better starting points the barrier algorithm iteratively decreases the value of σ_c. Starting with the very moderate value $\sigma_c = 1$ one defines $\sigma_c(\mu) = 10^{-\mu}$ and lets μ run from zero to 10 in integer steps.

---

[2]Matlab Version 7.0.4.365 SP2

Unfortunately for noisy data sets a good starting point is not always available. Therefore another measure to overcome such difficulties is proposed. It consists of constraining the VNA parameters v and β' to physically plausible values. These are values which allow to invert the model of the VNA with good numerical accuracy.

The VNA parameters v and β' describe the relation between the DUT S-parameters and the raw VNA results (Fig. 4.4). Describing this relationship by a transmission matrix $\mathbf{T}(v, \beta')$ it follows that the matrix $\mathbf{T}$ must be invertible. If $\mathbf{T}$ is not invertible the VNA is broken. The reciprocal condition number $\kappa(\mathbf{T})$ should not be smaller than $\chi = 0.0001$ because for a VNA which is calibrated with high impedance $(10\,\mathrm{k}\Omega)$ standards one typically obtains $\kappa(\mathbf{T}) = 0.001$. The factor

$$k(\mathbf{T}, \sigma_\kappa) = e^{-\frac{(\kappa(\mathbf{T}) - \chi - |\kappa(\mathbf{T}) - \chi|)^2}{2\sigma_\kappa^2}} \tag{4.17}$$

acts as an additional barrier which prevents the local optimizer from converging towards "solutions" with low physical plausibility. The factor σ_κ is experimentally set to $\sigma_\kappa = 10^{-5}$.

Combining this idea with the barrier algorithm yields the objective function

$$f(\mathbf{T}, \mu, \beta', s'_u) = p^0(\beta', \varsigma'|s') \cdot e^{-\frac{\|\mathbf{d}\|^2}{2 \cdot 10^{-2\mu}}} \cdot k(\mathbf{T}, \sigma_\kappa) \tag{4.18}$$

The list of the input variables for the objective function contains only the variables which vary independently during the search. The complete algorithm for the search of the maximum of $p(\beta', \varsigma'|s')$ is shown in Fig. 4.8.

Note that this maximum is related to a certain location v_M, s'_{uM}, β'_M in the search space and there is an associated value ς'_M. Other values for (v, s'_u) are also possible but have a lower probability density. Due to the truncations in $p(\beta', \varsigma'|s')$ the values (v_M, s'_{uM}) represent not necessarily the best solution of the calibration problem but only the most probable one. More appropriate is the expectation of (v, s'_u) which results from (4.14). The computation of the high dimensional integrals in (4.14) requires a Monte-Carlo integration, which is discussed in the next subsection.

4.6.2 Monte-Carlo integration

A typical VNA problem results in an integral with 44 complex dimensions. A rectangular grid with N points in each dimension ends up in N^{88} real
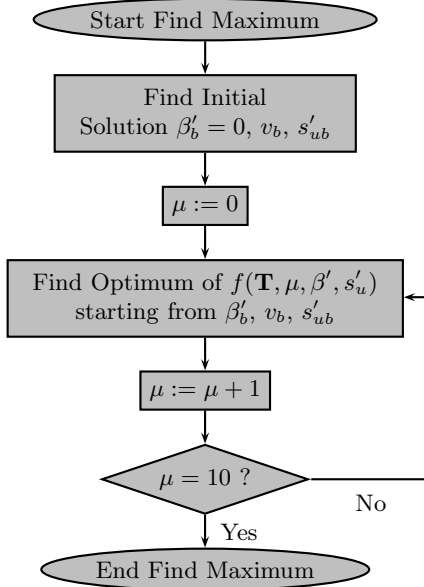
Figure 4.8: A detailed representation of the first step in Fig. 4.7. The first step of the algorithm for finding the maximum (4.15) consists of finding an initial solution v_b, s'_{ub} as specified in [34]. The uncertainty variables β' can be guessed initially as zero $\beta'_b = 0$ for this initial solution. The following steps describe the barrier algorithm for the approximation of $p(\beta', \varsigma'|s')$.

values — obviously far beyond any brute force integration technique. A practical way out is a Monte-Carlo integration.

Considering the right side of (4.14) it follows that the integrals in the numerator and denominator contain the pdfs $p(\beta', \varsigma'|s')$ and $p(v, s'_u)$. The numerator contains additionally the factor (v, s'_u). Note that the (v, s'_u)-dependency of the full integrand holds through $\mathbb{A}$'s dependency on those variables. The factor $p(v, s'_u)$ is constant and needs no further discussion because it cancels out. The multiple integrals over $\mathbb{C}^{n+q}$ and $\mathbb{A}$ can be approximated by a sum. Let p_i be a short notation for $p(\beta'_i, \varsigma'_i|s')$ at the

location $v_i, s'_{ui}, \beta'_i, \varsigma'_i$. Then the expression

$$E_N(r', s'_d) = \frac{\sum_{i=1}^N (v_i, s'_{ui})p_i}{\sum_{i=1}^N p_i} \qquad (4.19)$$

is an approximation of $E(r', s'_d)$ in (4.14) if the locations of p_i are chosen appropriately. In this context an appropriate choice means that the integration range is covered with uniformly distributed locations $v_i, s'_{ui}, \beta'_i, \varsigma'_i$. Several things have to be considered to find such a set of locations:

1) In principle, the integration range is unbounded with respect to v, β' and partially bounded with respect to s'_u, ς' (passivity restrictions). A practical and quite restrictive bound is given through $p(\beta', \varsigma'|s')$ which has significant magnitude only for small values of β', ς'. The respective range is predefined by the variances of those variables.

2) The variances of ς' can be significantly larger than the variances of β'.

3) The domain $\mathbb{A}$ — its dimension equals the dimension of β' — depends on the fix raw VNA values r' and the variables v, s'_u. It is defined by g' and changes when v, s'_u vary.

4) Given any ς' which is probable according to $p(\beta', \varsigma'|s')$ the function g' usually delivers β'-values far out of the range defined in 2).

5) The function g' responds to non-Gaussian distributed input parameters with Gaussian distributed output parameters due to the central limit theorem[41].

In spite of these difficulties, the algorithm (Fig. 4.9) finds a set of locations $v_i, s'_{ui}, \beta'_i, \varsigma'_i$ suitable for a Monte-Carlo integration using the simple sum (4.19). The most important point is that all locations are expected to be within close vicinity of the already known location $L_M = (v_M, s'_{uM}, \beta'_M, \varsigma'_M)$ associated to the global maximum of $p(\beta', \varsigma'|s')$. Since this domain must be searched for, the algorithm starts with some random locations close to L_M and controls the allowed distance from L_M by the restriction parameter a. With each iteration the restriction parameter is doubled or halved depending on the actual and previous values of the pdf $p(\beta', \varsigma'|s')$ and the value of the mode variable. If the mode variable is set
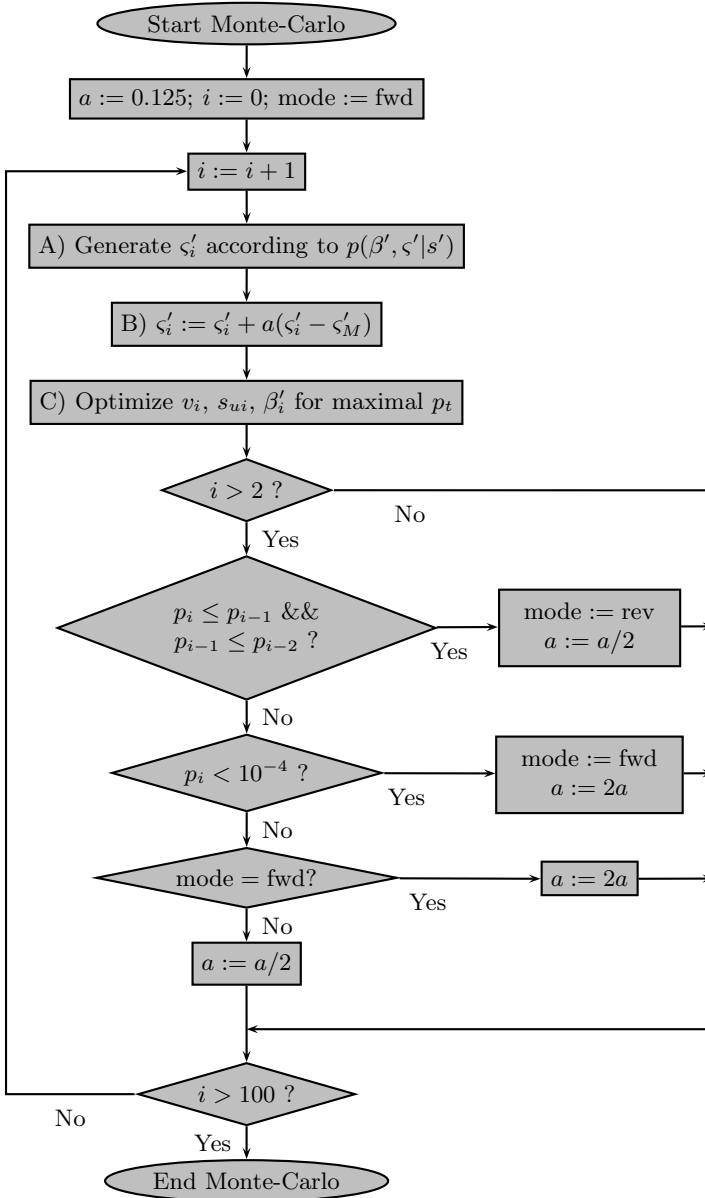
Figure 4.9: A detailed description of the second step in Fig. 4.7. The algorithm produces samples ς_i' around ς_M' with varying restriction a. Note that a can take values larger than 1. The ς_i' are combined with v_i, s_{ui}', β_i' which satisfy function g' and yield maximum probability density p_i.

to fwd, the next location will be closer to L_M. For the rev state the next location will be further away from L_M.

The core procedure of the random choice starts with a random set ς_i and then finds suitable values v_i, s'_{ui}, β'_i. The procedure is performed in three steps:

A) *Random choice of* ς'_i

The sample ς'_i is chosen according to the truncated pdf $p(\beta', \varsigma'|s')$. The truncation is easily taken into account by rejection sampling, [48]. Starting with ς_i prevents problems due to 5) and all restrictions due to 1) are taken into account with this step.

B) *Move* ς'_i *toward* ς'_M

According to the actual restriction parameter a the sample is moved as $\varsigma'_i \rightarrow \varsigma'_i - a(\varsigma'_i - \varsigma'_M)$. This step (partly) avoids cases described in 5).

C) *Find suitable* v_i, s'_{ui}, β'_i

Since the dimension of β' is higher than that of ς' only part of the values β'_i can be obtained from ς_i. Function g' gives the respective relation. The remaining values in β_i as well as v_i, s'_{ui} are obtained by a constrained optimization process such that maximum p_i results. The optimization uses again the local optimizer `lsqnonlin` from Matlab and is similar to the process in the previous section. Differences include the starting value — here a random ς'_i is used while the rest stems from L_M — and the used constraints. While the complex constraints for finding L_M are implemented with the barrier algorithm, the constraint mechanism included in `lsqnonlin` is used for the rather simple constraints which apply to s_u and ς'.

The samples v_i, s'_{ui}, produced with this algorithm, are equal up to the n-th digit where $n = 2 \ldots 6$ in the examples given in the next section. The estimation (4.19) yields $n + 1$ stable digits after $N = 100$ samples. The Monte-Carlo algorithm uses only $N = 100$ samples because of its $1/\sqrt{N}$ convergence. Further gains in accuracy would be very expensive in terms of computation time. The sequence of locations does not exactly show uniform distribution in the integration range. Nonetheless the practical tests described in the next sections indicate that the estimation error due to non-uniformly distributed locations must be small.

4.7 Test with synthetic data set

In order to make a statement about the quality of a calibration algorithm, two things are required. First, one must quantify how well the calibration algorithm works and second the algorithm must be compared against the performance of other algorithms. A LRL calibration is used for this comparison. All information which is usually collected during a real LRL calibration is artificially generated and then stored in a synthetic data set which contains blocks of 1000 calibrations. Each of them is characterized by three criteria: the variance of the standards, the frequency and the impedance level (either a $50\,\Omega$ calibration or a $10\,k\Omega$ calibration). Such parameterized data blocks are calibrated with four different calibration algorithms: Plain LRL, Multical Clone, Statistical Clone and Monte-Carlo. The results of each calibration are statistically varying $\bar{v}$ values. They are compared against the reference value v which was used to generate the synthetic data set. The mean squared differences are used to classify the different algorithms.

4.7.1 Setting up the synthetic data set

The LRL calibration is chosen as an example because it is regarded as the most accurate calibration in many cases. The synthetic data set of the LRL calibration contains information about the standards and the raw measurement results r'. The standards are four lines ($0\,mm$, $42\,mm$, $49\,mm$ and $125\,mm$) and two shorts. The line lengths are designed for a frequency range of $f = 0.2\ldots18\,GHz$. Further definitions of the standards are:

- Lines are not reflective.

- Lines are lossless.

- All lines have the same phase constant.

- Shorts do not allow for transmission.

- Both shorts have the same reflection coefficient.

Utilizing this information the calibration algorithm will estimate v from the measured raw data r'.

For generating each r, a whole chain of computations must be performed. First, one defines the ideal S-parameters s, then they are perturbed to obtain $s + \varsigma$. Next, one defines v and adds a perturbation to achieve $v + \beta$. Finally, r can be computed with the perturbed standard S-parameters $s + \varsigma$ and the perturbed error terms $v + \beta$.

The start of the chain of computations is to compute the ideal S-parameters of the lossless perfectly matched lines and to set the ideal S-parameter of the short to $\Gamma = -1$. Then a set of complex Gaussian random variables with zero mean value and variance $\sigma_{\varsigma'}^2$ is generated to account for ς'. These random variables are added to the ideal S-parameters. Whenever the absolute value of a resulting S-parameter is larger than one, a new random number is generated for the respective S-parameter. This process, called rejection sampling, is repeated until all amplitudes of S-parameters are less than one. For an example see S_{12} in Fig. 4.6. The resulting S-parameters represent $s + \varsigma$. This procedure does not ensure strict passivity of the standards but it is very simple and yields distributions which are similar to S-parameter distributions with strict passivity, [42]. A direct consequence of the given procedure is that the reflection coefficients of the shorts and the transmission coefficients of the lines follow a non-Gaussian distribution.

The next step is to define and perturb the measurement function parameters v. Two different definitions of v will be used to show the influence of $50\,\Omega$ standards and $10\,\mathrm{k\Omega}$ standards on the calibration accuracy. To obtain $v + \beta$, a complex random variable β which is Gaussian in all components with zero mean value and variance $\sigma_{\beta'}^2$ is added to the ideal error box parameters v. These error box parameters are called perturbed error box parameters.

Finally, the measurement results r' are computed. For generating r, the variance of the error box parameters is set to $\sigma_{\beta'}^2 = 5 \times 10^{-7}$ and the variance of the standards is set to $\sigma_{\varsigma'}^2 = [10^{-3}, 10^{-5}, 10^{-7}]$. Further parameters for generating the raw S-parameters r' include the frequency $f = [3.45, 9.15]\,\mathrm{GHz}$ and the choice between $50\,\Omega$ and $10\,\mathrm{k\Omega}$ standards. For the $50\,\Omega$ case, the magnitudes of the transmission coefficients are set to approximately 1 and the source match and directivity terms are set to magnitudes of approximately 0.1, see Fig. 4.10. For the $10\,\mathrm{k\Omega}$ case, the directivity and source match terms are set to magnitudes of 0.99 and the transmission terms to 0.1. Thousand calibrations are generated for each
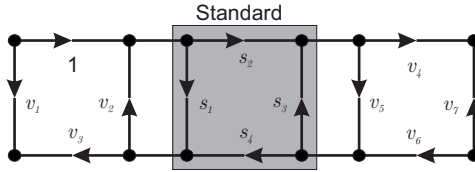
Figure 4.10: 8-Term error network representing the VNA and a standard. The
error boxes are constructed from transmission terms v_3, v_4, v_6, directivity
terms v_1, v_7 and source match terms v_2, v_5. One branch of the network
describing the VNA is set to 1 without loss of generality because S-parameters
are ratios of wave quantities. The S-parameters of the standard are called
s_n.

setting, resulting in a total of 2 impedances $\times$ 2 frequencies $\times$ 3 variances $\times$
1000 calibrations = 12,000 calibrations.

This data set contains calibration scenarios where the accuracy of the
standards is better than the precision of the VNA but also cases where the
opposite is true. With this variety it can be assessed how well errors in the
VNA and errors in the standards are modeled. The data set contains sce-
narios with $50\,\Omega$ and $10\,\text{k}\Omega$ standards. The $10\,\text{k}\Omega$ case produces strongly
non-Gaussian distributed measured raw S-parameters, whereas the $50\,\Omega$
case produces nearly Gaussian distributed measured raw S-parameters.
These parts of the data set are intended to test the dependence of the cal-
ibration results on the shape of the pdf of the measured raw S-parameters.
The last parameter to be discussed is the frequency. The expected level
of error for the $f = 9.15\,\text{GHz}$ calibration is lower than for $f = 3.45\,\text{GHz}$
due to the resulting phase difference of the lines, see [49]. However, this
is only valid for the $50\,\Omega$ calibration because [49] assumes small source
match terms to arrive at this result.

Now the raw S-parameters r', the pdf $p(\beta', \varsigma'|s')$ and information about
the standards are available. With this one obtains estimates of the cali-
bration coefficients v and the standard parameters s'_u (phase constant and
reflection coefficient).

4.7.2 Calibration algorithms and results

In the following the algorithms Plain LRL, Multical Clone and Statistical
Clone are used to benchmark the Monte-Carlo algorithm because they are

probably the most popular calibration algorithms for the LRL problem. The Plain LRL is a very basic algorithm which is described in [34]. This algorithm does not use any pdf but assumes the VNA and the standards to be flawless.

The Multical Clone algorithm is based on [12] and [13]. It assumes Gaussian distributed errors in the standards but no errors in the VNA. The variances of the errors in the standards do not have to be supplied to the algorithm. They are set to a fixed value by the algorithm.

The Statistical Clone algorithm is based on the equations in [38]. This algorithm assumes errors in the standards and in the scale reading. For calibration, the covariance matrix of the errors in the standards and of the errors in the measured raw S-parameters are required. It is trivial to determine the covariance matrix for the standards because $p(\beta', \varsigma'|s')$ is known. The covariance matrix for the raw S-parameters r' is constructed from the raw S-parameters of a special synthetic data set with unperturbed standards but with perturbed VNA parameters.

All described calibration algorithms are used to estimate v. Tables 4.1 and 4.2 show the mean squared error of the estimate $\bar{v}$ with respect to the v which were used for the generation of the data set. Each entry in the tables represents a block of 1000 calibrations and is thus itself a realization of a random variable. The variances of these random variables are in the $10\,\mathrm{k\Omega}$ Plain LRL cases that large that no convergence for more accurate standards is visible. In the other cases, the variance of the results is much smaller. Comparing the mean squared errors for all algorithms and calibration scenarios shows that the Monte-Carlo algorithm always performs better than all other algorithms. The reason for this is that the Monte-Carlo algorithm assumes the errors to be in the standards and in the VNA itself. In contrast the Plain LRL algorithm does not assume any errors and the Multical Clone assumes errors only in the standards. The Statistical Clone algorithm assumes errors in the standards and in the measured raw S-parameters. This is sufficient for $50\,\Omega$ calibrations but for non-standard applications like the $10\,\mathrm{k\Omega}$ calibration the advantages of the new model of the calibration process become evident.

The very robust convergence is another advantage of the new algorithm. The No Convergence entries in the tables signify cases where the respective algorithm did not converge or produced unrealistic errors. While the Multical Clone algorithm produced huge errors in all of the $10\,\mathrm{k\Omega}$ cases, the Statistical Clone algorithm failed to converge in only one $10\,\mathrm{k\Omega}$ case.

Table 4.1: Mean squared error of $\bar{v}$ for the $50\,\Omega$ case

	$\sigma_{\varsigma'}^2 = 10^{-3}$	$\sigma_{\varsigma'}^2 = 10^{-5}$	$\sigma_{\varsigma'}^2 = 10^{-7}$
Plain LRL $f = 3.45\,\text{GHz}$	1.242×10^{-1}	9.642×10^{-4}	1.126×10^{-5}
Multical Clone $f = 3.45\,\text{GHz}$	9.818×10^{-4}	1.166×10^{-5}	1.623×10^{-6}
Statistical Clone $f = 3.45\,\text{GHz}$	9.842×10^{-4}	1.055×10^{-5}	1.302×10^{-6}
Monte-Carlo $f = 3.45\,\text{GHz}$	9.706×10^{-4}	1.008×10^{-5}	1.280×10^{-6}
Plain LRL $f = 9.15\,\text{GHz}$	9.483×10^{-2}	6.649×10^{-6}	9.934×10^{-7}
Multical Clone $f = 9.15\,\text{GHz}$	7.242×10^{-4}	8.693×10^{-6}	1.309×10^{-6}
Statistical Clone $f = 9.15\,\text{GHz}$	3.957×10^{-4}	4.196×10^{-6}	5.971×10^{-7}
Monte-Carlo $f = 9.15\,\text{GHz}$	3.734×10^{-4}	3.855×10^{-6}	5.847×10^{-7}

During a closer examination of this last case it was found that supplying the correct solution of the calibration problem as a starting point to the Statistical Clone did not solve the problem. For this case the Statistical Clone algorithm does not converge because its error model does not produce a local minimum.

It must be mentioned that robust convergence and better results require more computation time. For calibration the Matlab implementation of the Monte-Carlo algorithm needs half an hour to compute 1000 frequency points on a single core AMD Opteron 2.2 GHz with 3 GB RAM. The other in-house algorithms need less than five minutes for this task. Similar values are reported in [39].

Table 4.2: Mean Squared Error of $\bar{v}$ for the $10\,\mathrm{k\Omega}$ case

	$\sigma^2_{\varsigma'} = 10^{-3}$	$\sigma^2_{\varsigma'} = 10^{-5}$	$\sigma^2_{\varsigma'} = 10^{-7}$
Plain LRL $f = 3.45\,\mathrm{GHz}$	3.292×10^{-3}	6.497×10^{-3}	9.099×10^{-3}
Multical Clone $f = 3.45\,\mathrm{GHz}$	No Convergence	No Convergence	No Convergence
Statistical Clone $f = 3.45\,\mathrm{GHz}$	1.436×10^{-2}	4.591×10^{-3}	7.924×10^{-4}
Monte-Carlo $f = 3.45\,\mathrm{GHz}$	3.094×10^{-3}	1.824×10^{-4}	5.127×10^{-5}
Plain LRL $f = 9.15\,\mathrm{GHz}$	8.986×10^{-3}	7.131×10^{-3}	1.133×10^{-2}
Multical Clone $f = 9.15\,\mathrm{GHz}$	No Convergence	No Convergence	No Convergence
Statistical Clone $f = 9.15\,\mathrm{GHz}$	No Convergence	6.404×10^{-4}	1.755×10^{-4}
Monte-Carlo $f = 9.15\,\mathrm{GHz}$	1.778×10^{-3}	3.936×10^{-4}	2.904×10^{-5}

4.8 Tests with real data set

After testing the calibration algorithms with the synthetic data set they
are applied to a real LRL calibration problem. First, the associated real
data set is compiled. The required probability density functions have to be
constructed from uncertainty computations of the standards and estimates
of the VNA uncertainties. Then the different calibration algorithms are
applied to the real data set. The accuracy of the algorithms can not be
computed by the resulting estimates $\bar{v}$ because the true v is not known.
Here the only way to judge the quality of the different algorithms is to
compare how well the frequency response of a well known DUT meets the
expectations.

4.8.1 Real data set

As before, the properties of the standards are first defined. A $50\,\Omega$ N-type calibration kit with two phase matched offset shorts and four lines ($0\,\text{mm}$, $41.6632\,\text{mm}$, $48.6035\,\text{mm}$, $124.8755\,\text{mm}$) is used. The kit can be used for calibrations from $f = 0.2\ldots 18\,\text{GHz}$. Further information about the standards are:

- Lines are not reflective.

- Lines are lossy.

- All lines have the same phase constant.

- Shorts do not allow for transmission.

- Both shorts have the same reflection coefficient.

Note that losses in the lines are now considered.

Unlike for the synthetic data set the measured raw data r' is obtained from real measurements. This is the reason why one has to construct the probability density functions for the different calibration algorithms.

The Statistical Clone requires the covariances of the S-parameters, describing the standards, and of the measured raw S-parameters. The covariance matrix for the S-parameters of the standards can be computed from connector repeatability, dimensional uncertainties, conductivity uncertainties and uncertainties in the computational process yielding the S-parameters of the standard. The covariance matrix of the measured raw S-parameters is usually obtained by repeating the anticipated cable movements with attached standards. This method requires standards which are much more stable than the measurement system. The resulting variations in the raw S-parameters give the estimated variance of the raw S-parameters.

Other than the Statistical Clone algorithm, the Monte-Carlo algorithm requires the pdf $p(\beta', \varsigma'|s')$. For the real data set, the same type of pdf is used as for the synthetic data set. The independence of β' from ς' and s' is used to derive $p(\beta', \varsigma'|s') = p(\beta')p(\varsigma'|s')$, see Fig. 4. The probability density function $p(\varsigma'|s')$ is found by a computational process similar to the one which resulted in the covariance matrix of the standards for the Statistical Clone algorithm. There are two ways to determine $p(\beta')$. The

first method applies to cases where the element of the VNA which causes the largest part of the uncertainties is already characterized. This will most often be a cable which introduces transmission phase uncertainty. Such uncertainties can be directly incorporated into $p(\beta')$. The second method is iterative. It requires that the stability of the standards exceeds the stability of the VNA largely. The first step in this procedure is to perform several measurements of each calibration standard. Between the measurements the cables are moved as for the normal measurements but without disconnecting the standard. Second, one computes β' for each set of measured raw S-parameters with $\varsigma' = 0$ and an arbitrarily given $p(\beta')$. The differences between the resulting β' should equal differences predicted by $p(\beta')$. Now the function $p(\beta')$ can be modified until the differences of the resulting β' match the prediction of $p(\beta')$. In a final step, $p(\varsigma'|s')$ and $p(\beta')$ are multiplied.

The Plain LRL algorithm and Multical Clone do not require probability density functions or similar information. The other two algorithms require covariance matrices or a probability density function. It is intended to compare the results of the different algorithms. Thus one defines a probability density function like for the synthetic data set and derives the covariance matrices from this function, see section 4.7.2. The variances of the original probability density function are set to $\sigma_{\beta'}^2 = 5 \times 10^{-7}$ and $\sigma_{\varsigma'}^2 = 10^{-6}$. This way of generating covariance matrices and probability density function guarantees comparability of results.

4.8.2 Results of real data set

Figure 4.11 shows the measured reflection coefficients of the offset short which result from four calibration algorithms. The expected quasi exponential decay for the offset short is best realized with the Statistical Clone and the Monte-Carlo algorithm. The results of the Plain LRL algorithm suffer from switching between different lines, whereas the Multical Clone results show the effects of a badly calibrated tracking coefficient. The spikes on the traces are due to sampler bounce on a HP 8510 system.

Sampler bounce produces measured raw reflection coefficients which are larger in magnitude than expected. This is an error of the VNA and occurs only with highly reflective DUTs. Sampler bounce enters into the final measurement result in a multi stage process. First, the standards are measured. The measured raw S-parameters of the short are affected
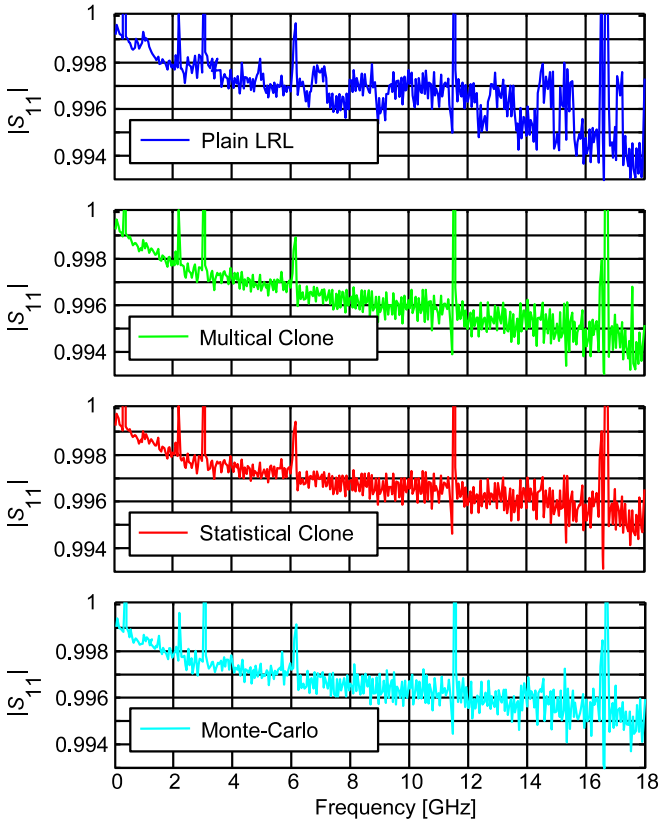
Figure 4.11: S_{11} magnitudes of the short after de-embedding with different calibration algorithms. The raw data is measured with a HP 8510 system. Spikes are due to sampler bounce in the VNA test set. The Plain LRL result shows the artifacts of changing pairs of lines. The Multical Clone results suffer from a tracking problem. The Statistical Clone and Monte-Carlo algorithm show rather similar realizations of the expected quasi exponential decay.

by sampler bounce. Next, the calibration algorithm computes the $\bar{v}$ from the erroneous r' and the specifications of the standards. As a consequence the $\bar{v}$ are incorrect as well. If they are used to de-embed the S-parameters of a DUT, which is not affected by sampler bounce, one should still see the
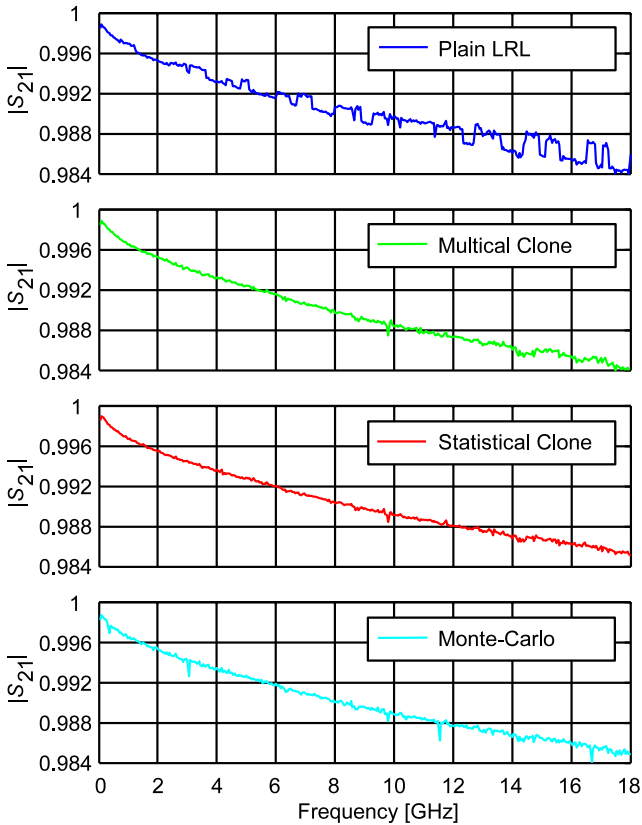
Figure 4.12: S_{21} magnitude of the 125 mm line after de-embedding with different calibration algorithms. The measurements are made with a HP 8510 system. Like in Fig. 4.11 the Plain LRL results show the switching between the lines and the tracking problem of Multical Clone is visible as well. Remaining spikes in the Monte-Carlo trace are a result of passivity constraints in the algorithm and sampler bounce in the VNA.

effects of sampler bounce during calibration. Figure 4.12 shows the transmission coefficient magnitude of the 125 mm line. The sampler bounce effects on the trace of Monte-Carlo are visible, whereas other algorithms do not show these artifacts. The reason for this is that the Monte-Carlo

algorithm assumes the offset shorts to be passive whereas the other algorithms do not. The Monte-Carlo and the Statistical Clone results are very close to the expected quasi exponential decay, whereas the Multiline Clone result suffers again from the tracking problem. The Plain LRL algorithm result shows again the line switching artifacts.

5 Calibration for Snap-on Connectors

Abstract—The introductory section describes the problems which arise during calibration with snap-on connectors. Next, these problems are analyzed in detail with a Monte Carlo simulation (MCS). The results of this MCS indicate that VNAs are best calibrated with metrology grade connectors and in a second step a pre-characterized adapter should be used to measure DUTs with industry grade connectors. In the following two adapter characterization techniques are presented in detail. The chapter ends with a comparison of both techniques.

5.1 Introduction

Practical LRL calibration tests with standards which are equipped with snap-on connectors of the MMPX type showed highly random calibration results. The reason for this failure lies in the construction of snap-on connectors.

The snap-on mechanism presses the female and male parts of the connector against each other. Obviously the forces of this mechanism are much smaller than the forces which can be exerted with a coupling nut. Thus snap-on connectors show a different mechanical and electrical length at each connection. This variability in length caused the failure of the LRL calibration.

The sensitivity of other calibration methods like short open load thru (SOLT) on the length variability can be assessed with a Monte Carlo simulation (MCS). The advantage of a MCS is that the calibration process can be modeled exactly. Disadvantages of the MCS are that it is computationally expensive and that there is in some cases no convergence. An extensive MCS of SOLT and LRL calibrations with snap-on connectors and with 1.85 mm connectors and subsequent adapter de-embedding showed that the best solution for snap-on connector calibration is a 1.85 mm connector calibration with a subsequent adapter de-embedding.

The adapter de-embedding is the critical point in the selected calibration method because the adapter has to be known for de-embedding. For

adapter characterization two new methods are tested. The short open thru (SOT) method uses a short, an open and a thru to characterize the adapters, whereas the other method employs bead-less adapters which are characterized by electromagnetic field simulation.

5.2 MCS of calibration methods

As already stated in the previous chapter, the uncertainty of a VNA measurement is a consequence of the uncertainties both of calibration standards and the VNA. The way how the latter uncertainties move forward to the final measurement uncertainties is a complicated multi-stage process. The first stage (calibration of the VNA) essentially results in the error box terms. Here the uncertainties of the standards and of the VNA mix and result in uncertain but correlated error box terms. In the second stage (measurement of DUT), the uncertain error box terms are used to calculate the S-parameters of the DUT. In this stage the uncertainties of the error box terms and of the DUT mix up and form the uncertainties of the measurement result. In particular the correlation of error box terms amongst each other poses a challenge to the statistical modeling of the measurement process. Note that the uncertainty distribution functions (with assumed parameters such as shape and variance) of the VNA error terms and the S-parameters of the standards mainly determine the final measurement uncertainties.

The guide to the expression of uncertainty in measurement (GUM), [50], defines a simplification of uncertainty computation. It consists in using the Taylor expansion of the equation which defines the measurand. This Taylor expansion is restricted to the linear terms of the involved random variables. The distribution of the measurement result is then computed by using the covariance matrix of the involved random variables for summation and quadrature, see [17]. Such an approach does not take into account the nonlinearities of the calibration and de-embedding equations.

The MCS presented here concentrates on the influence of non-ideal connectors on calibration accuracy. The connectors are modeled with random transmission phase and random reflection coefficients. Essentially the whole calibration and subsequent measurement process are simulated a couple of ten thousand times by starting with random input values for the standards. The resulting distribution of the S-parameters of a given
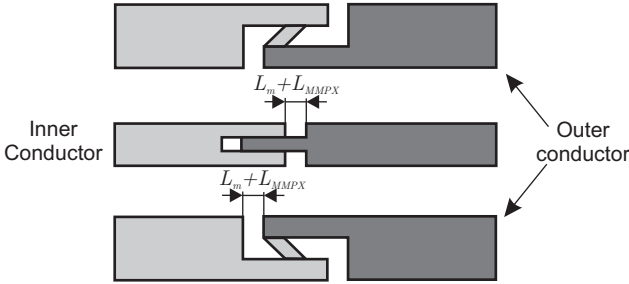
Figure 5.1: MMPX interface with random gap length $L_\mu + L_{MMPX}$. L_{MMPX} represents the varying part of the gap length, whereas L_μ represents the fixed length of the gap.

DUT is then analyzed using a statistics software.

This approach was particularly useful for studying different calibration techniques in conjunction with snap-on connectors which show large phase and small reflection coefficient variances. The MCS makes it possible to clearly distinguish between effects of transmission phase deviations and reflection coefficient deviations.

5.2.1 Uncertainties of the connectors

The snap-on connectors (MMPX connectors) investigated in this study, have shown a maximum measured transmission phase deviation of $\pm 1.5°$ at 65 GHz for the transmission term. The phase deviations stem from the variable gap length in the transmission path, see Fig. 5.1. The maximum measured reflection term uncertainty was -30 dB. In contrast the 1.85 mm connectors are more repeatable. They did not show significant phase deviations for the transmission term. The random part of their reflection coefficient varies within much lower limits which depend on the manufacturer and the present sample. One can surely assume that the random reflection coefficient is below -40 dB. These figures were derived from measurements of repeated connections.

For the snap-on connector as well as for the 1.85 mm connector, it is assumed that the phase of the transmission term and the complex reflection term are Gaussian distributed. Thus the 95 percent quantiles for the complex reflection term and for phase deviations were set to the mea-

sured maximum values. The measured transmission phase deviations of the snap-on connector are modeled by a random length variable L_{MMPX}. The statistical properties of this variable can be deduced from the transmission term phase measurements as

$$L_{MMPX} \sim N\left(0, \ 9.62714 \cdot 10^{-11}\right). \tag{5.1}$$

$N(\mu, \sigma^2)$ denotes a Gaussian distribution with mean μ and variance σ^2. As already mentioned the distribution of the length variable L_{MMPX} is chosen such that in 95 percent of the connections the length deviation from the mean transmission path length produces phase errors of less than $\pm 1.5°$ at 65 GHz. Axial offsets and various other effects cause reflection coefficient deviations. A complex random variable, R_{MMPX}, represents these complex deviations from the mean reflection coefficient

$$\mathrm{Re}\left\{R_{MMPX}\right\} \quad \sim \quad N\left(0, \ 2.60318 \cdot 10^{-4}\right) \tag{5.2}$$

$$\mathrm{Im}\left\{R_{MMPX}\right\} \quad \sim \quad N\left(0, \ 2.60318 \cdot 10^{-4}\right). \tag{5.3}$$

As for L_{MMPX} the variable R_{MMPX} is chosen such that 95 percent of the connections show a deviation of less than -30 dB from the mean return loss. Both L_{MMPX} and R_{MMPX} describe deviations from a mean connection.

For 1.85 mm connectors the phenomenon of varying transmission length is nearly inexistent due to the coupling nut, thus

$$L_{185} = 0. \tag{5.4}$$

The random reflection coefficient of the 1.85 mm connector is assumed to be below -40 dB. The resulting random variable is

$$\mathrm{Re}\left\{R_{185}\right\} \quad \sim \quad N\left(0, \ 2.60318 \cdot 10^{-5}\right) \tag{5.5}$$

$$\mathrm{Im}\left\{R_{185}\right\} \quad \sim \quad N\left(0, \ 2.60318 \cdot 10^{-5}\right). \tag{5.6}$$

5.2.2 Uncertainties of standards

The previously defined random variables can be used to specify the random S-parameters of calibration standards. Hereby the standards are assumed to be perfect but equipped with an imperfect connector. The

following equations hold for snap-on connector standards as well as for
1.85 mm standards:

$$S_{\mathrm{S}} = \begin{bmatrix} -e^{-2j\beta L_{1s}^{SOLT}} & 0 \\ \\ 0 & -e^{-2j\beta L_{2s}^{SOLT}} \end{bmatrix} \tag{5.7}$$

$$S_{\mathrm{O}} = \begin{bmatrix} e^{-2j\beta L_{1o}^{SOLT}} & 0 \\ \\ 0 & e^{-2j\beta L_{2o}^{SOLT}} \end{bmatrix} \tag{5.8}$$

$$S_{\mathrm{L}} = \begin{bmatrix} R_{11l}^{SOLT} & 0 \\ \\ 0 & R_{22l}^{SOLT} \end{bmatrix} \tag{5.9}$$

$$S_{\mathrm{T}} = \begin{bmatrix} R_{11t}^{SOLT} & \sqrt{1 - \left|R_{22t}^{SOLT}\right|^2}\,e^{-j\beta L_{1t}^{SOLT}} \\ \\ \sqrt{1 - \left|R_{11t}^{SOLT}\right|^2}\,e^{-j\beta L_{1t}^{SOLT}} & R_{22t}^{SOLT} \end{bmatrix}. \tag{5.10}$$

Here, the random variables R and L are not written with the connector
type as an index. Instead, they are indexed with the name of the standard
to which they belong, e.g., L_{1o}^{SOLT} is the random length variable of the
open at port one which is used for SOLT calibration. Connector reflection
coefficient deviations are not important for the high reflects S_{S} and S_{O}
because energy is reflected almost completely in the standards. Trans-
mission phase deviations are doubled for the high reflects because energy
has to transverse the connector twice. The connector of the load S_{L} is
assumed to have a reflection coefficient deviation of R_{11l}^{SOLT} from its mean
return loss, whereas the load element has been assumed to be perfect.
Imperfect load elements are not considered here, as only the influence
of connector deficiencies on calibration and measurement accuracy are of
interest. Note that the reflection term R is complex and describes the
phase and amplitude of the reflection coefficient deviation. The thru S_T
contains influences of reflection coefficient and phase variations. Passivity
of the thru is maintained by the square root term. Since energy passes
the connector only once, length deviations occur only once in the formula.

For thru reflect line (TRL) calibration standards with phase and amplitude deviations, the following S-parameters are used:

$$S_{\mathrm{T}} = \begin{bmatrix} R_{11t}^{TRL} & \sqrt{1 - \left|R_{22t}^{TRL}\right|^2}\, e^{-j\beta L_{1t}^{TRL}} \\ \sqrt{1 - \left|R_{11t}^{TRL}\right|^2}\, e^{-j\beta L_{1t}^{TRL}} & R_{22t}^{TRL} \end{bmatrix} \tag{5.11}$$

$$S_{\mathrm{R}} = \begin{bmatrix} -0.9 e^{-2j\beta L_{1r}^{TRL}} & 0 \\ 0 & -0.9 e^{-2j\beta L_{2r}^{TRL}} \end{bmatrix} \tag{5.12}$$

$$S_{\mathrm{L}} = \begin{bmatrix} R_{11l}^{TRL} & \sqrt{1 - \left|R_{22l}^{TRL}\right|^2}\,\Theta \\ \sqrt{1 - \left|R_{11l}^{TRL}\right|^2}\,\Theta & R_{22l}^{TRL} \end{bmatrix} \tag{5.13}$$

$$\Theta = e^{-j\beta(L_0 + L_{1l}^{TRL} + L_{2l}^{TRL})}. \tag{5.14}$$

The thru standard S_{T} is exactly the same as for the SOLT calibration. Influences of connector reflection coefficient and transmission phase deviations on the reflect standard S_{R} are treated in the same way as for high reflect standards of the SOLT calibration. Reflection coefficient deviations of the connectors of the line S_{L} are treated in the same way as for the thru. Transmission phase deviations for the line stem from two different connectors, hence the phase is a superposition of two independent random variables plus $L_0 = 5\,\mathrm{mm}$, the length of the line.

For the case of a 1.85 mm calibration and subsequent adapter de-embedding, the uncertainties on the adapters S-parameters contribute to the overall measurement uncertainty. Their influence is

$$S_{AdL} = \begin{bmatrix} R_{11a} & 1 \\ \sqrt{1 - |R_{11a}|} & 0 \end{bmatrix} \tag{5.15}$$

$$S_{AdR} = \begin{bmatrix} 0 & \sqrt{1 - |R_{22a}|} \\ 1 & R_{22a} \end{bmatrix}. \tag{5.16}$$

$$(5.17)$$

The random variables R_{iia} model the distribution of the random part of the connector reflection coefficient. The connection for the measurement of the DUT is assumed to be error free. This assumption is made due to the fact that all measurement methods require a connection between VNA and DUT. It is not intended to compute the total measurement uncertainty but to compare different calibration methods.

5.2.3 Test DUTs and the VNA

The following two DUTs were chosen as test DUTs:

$$S_{LR} = \begin{bmatrix} 0.1 & 0.9 \\ 0.9 & 0.1 \end{bmatrix} \qquad (5.18)$$

$$S_{HR} = \begin{bmatrix} 0.9 & 0.1 \\ 0.1 & 0.9 \end{bmatrix}. \qquad (5.19)$$

In the following these two devices will be called low reflect and high reflect DUTs. The low reflect DUT is a device with low reflection coefficients and high transmission coefficients, whereas the high reflect device exhibits low transmission coefficients and high reflection coefficients. As already mentioned, the connection between VNA and DUT is not taken into account, as the errors introduced by this connection are meaningless for the intended comparison of calibration techniques.

The VNA introduces random errors to the calibration, but they are neglected because they have much smaller influence on the calibration results than the assumed variability of the connectors. In practice it was found that even the values of the non random parts of the error terms have negligible influence on the results of the MCS. The main effect on the measurement uncertainty is due to the variance of the standards.

5.2.4 Monte Carlo Simulation

The impact of uncertain standards on calibration and measurement has been simulated 50'000 times for each frequency point and for SOLT and
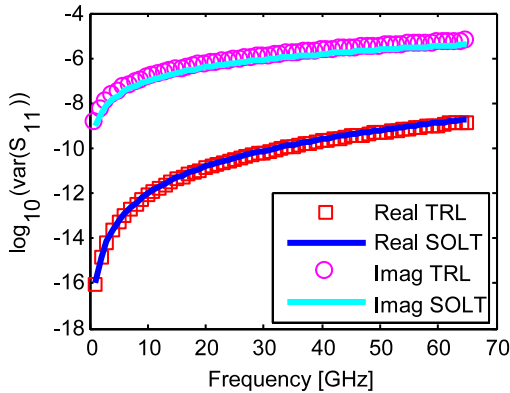
Figure 5.2: Variance of S_{11} of the low reflect using TRL and SOLT calibrations. Only phase errors are considered. Phase errors correspond to gap length variations. Note that the data points for the real part of SOLT and TRL calibration cover each other.

TRL calibrations using MUSE [18] and R [51]. The number of 50'000 samples for each frequency was determined in a convergence study. It was found that 50'000 samples are sufficient to guarantee the first two digits of the variance in Figs. 5.2-5.7. Calibrations with MMPX standards as well as calibrations with 1.85 mm standards plus the subsequent 1.85 mm to MMPX adapter de-embedding have been simulated. Low and high reflect DUTs were used to point out the different qualities of the respective calibration method. The frequency range is from 1 GHz up to 65 GHz.

Figures 5.2 to 5.5 show the measurement uncertainty resulting from calibration with MMPX connector equipped standards, whereas Figs. 5.6 and 5.7 show measurement uncertainty resulting from 1.85 mm calibration plus adapter de-embedding. By comparing both groups of graphs, one can conclude that using the adapter de-embedding method is advantageous.

Figures 5.2 and 5.4 display the measurement uncertainty only due to length variations in the transmission path. Surprisingly, in these figures the TRL variance graph is very similar to a SOLT calibration variance graph. If the electrical line length is outside of the range $20° \ldots 160°$, thru and line become too similar and the TRL calibration algorithm produces large errors. This behavior is well known from [49] and occurs only if there
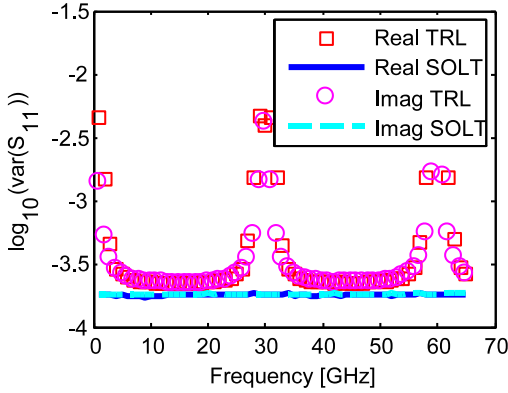
Figure 5.3: Same result as in Fig. 5.2 but additionally reflection errors are considered.
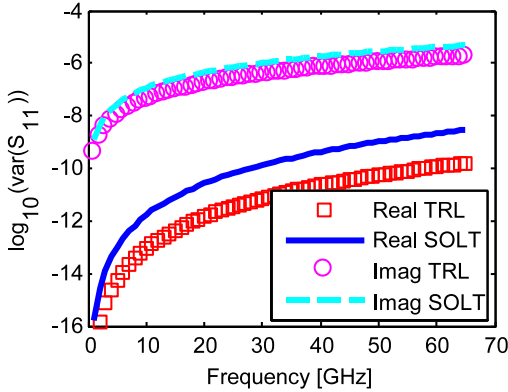
Figure 5.4: Variance of S_{21} of the high reflect using TRL and SOLT calibrations. Only phase errors are considered. Phase errors correspond to gap length variations.

are reflection coefficient variations in the S-parameters of the standards, see Figs. 5.3 and 5.5.
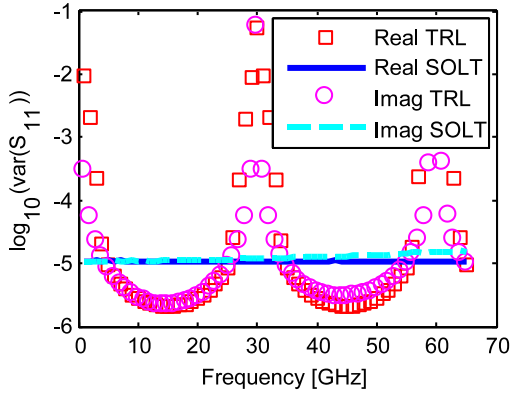
Figure 5.5: Same result as in Fig. 5.4 but additionally reflection errors are considered.
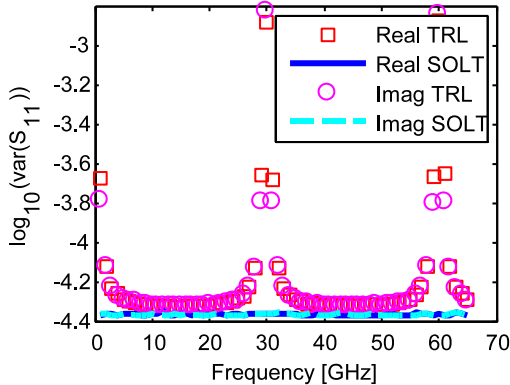
Figure 5.6: Variance of S_{11} of the low reflect using TRL and SOLT calibrations in combination with adapter de-embedding. Only reflection coefficient errors of the 1.85 mm connectors have been considered. Note that the data points for the real and imaginary part of the SOLT calibration cover each other. The points for the real and imaginary part of the TRL calibration cover each other partly.
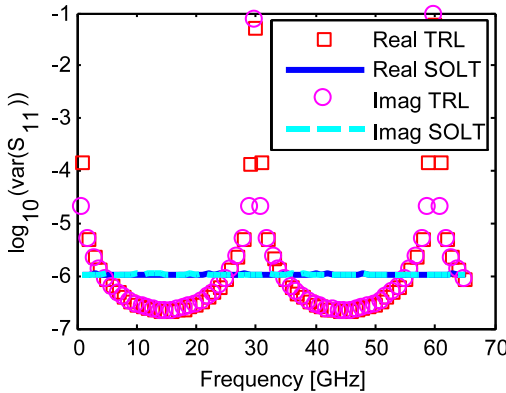
Figure 5.7: Variance of S_{21} of the high reflect using TRL and SOLT calibrations in combination with adapter de-embedding. Only reflection coefficient errors of the 1.85 mm connectors have been considered. Note that the data points for the real and imaginary part of the SOLT calibration cover each other. The points for the real and imaginary part of the TRL calibration cover each other partly.

5.3 Adapter characterization

As described in the previous section, the use of a calibration kit with industry grade connectors will introduce considerable error to the calibration with each required connection, [52]. A better approach is calibrating the VNA with metrology grade connectors (e.g., a 1.85 mm calibration kit) and performing the measurements using accurately characterized adapters. The accuracy of the adapter characterization is crucial and depends on the number of industry grade connections involved in the process.

Adapter characterization in general is addressed by a product note [53] which describes a technique called adapter removal method, requiring a complete two-port calibration for each connector family to characterize the adapters. If, e.g., the SOLT method is applied, seven industry grade connections are required. This number is too high and renders the adapter removal method unsuitable for adapters with industry grade connectors.

Adapter characterization is also important in the field of noise tem-
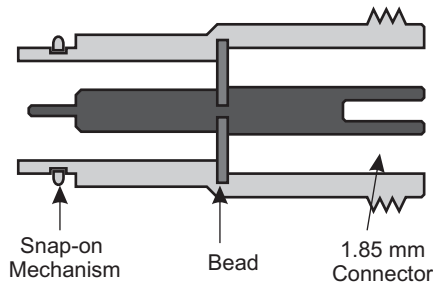
Figure 5.8: Schematic representation of a beaded adapter joining a MMPX and a 1.85 mm connector. The SOT method characterizes the 1.85 mm interface and the bead by measurements, while the snap-on interface will be characterized by simulation. The BA method characterizes the whole adapter by measurements.

perature measurements. In this context [54] describes a one-port sliding short method to characterize an adapter where only one industry grade connection is required. However, the production of an accurate sliding short for frequencies up to 65 GHz is very challenging.

An adapter characterization method requiring only short and open is described in [55]. This reflective termination method only partly characterizes the adapter. It is compared to both the adapter removal method of [53] and the sliding short method of [54]. The uncertainties of the adapter removal method are estimated to be larger than the uncertainties of the reflective termination method which in turn shows larger uncertainties than the sliding short method.

To overcome the shortcomings of the methods in [53] and [54], a two-port adapter characterization method which requires only opens, shorts and a thru connection between two adapters for their full characterization is developed. An improvement of characterization accuracy can be achieved by the BA method described in section 5.3.2, see [56]. Beadless adapters show very low reflections and have a nearly ideal behavior as opposed to the mechanically more robust beaded adapters. Finally, the accuracy and the ease of use of both methods are compared.
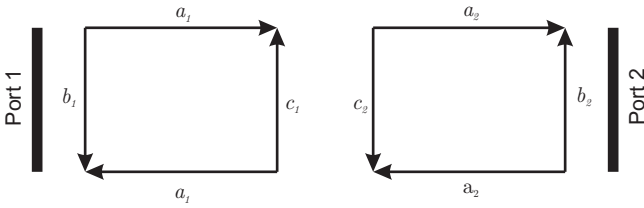
Figure 5.9: Signal flow graph of two reciprocal adapters with losses. Indices indicate the number of the adapter. Adapter 1 is mounted to port 1 and adapter 2 to port 2. The yet unknown S-parameters of the adapters are denoted with a_n, b_n and c_n.

5.3.1 Short-Open-Thru Method

Adapters are passive components made of linear isotropic materials, see Fig. 5.8. Thus one can consider adapters as reciprocal lossy two-ports. Figure 5.9 shows the signal flow graph of two adapters mounted to two VNA test ports. The latter are supposed to be calibrated with (metrology grade) 1.85 mm connectors, whereas different devices will be attached to the industry grade interface of the adapters. Note that the industry grade interface is considered as part of the device under test and the influence of the interface is not included in a_n, b_n, c_n (see Fig. 5.9).

Unlike the adapter removal method with SOLT calibration, the SOT adapter characterization does not require a load with industry grade interface due to the reciprocity of the adapter. This is an advantage because manufacturing of a load for the given frequency range is difficult and the number of required industry grade connections is reduced by omitting the load. The center conductor and short plane of the still required short standards with industry grade interface are lathed from a single piece of metal, whereas the open standards consist of plain outer conductors (see Fig. 5.10). Reflection coefficients of the opens and shorts including the industry grade interface are computed using a numerical field solver[1]. These simulations require to define the reference plane in a section where only one mode exists, i.e., not in the mid of the interface (see Fig. 5.11). As a consequence of this definition of the reference plane also the thru connection is simulated.

---

[1]CST Microwave Studio Version 5.1.3 June 27. 2005
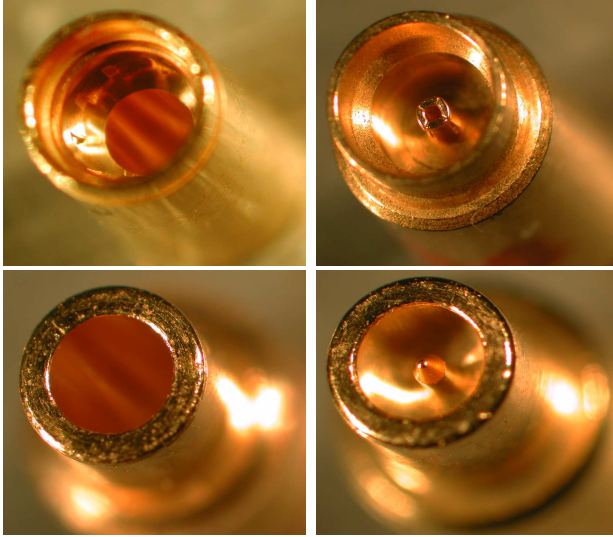
Figure 5.10: MMPX standards for the SOT method. Opens are displayed in the left column, whereas short standards are on the right side. In the upper row, the female standards are shown, while male standards are in the lower row.

Three measurements are needed to characterize the adapters with the SOT method: First, shorts equipped with industry grade connectors are measured with the adapters. Second, opens are measured with the adapters. Third, the thru connection of both adapters is measured.

Based on the flow graph shown in Fig. 5.9 the SOT measurements are described by the following set of equations:

$$S_{11\text{MT}} + \eta_1 = b_1 + a_1^2 \frac{S_{11\text{T}}(1 - c_2 S_{22\text{T}}) + S_{12\text{T}}^2 c_2}{D} \qquad (5.20)$$

$$S_{12\text{MT}} + \eta_2 = a_1 a_2 \frac{S_{12\text{T}}}{D} \qquad (5.21)$$

$$S_{22\text{MT}} + \eta_3 = b_2 + a_2^2 \frac{S_{22\text{T}}(1 - c_1 S_{11\text{T}}) + S_{12\text{T}}^2 c_1}{D} \qquad (5.22)$$

$$S_{11\text{MS}} + \eta_4 = b_1 + a_1^2 \frac{S_{11\text{S}}}{1 - c_1 S_{11\text{S}}} \qquad (5.23)$$
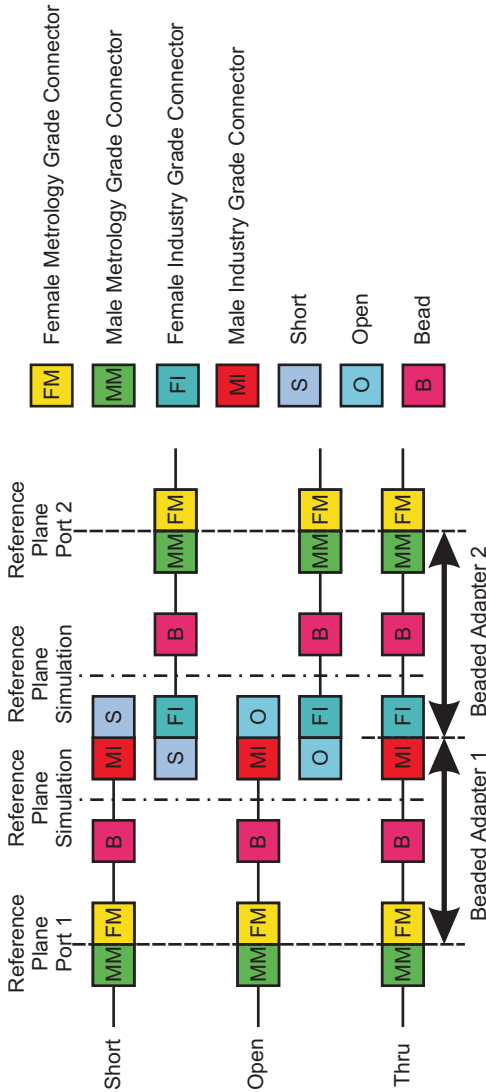
Figure 5.11: Calibration standards used for SOT adapter characterization. One pair of adapters is used for all three measurements. The reference planes of the VNA are depicted as well as the reference planes for the simulation of the standards.

$$S_{22\text{MS}} + \eta_5 = b_2 + a_2^2 \frac{S_{22\text{S}}}{1 - c_2 S_{22\text{S}}} \tag{5.24}$$

$$S_{11\text{MO}} + \eta_6 = b_1 + a_1^2 \frac{S_{11\text{O}}}{1 - c_1 S_{11\text{O}}} \tag{5.25}$$

$$S_{22\text{MO}} + \eta_7 = b_2 + a_2^2 \frac{S_{22\text{O}}}{1 - c_2 S_{22\text{O}}} \tag{5.26}$$

$$D = 1 - c_1 S_{11\text{T}} - c_2 S_{22\text{T}} - c_1 c_2 S_{12\text{T}}^2 + c_1 c_2 S_{11\text{T}} S_{22\text{T}}.$$

Here index M stands for measured values, whereas its absence indicates standard (simulated) values. T signifies the thru, S the short, O the open and a_n, b_n, c_n are the S-parameters of the adapters to be characterized. The η_i denote the unavoidable measurement errors. This system of equations is over-determined and can be solved using a least squares approach minimizing the sum of the errors $\sum_{i=1}^{7} |\eta_i|^2$. Since the unknowns a_n, b_n, c_n are nonlinear quantities, the `lsqnonlin` optimizer of the Matlab Optimization Toolbox is used. Reasonable starting values are, e.g.,

$$a_1 = a_2 = \sqrt{S_{12\text{MT}}} \tag{5.27}$$

which physically correspond to phase-matched adapters with equal transmission characteristics, small reflection terms c_1 and c_2 and $S_{12\text{T}} = 1$ to fulfill (5.21) with small error.

As already mentioned in the introduction of this section, initially the parameters a_n, b_n, c_n do not include the influences of the industry grade interface (see Fig. 5.11). The complete S-parameters of the adapter can be obtained by appending the industry grade interface $S_{11\text{T}}, \sqrt{S_{21\text{T}}}$ and $\sqrt{S_{12\text{T}}}$ to adapter 1 and by putting $S_{22\text{T}}, \sqrt{S_{21\text{T}}}$ and $\sqrt{S_{12\text{T}}}$ to adapter 2. The results of this algorithm can be seen in Fig. 5.12 and Fig. 5.13.

5.3.2 Beadless Adapter Method

In contrast to the beaded adapters described in the previous section, beadless adapters show an (electrically) almost ideal behavior with very low reflection. Their S-parameters are given with high accuracy by simple formulae. But they are mechanically fragile and therefore not very suitable for everyday use. However, for the characterization of beaded adapters they open the way to a rather accurate procedure. Essentially, only three thru measurements need to be performed. In the first measurement, both
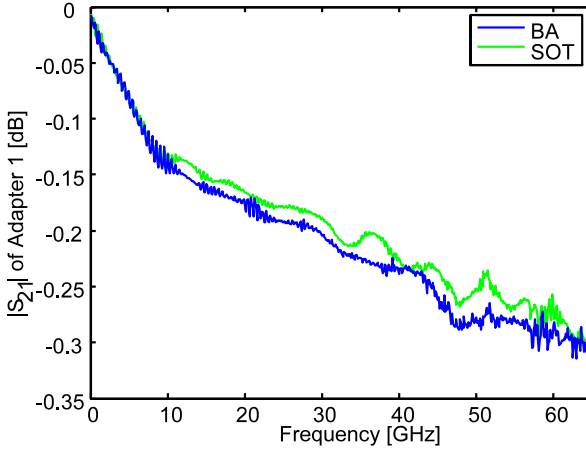
Figure 5.12: S_{21} of the adapter as a result of the SOT and BA methods. The ripple in the transmission term is a result of poor calibration of the VNA and reflections of the adapters.

beadless adapters are connected to form a thru connection. The second measurement is a thru connection of a beadless adapter at port 1 and a beaded adapter at port 2. For the third measurement, the beadless adapter at port 1 is replaced with a beaded one and vice versa at port 2.

Specially manufactured beadless adapters are used for this adapter characterization method, see Fig. 5.14. One can assume that the reflection terms S_{11L1}, S_{11L2}, S_{22L1} and S_{22L2} of both beadless adapters are quite small. If a simple $e^{\gamma l}$ wave transmission through the beadless adapters is assumed (with the propagation constant γ to be determined by measurement), one can easily determine the S-parameters of both beadless adapters:

$$\gamma = \frac{\ln(S_{21\text{ML1L2}})}{l_1 + l_2} \tag{5.28}$$

$$S_{21\text{L1}} = e^{\gamma l_1} = S_{12\text{L1}} \tag{5.29}$$

$$S_{21\text{L2}} = e^{\gamma l_2} = S_{12\text{L2}} \tag{5.30}$$

$$S_{11\text{L1}} = S_{22\text{L1}} = S_{11\text{L2}} = S_{22\text{L2}} = 0. \tag{5.31}$$

Here $S_{21\text{ML1L2}}$ signifies the measured transmission of both beadless adapters.
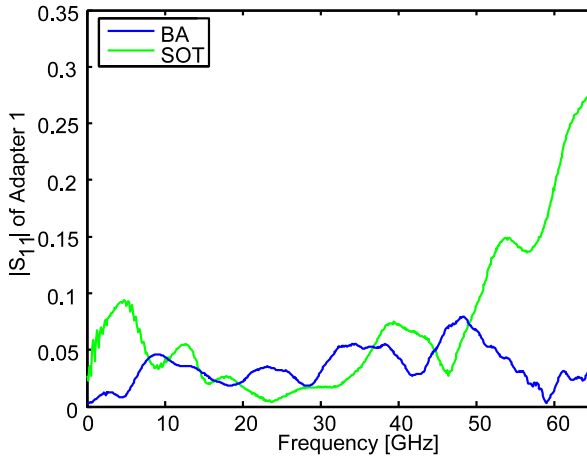
Figure 5.13: S_{11} of the adapter at port 1 as a result of the SOT and BA method. Beadless adapter characterization and the SOT method show large differences for frequencies larger than 50 GHz.
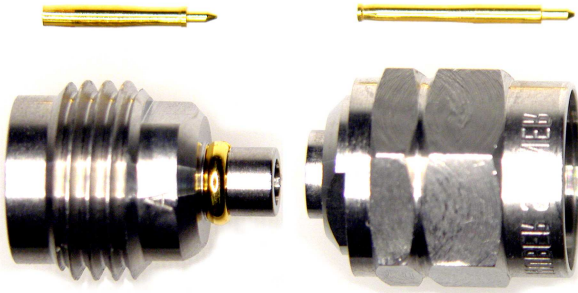
Figure 5.14: Beadless adapters between MMPX interface and 1.85 mm interface. The length of the adapters was reduced to a minimum to reduce unwanted reflections and to ease mounting of the adapters.

This model of the beadless adapter does not fully account for the influence of metrology grade interface, diameter transition and industry grade interface. Reflections from the diameter transition and the connectors are neglected because they are small compared to typical S-parameter mea-

surement uncertainties of transparent devices, see [57]. The influence of connectors and diameter transitions on the transmission coefficients of the beadless adapters is approximated by (5.29) and (5.30).

If $\mathbf{T}_{B1}$ and $\mathbf{T}_{B2}$ denote the (yet unknown) T-matrices of beaded adapters, the T-matrices of the aforementioned combinations of a beaded and a beadless adapter can be written as $\mathbf{T}_{B1}\mathbf{T}_{L2}$ and $\mathbf{T}_{L1}\mathbf{T}_{B2}$ respectively. Equating this with the measured T-matrices leads to

$$\mathbf{T}_{B2} = \mathbf{T}_{L1}^{-1}\mathbf{T}_{ML1B2}, \tag{5.32}$$
$$\mathbf{T}_{B1} = \mathbf{T}_{MB1L2}\mathbf{T}_{L2}^{-1}. \tag{5.33}$$

Here (5.32) uses the second measurement to de-embed the T-parameters $\mathbf{T}_{B2}$ of the beaded adapter at port 2. Equation (5.33) de-embeds the T-parameters $\mathbf{T}_{B1}$ of the beaded adapter at port 1 by using the third measurement result. Finally, the T-parameters of the beaded adapters can be converted back to the respective S-parameters. In Fig. 5.12 and 5.13, the results of the SOT method is compared with this approach.

5.3.3 Comparison

The number of industry grade connections required is an indicator for the quality of the methods compared. The BA method requires 3 connections for 2 adapters, whereas the SOT method requires 5 connections for the same task. A second indicator, which confirms this initial estimation of accuracy, is the difference between the measured and the computed thru connection of two beaded adapters, see Fig. 5.15. Cascading the adapter S-parameters resulting from one of the two methods yields a computed thru connection. One would expect the SOT method to outperform the BA method because the SOT characterization uses the thru connection as a standard, but evidently this advantage of the SOT method is more than compensated by its inaccuracies in measurement and standard definition. Regarding the BA method, only the delicate connection process of the beadless adapters is a drawback. Care must be taken to ensure that the center conductors mate correctly during the connection process.
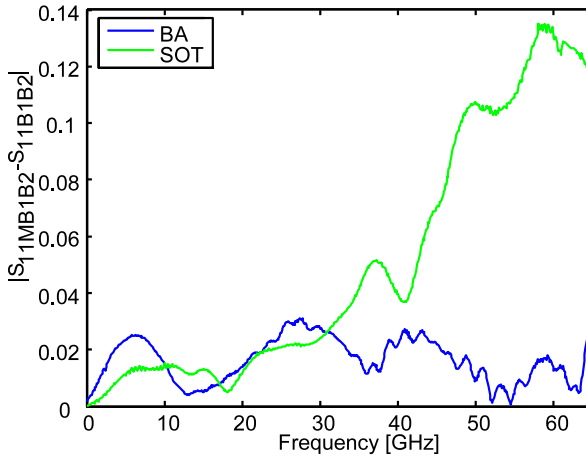
Figure 5.15: Difference between the measured reflection at port 1 of a thru connection of both beaded adapters $S_{11\mathrm{MB1B2}}$ and the results due to adapter characterization and subsequent cascading of the two beaded adapters $S_{11\mathrm{B1B2}}$. The superiority of the BA method is visible for frequencies larger than 30 GHz.

6 Conclusion

The main goal of this thesis is to make S-parameter measurements up to 70 GHz traceable. This means a mathematical model of the measurement process is required.

A rather surprising fact is that there is apparently no solid mathematical theory about what mode is measured by a VNA. This comes from the fact that proofs of completeness for the solution of Maxwell's equations are quite difficult in the case of lossy wave guides. Nonetheless, one practically knows that the fundamental mode is measured. The computation of the fundamental mode requires the dimensions and material parameters of the coaxial transmission line. While the fundamental modes of lossless and lossy smooth transmission lines are well-known, a new method to compute the propagation constant of the fundamental mode in a lossy rough line is presented in chapter two. The implications of roughness on S-parameters are clearly described. While the impact of surface roughness in the test port on the achievable accuracy of a VNA is rather small, it has a noticeable impact on the propagation constant.

The accurate computation of the propagation constant plays a crucial role in the computation of standards. Basically each standard which contains a piece of rough transmission line can only be characterized if the propagation constant is known. The possibly even more fundamental model of the slotted 1.85 mm connector is described in chapter three. Starting with FDTD and FEM simulations of the connector, a database lookup program is developed which computes the S-parameters of connectors with arbitrary geometry within seconds. The simulations which were used to build up the database are validated by comparison between FDTD and FEM results. Chapter three concentrates on the characterization of transmission line standards and offset shorts. The transmission line standards can be readily characterized by their connector geometry, diameter profiles, conductivity and plating roughness parameters. The latter data is used to compute the S-parameters of the line. The connector geometry is used to compute the S-parameters of the connector. Finally, the complete S-parameters are computed by cascading the S-matrices of line

and connector. For the offset shorts a similar approach is chosen. The short plane is the only new element which has to be characterized. It is characterized by its diameters and its conductivity. No other standards are computed because for coaxial calibration the offset short and the transmission lines seem to be the most accurate, traceable standards.

Chapter four gives a new general theory of VNA calibration. First, a model of the VNA measurement process is constructed. Thereby the definition of the standards is assumed to be erroneous and the model of the VNA is assumed to be incorrect. This model of how inaccuracies enter the calibration process is new and results in advantageous properties like robustness of the algorithm and better accuracy as other calibration algorithms. These advantages are due to the fact that the used error model is close to the physical reality. Defining random variables and modeling the errors as probability density functions (pdfs) are prerequisites to the construction of a pdf for the calibration coefficients via Bayes' law. Now one can take the mean value of this pdf to estimate the true VNA parameters. The numerical computation of this mean value requires the use of nonlinear optimization techniques and Monte-Carlo integration. The new calibration algorithm is compared to already known calibration algorithms with synthetic and real data. Here synthetic data stands for entirely simulated calibration scenarios, whereas real data refers to real calibration scenarios. The new algorithm is more precise and accurate than the other algorithms in all tested scenarios.

The new algorithm models the influence of several error sources on the calibration result. In contrast to that, the calibration accuracy with snap-on connectors is dominated by a single error source, namely the instable transmission phase of the snap-on mechanism. In chapter five the impact of this length variability on different VNA calibrations is investigated by using Monte Carlo simulations (MCSs). Only very small accuracy can be achieved with standard calibration methods. However, a calibration with 1.85 mm connectors followed by an adapter de-embedding yields higher accuracy. For this reason two new adapter characterization techniques are investigated. A first method relies on the standards short open and thru connection, while the second, more accurate, method uses computationally characterized beadless adapters as standards. Both methods are validated by the following test: First, two beaded adapters are characterized with the method under consideration. Next, the S-parameters of the two beaded adapters are computed and measured. The difference between

the computed and measured S-parameters indicates the accuracy of the adapter characterization method.

7 Outlook

This thesis provides the theory for traceable coaxial S-parameter measurements up to 70 GHz. A direct extension of this work is the application of the presented theory to slotted and slotless coaxial connectors like the 3.5 mm, 2.92 mm, 2.4 mm and 1 mm connectors. Other VNA measurement applications such as rectangular waveguide measurements or on-wafer measurements can also benefit from the presented theory.

Concerning the computation of standards, the probably most evident and useful extension would be to compute the S-parameters of other connector families. This would help to reduce the uncertainty budget of measurements with these connectors. At the same time, the standards could be defined more accurately and connectors could be optimized for lower return loss and higher repeatability.

The surface impedance computed with the MMP method can be used to compute the propagation constant of rectangular and circular wave guides. This is especially important for sub-THz applications which use offset short calibration.

Another possibility is to develop new high precision standards. This could result in standards which can produce several computable reflection coefficients by changing the standard in a well controlled way. Hence one could perform a calibration with only one connection. By repeated use of such standards one could fully even out the random influence of the connector.

While the presented calibration algorithm is capable of m-port calibrations with arbitrary models of the VNA, such computations are prohibitive in terms of computation time. More efficient algorithms which retain the correct modeling of the errors in the standards and the VNA and thus the robustness and accuracy of the presented algorithm could be developed for multi port calibrations. In this context existing Gibbs sampling algorithms can be used.

The concept of adapter characterization and de-embedding could be extended to other connector families. Substantial savings can be expected from this method as several calibration kits for industry grade connectors

can be made obsolete with a set of well characterized adapters.

A S-parameters

S-parameters are always stated with respect to the characteristic impedance of the ports under consideration. The characteristic impedance depends, as stated in section 2.6, on the measured mode and the wave guide. In other words, the test port adapters and the calibration kit determine the characteristic impedance of the calibrated VNA. It is necessary to normalize the S-parameters to a reference impedance before comparing S-parameters which are measured with VNAs calibrated with differing calibration kits and test port adapters. Typical reference impedances are $Z_{ref} = 50\,\Omega$ and $Z_{ref} = 75\,\Omega$. The reference impedance can be chosen arbitrarily and should not be mixed up with the characteristic impedance which is based on the electromagnetic fields of the mode under consideration.

According to [11] one can convert the S-matrices introduced in section 2.6 to an impedance matrix

$$\mathbf{Z} = (\mathbf{I} - \mathbf{U}^{-1}\mathbf{S}\mathbf{U})^{-1}(\mathbf{I} + \mathbf{U}^{-1}\mathbf{S}\mathbf{U})\mathbf{Z}_{ref} \tag{A.1}$$

which relates waveguide currents to waveguide voltages. Here $\mathbf{I}$ is the unity matrix, $\mathbf{U}$ is a diagonal matrix

$$\mathbf{U} = diag\left(\frac{\sqrt{\mathrm{Re}\left\{Z_{ref}^i\right\}}}{|Z_{ref}^i|}\right) \tag{A.2}$$

and $\mathbf{Z}_{ref}$ is a diagonal matrix with the reference impedances of all ports Z_{ref}^i as diagonal elements. Equation (A.1) can be used to adjust the reference impedance of a given S-matrix by the following procedure. First, one computes the impedance matrix. Then matrices $\mathbf{U}$ and $\mathbf{Z}_{ref}$ are built according to the desired reference impedances. Finally, the new S-matrix is computed

$$\mathbf{S} = \mathbf{U}(\mathbf{Z} - \mathbf{Z}_{ref})(\mathbf{Z} + \mathbf{Z}_{ref})^{-1}\mathbf{U}^{-1}. \tag{A.3}$$

Another advantage of S-parameter notation is that the S-matrix of two coupled DUTs can be computed from the S-matrices of the individual DUTs. This can be achieved in a three step procedure. First, one adjusts the reference impedances of the connecting ports to one impedance level. Then the S-matrices of the DUT are combined to one system of equations. Care must be taken that the scattered and incident wave quantities $\vec{a}$ and $\vec{b}$ of the connected ports are correctly stated. Rearranging of the system of equations yields the combined S-matrix. In the case of two port devices, the rearranging of the system of equations can be avoided by using T-parameters. Two port S-parameters can be transformed to T-parameters by

$$\mathbf{T} = \begin{pmatrix} -\frac{S_{11}S_{22} - S_{12}S_{21}}{S_{21}} & \frac{S_{11}}{S_{21}} \\ -\frac{S_{22}}{S_{21}} & \frac{1}{S_{21}} \end{pmatrix}. \tag{A.4}$$

Note that S_{21} should not be zero for this transformation. T-parameter matrices can be cascaded by matrix multiplication

$$\mathbf{T}_c = \mathbf{T}_a \mathbf{T}_b. \tag{A.5}$$

Where $\mathbf{T}_a$ and $\mathbf{T}_b$ are the individual T-matrices and $\mathbf{T}_c$ is the combined T-matrix of DUTs a and b. The transformation from T-parameters to S-parameters is

$$\mathbf{T} = \begin{pmatrix} \frac{T_{12}}{T_{22}} & \frac{T_{11}T_{22} - T_{12}T_{21}}{T_{22}} \\ \frac{1}{T_{22}} & -\frac{T_{21}}{T_{22}} \end{pmatrix}. \tag{A.6}$$

Note that T_{22} should not be zero for this transformation.

B Hankel Functions

Hankel functions might be difficult to evaluate with Bessel and Neumann functions for big arguments in the upper right complex plane because of a loss of accuracy when adding Bessel and Neumann function. This problem can be overcome by using the following asymptotic expansions

$$
\begin{aligned}
\underline{H}_n^{(2)}(z) \approx{}& \sqrt{\frac{2}{\pi z}} e^{-j\left(z-\frac{\pi}{2}n-\frac{\pi}{4}\right)} \\
&\times \sum_{k=0}^{N} \frac{1}{(2jz)^k} \frac{\Gamma(n+k+0.5)}{k!\Gamma(n-k+0.5)}
\end{aligned}
\tag{B.1}
$$

$$
\begin{aligned}
\underline{H}_n^{(1)}(z) \approx{}& \sqrt{\frac{2}{\pi z}} e^{j\left(z-\frac{\pi}{2}n-\frac{\pi}{4}\right)} \\
&\times \sum_{k=0}^{N} \frac{(-1)^k}{(2jz)^k} \frac{\Gamma(n+k+0.5)}{k!\Gamma(n-k+0.5)}.
\end{aligned}
\tag{B.2}
$$

Where Γ is the Gamma function. The deviation from the actual value is less than the last term in the sum. Note that increasing N does not necessarily result in increased accuracy as this is an asymptotic expansion. For the range of arguments useful for the problem of a coaxial line, a good value for N has been $N = 90$ resulting in approximately 80 useful digits for the Hankel function. See for further details [58].

C Air Line Data

Special measurement adapters are used for the compressed length measurements of the air lines. The special adapters consist of a male or female connector fixed on a reference plate. First, the male and female special adapters are connected to each other and the coupling nut is tightened with the prescribed torque. Then the distance between the two reference plates of the special adapters is measured with a laser interferometer. Next, the air line is connected to the two special adapters. Thereby the connectors are torqued down to the prescribed torque. The length of air line plus special adapters is again measured with a laser interferometer. Last, the length of the special adapters is subtracted from the previous measurement result.

Torquing down the air lines connectors creates pressure on the mating planes. The pressure compresses the outer conductor between mating plane and the point where the coupling nut makes contact to the outer conductor. Length measurements in the compressed and uncompressed state showed that compression can cause a length reduction of up to $6\,\mu$m in a 1.85 mm air line. It is appropriate to use the compressed length because during VNA measurements the air line is in its compressed state. The length measurements are conducted at 20° Celsius and are converted to 23° Celsius via the thermal expansion coefficient of beryllium copper. This is because dimensional laboratories work at 20° Celsius and electrical laboratories work at 23° Celsius. The uncertainty of the compressed length depends on the straightness of the transmission line. A typical U95 value is $3\,\mu$m.

Table C.1: 1.85 mm Air Lines Measurement

Length	Inner Diameter	Outer Diameter
14.9958 mm	0.8021 mm	1.8490 mm

Table C.1: Continuation

Length	Inner Diameter	Outer Diameter
16.3499 mm	0.8031 mm	1.8481 mm
18.5760 mm	0.8020 mm	1.8498 mm
23.0732 mm	0.8029 mm	1.8513 mm
29.9756 mm	0.8006 mm	1.8494 mm
Mean	0.8021 mm	1.8495 mm

The diameters of the inner conductor are measured with a laser scanner system at 23° Celsius. Here the U95 uncertainty is typically $1\,\mu$m. The diameters of the outer conductor are measured with an air gauge at 23° Celsius. Here the U95 uncertainty is typically $1.5\,\mu$m. All mechanical measurements listed in tables C.1 and C.2 are performed at METAS Switzerland.

Table C.2: 2.4 mm Air Lines Measurement

Length	Inner Diameter	Outer Diameter
14.967 mm	1.0420 mm	2.3975 mm
17.493 mm	1.0425 mm	2.3975 mm
29.997 mm	1.0424 mm	2.3974 mm

Table C.2: Continuation

Length	Inner Diameter	Outer Diameter
49.955 mm	1.0413 mm	2.3989 mm
Mean	1.0421 mm	2.3978 mm

The plating thickness of all transmission lines is $a_3 - a_1 = b_1 - b_3 = 1\,\mu\text{m}$, the average roughness height is $a_1 - a_2 = b_2 - b_1 = 0.45\,\mu\text{m}$, the average roughness period is $p = 1\,\mu\text{m}$ and the conductivity of the hard gold plating is $\sigma_2 = 7.57{\times}10^6\,\frac{\text{S}}{\text{m}}$. No reliable information about the conductivity of the used beryllium copper were available. The input data, which is presented in Table C.3, is compiled from length and diameter measurements, from roughness parameters and from electrical parameters of the transmission lines.

Table C.3: Air Lines Simulation

	Hoffmann	Hoffmann	Daywitt	Sanderson
	2.4 mm	1.85 mm	1.85 mm	1.85 mm
ϵ_1	$1.000649\epsilon_0$	$1.000649\epsilon_0$	$1.000649\epsilon_0$	$1.000649\epsilon_0$
μ_1	μ_0	μ_0	μ_0	μ_0
$\underline{\epsilon}_2$	$\epsilon_0 - \frac{j\sigma_2}{\omega}$	$\epsilon_0 - \frac{j\sigma_2}{\omega}$	$\epsilon_0 - \frac{j\sigma_2}{\omega}$	$\epsilon_0 - \frac{j\sigma_2}{\omega}$
σ_2	$7.57{\times}10^6\,\frac{\text{S}}{\text{m}}$	$7.57{\times}10^6\,\frac{\text{S}}{\text{m}}$	$7.4{\times}10^6\,\frac{\text{S}}{\text{m}}$	$1.14{\times}10^7\,\frac{\text{S}}{\text{m}}$

Table C.3: Continuation

	Hoffmann	Hoffmann	Daywitt	Sanderson
μ_2	μ_0	μ_0	μ_0	μ_0
$\underline{\epsilon}_3$	$\epsilon_0 - \frac{j\sigma_3}{\omega}$	$\epsilon_0 - \frac{j\sigma_3}{\omega}$	-	-
σ_3	$1.6 \times 10^7 \frac{\text{S}}{\text{m}}$	$1.6 \times 10^7 \frac{\text{S}}{\text{m}}$	-	-
μ_3	μ_0	μ_0	-	-
a_1	$520.27 \, \mu\text{m}$	$400.32 \, \mu\text{m}$	-	-
a_2	$519.82 \, \mu\text{m}$	$399.87 \, \mu\text{m}$	-	-
a_3	$521.27 \, \mu\text{m}$	$401.32 \, \mu\text{m}$	$401.1 \, \mu\text{m}$	$401.32 \, \mu\text{m}$
a_4	$520.82 \, \mu\text{m}$	$400.87 \, \mu\text{m}$	-	$400.87 \, \mu\text{m}$
b_1	$1199.7 \, \mu\text{m}$	$925.56 \, \mu\text{m}$	-	-
b_2	$1200.1 \, \mu\text{m}$	$926.01 \, \mu\text{m}$	-	-
b_3	$1198.7 \, \mu\text{m}$	$924.56 \, \mu\text{m}$	$924.8 \, \mu\text{m}$	$924.56 \, \mu\text{m}$
b_4	$1199.1 \, \mu\text{m}$	$925.01 \, \mu\text{m}$	-	$925.01 \, \mu\text{m}$
p	$1 \, \mu\text{m}$	$1 \, \mu\text{m}$	$1 \, \mu\text{m}$	$1 \, \mu\text{m}$

D Unbiased Variance Optimal Estimator

According to [45] the estimator is unbiased if and only if

$$\int_{\mathbb{C}^{n+q+lm2}} (E(r', s'_d) - (v, s'_u))p(r'|v, s'_u, s'_d)\, dr'\, p(v, s'_u)\, dv\, ds'_u = 0 \qquad \text{(D.1)}$$

holds. This integral and the following integrals in this section are componentwise integrals over the whole complex plane. The order of integration can be changed as the distribution $p(r', v, s'_u|s'_d)$ follows the conditions of Fubini's theorem, see [59]. Thus

$$\int_{\mathbb{C}^{lm2+n+q}} (E(r', s'_d) - (v, s'_u))p(v, s'_u|r', s'_d)\, dv\, ds'_u\, p(r'|s'_d)\, dr' = 0 \qquad \text{(D.2)}$$

holds as well. A stronger request would be

$$\int_{\mathbb{C}^{n+q}} (E(r', s'_d) - (v, s'_u))p(v, s'_u|r', s'_d)\, dv\, ds'_u = 0. \qquad \text{(D.3)}$$

Now it is clear that an unbiased estimator of (v, s'_u) is

$$E(r', s'_d) = \int_{\mathbb{C}^{n+q}} (v, s'_u)p(v, s'_u|r', s'_d)\, dv\, ds'_u. \qquad \text{(D.4)}$$

The variance of an estimator is

$$\text{var} = \int_{\mathbb{C}^{n+q+lm2}} |E(r', s'_d) - (v, s'_u)|^2 p(r'|v, s'_u, s'_d)\, dr'\, p(v, s'_u)\, dv\, ds'_u. \qquad \text{(D.5)}$$

Similar to the already given argument for the unbiasedness the order of integration is exchanged

$$\text{var} = \int_{\mathbb{C}^{lm2+n+q}} |E(r', s'_d) - (v, s'_u)|^2 p(v, s'_u|r', s'_d)\, dv\, ds'_u\, p(r'|s'_d)\, dr'. \qquad \text{(D.6)}$$

As $p(r'|s_d')$ is strictly positive it is equivalent to force

$$\text{var}' = \int_{\mathbb{C}^{n+q}} |E(r', s_d') - (v, s_u')|^2 p(v, s_u'|r', s_d') \, dv \, ds_u' \qquad \text{(D.7)}$$

to be minimal for all r'. This is already achieved by the unbiased $E(r', s_d')$.

Bibliography

[1] G. Grau, *Quantenelektronik.* Braunschweig, Germany: Vieweg, 1978.

[2] P. Leuchtmann, *Einführung in die elektromagnetische Feldtheorie.* Munich, Germany: Pearson, 2005, ch. 11. Die Führung elektromagnetischer Wellen, pp. 329–343.

[3] R. E. Collin, *Field Theory of Guided Waves.* New York, USA: IEEE Press, 1990, ch. 5. Waveguides and Cavities, pp. 330–404.

[4] J. A. Stratton, *Electromagnetic Theory.* Hoboken, USA: John Wiley & Sons, Inc., 2007, ch. IX. Coaxial Lines, pp. 545–554.

[5] W. C. Daywitt, "First-order symmetric modes for a slightly lossy coaxial transmission line," *IEEE Transactions on Microwave Theory and Techniques*, vol. 38, no. 11, pp. 1644–1650, Nov. 1990.

[6] ——, "Exact principal mode field for a lossy coaxial line," *IEEE Transactions on Microwave Theory and Techniques*, vol. 39, no. 8, pp. 1313–1322, Aug. 1991.

[7] ——, "The propagation constant of a lossy coaxial line with a thick outer conductor," *IEEE Transactions on Microwave Theory and Techniques*, vol. 43, no. 4, pp. 907–911, Apr. 1995.

[8] A. E. Sanderson, *Advances in Microwaves*, L. Young, Ed. New York, USA: Academic Press, Inc., 1971.

[9] T. Watanabe, Y. Choyal, K. Minami, and V. L. Granatstein, "Range of validity of the rayleigh hypothesis," *Physical Review E*, vol. 69, no. 5, p. 056606, May 2004.

[10] T. C. Paulick, "Applicability of the rayleigh hypothesis to real materials," *Physical Review B*, vol. 42, no. 5, pp. 2801–2824, Aug. 1990.

[11] R. B. Marks and D. F. Williams, "A general waveguide circuit theory," *Journal of Research of the National Institute of Standards and Technology*, vol. 97, no. 5, pp. 533–562, Sept. 1992.

[12] R. B. Marks, "A multiline method of network analyzer calibration," *IEEE Transactions on Microwave Theory and Techniques*, vol. 39, no. 7, pp. 1205–1215, July 1991.

[13] D. C. DeGroot, J. A. Jargon, and R. B. Marks, "Multiline TRL revealed," in *ARFTG Conference Digest*, vol. 60, Dec. 2002, pp. 131–155.

[14] M.J.Gans, "A general proof of floquet's theorem (correspondence)," *IEEE Transactions on Microwave Theory and Techniques*, vol. 13, no. 3, pp. 384–385, May 1965.

[15] C. Hafner, *Post-modern electromagnetics using intelligent Maxwell solvers.* New York, USA: John Wiley & Sons, 1999.

[16] D. Williams and B. Alpert, "Causality and waveguide circuit theory," *IEEE Transactions on Microwave Theory and Techniques*, vol. 49, no. 4, pp. 615–623, Apr. 2001.

[17] B. Hall, "Calculating measurement uncertainty for complex-valued quantities," *Measurement Science and Technology*, vol. 14, pp. 368–375, February 2003.

[18] "Measurement Uncertainty Reasearch Group : *MUSE*-softwarepackage, ETH-Zurich & Empa, *http://www.mu.ethz.ch.*"

[19] P. Leuchtmann and J. Ruefenacht, "On the calculation of the electrical properties of precision coaxial lines," *IEEE Transactions on Microwave Theory and Techniques*, vol. 53, no. 2, pp. 392–397, Apr. 2004.

[20] J. Whinnery and H. Jamieson, "Equivalent circuits for discontinuities in transmission lines," *Proceedings of the IRE*, vol. 32, no. 2, pp. 98–114, Feb. 1944.

[21] J. Whinnery, H. Jamieson, and T. Robbins, "Coaxial-line disconti-
nuities," *Proceedings of the IRE*, vol. 32, no. 11, pp. 695–709, Nov.
1944.

[22] T. Moreno, *Microwave transmission design*. Norwood, USA: Artech
House INC., 1989.

[23] P. Somlo, "The computation of coaxial line step capacitance," *IEEE
Transactions on Microwave Theory and Techniques*, vol. 15, no. 1,
pp. 48–53, Jan. 1967.

[24] T. MacKenzie and A. Sanderson, "Some fundamental design prin-
ciples for the development of precision coaxial standards and com-
ponents," *IEEE Transactions on Microwave Theory and Techniques*,
vol. 14, no. 1, pp. 29–39, Jan. 1966.

[25] W. K. Gwarek, "Computer-aided analysis of arbitrarily shaped coax-
ial discontinuities," *IEEE Transactions on Microwave Theory and
Techniques*, vol. 36, no. 2, pp. 337–342, Feb. 1988.

[26] G. M. Wilkins, J.-F. Lee, and R. Mittra, "Numerical modeling of
axisymmetric coaxial waveguide discontinuities," *IEEE Transactions
on Microwave Theory and Techniques*, vol. 39, no. 8, pp. 1323–1328,
Aug. 1991.

[27] B. Szendrenyi, "Effects of pin depth in LCP 3.5mm 2.4mm and
1.00mm connectors," in *IEEE MTT-S International Microwave Sym-
posium Digest*, vol. 3, June 2000, pp. 1859–1862.

[28] *Standard for precision coaxial connectors DC to 110 GHz, IEEE
P287*, IEEE Instrumentation and Measurement Society, Sep. 2007.

[29] (2009) Connector reference list. [Online]. Avail-
able: http://www.metas.ch/root_legnet/Web/Fachbereiche/
Elektrizitaet/PDFFiles/217/ConnectorBibliography1.8.pdf

[30] J. Hoffmann, P. Leuchtmann, and R. Vahldieck, "Pin gap investi-
gations for the 1.85 mm coaxial connector," in *Proceedings European
Microwave Conference*, Oct. 2007, pp. 388–391.

[31] K. Wong, "Private communication," 2006.

[32] K. H. Wong, "Characterization of calibration standards by physical measurements," in *ARFTG Conference Digest*, vol. 39, June 1992, pp. 53–62.

[33] J. Hoffmann, P. Leuchtmann, and R. Vahldieck, "Over-determined offset short calibration of a VNA," in *ARFTG Conference Digest*, vol. 71, June 2008.

[34] G. F. Engen and C. A. Hoer, "Thru-reflect-line: An improved technique for calibrating the dual six-port automatic network analyzer," *IEEE Transactions on Microwave Theory and Techniques*, vol. 27, no. 12, pp. 987–993, Dec. 1979.

[35] R. F. Baur and P. Penfield, "De-embedding and unterminating," *IEEE Transactions on Microwave Theory and Techniques*, vol. 22, no. 3, pp. 282–288, Mar. 1974.

[36] G. F. Engen, "A least squares solution for use in the six-port measurement technique," *IEEE Transactions on Microwave Theory and Techniques*, vol. 28, no. 12, pp. 1473–1477, Dec. 1980.

[37] S. P. Jachim and W. D. Gutscher, "A statistical method for calibrating the six-port reflectometer using nonideal standards," *IEEE Transactions on Microwave Theory and Techniques*, vol. 37, no. 11, pp. 1825–1828, Nov. 1989.

[38] D. F. Williams, C. M. Wang, and U. Arz, "An optimal multiline TRL calibration algorithm," in *IEEE MTT-S International Microwave Symposium Digest*, vol. 3, June 2003, pp. 1819–1822.

[39] D. F. Williams, J. C. M. Wang, and U. Arz, "An optimal vector-network-analyzer calibration algorithm," *IEEE Transactions on Microwave Theory and Techniques*, vol. 51, no. 12, pp. 2391–2401, Dec. 2003.

[40] J. Hoffmann, P. Leuchtmann, J.Ruefenacht, and R. Vahldieck, "A stable bayesian vector network analyzer calibration algorithm," *IEEE Transactions on Microwave Theory and Techniques*, vol. 57, no. 4, pp. 869–880, Apr. 2009.

[41] D. Rasch, *Mathematische Statistik. Eine Einführung für Studenten der Mathematik, Statistik und Naturwissenschaften.* Heidelberg, Germany: Johann Ambrosius Barth Verlag, 1995, ch. 6 Funktionen und Folgen von zufälligen Variablen, p. 177.

[42] (2006) Agilent AN-154 S-parameter design. [Online]. Available: http://cp.literature.agilent.com/litweb/pdf/5952-1087.pdf

[43] J. B. Scott, "Investigation of a method to improve VNA calibration in planar dispersive media through adding an asymmetrical reciprocal device," *IEEE Transactions on Microwave Theory and Techniques*, vol. 53, no. 9, pp. 3007–3013, Sept. 2005.

[44] T. Jamneala, D. A. Feld, and B. Zaini, "Network analyzer calibration employing reciprocity of a device," U.S. Patent 7 064 555, Jun 20, 2006.

[45] D. Rasch, *Mathematische Statistik. Eine Einführung für Studenten der Mathematik, Statistik und Naturwissenschaften.* Heidelberg, Germany: Johann Ambrosius Barth Verlag, 1995, ch. 9 Punktschätzung, pp. 267–277.

[46] J. Nocedal and S. J. Wright, *Numerical Optimization.* New York, USA: Springer, 2006, ch. 1 Introduction, pp. 6–9.

[47] ——, *Numerical Optimization.* New York, USA: Springer, 2006, ch. 15 Fundamentals of Algorithms for Nonlinear Constrained Optimization, pp. 421–447.

[48] C.Robert and G. Casella, *Monte Carlo Statistical Methods.* New York, USA: Springer, 2004, ch. 2 Random Variable Generation, pp. 47–57.

[49] U. Stumper, "Uncertainty of VNA S-parameter measurement due to nonideal TRL calibration items," *IEEE Transactions on Instrumentation and Measurement*, vol. 54, no. 2, pp. 676–679, Apr. 2005.

[50] *Evaluation of measurement data — Guide to the expression of uncertainty in measurement*, Joint Committee for Guides in Metrology, Sep. 2008.

[51] *R: A language and environment for statistical computing*, R Foundation for Statistical Computing, 2005.

[52] J. Hoffmann, P. Leuchtmann, J. Schaub, and R. Vahldieck, "Computing uncertainties of S-parameters by means of monte carlo simulation," in *ARFTG Conference Digest*, vol. 69, June 2007.

[53] (2006) Agilent 8510-13 measuring noninsertable devices product note. [Online]. Available: http://cp.literature.agilent.com/litweb/pdf/5956-4373E.pdf

[54] W. Daywitt and G. Counas, "Measuring adapter efficiency using a sliding short circuit," *IEEE Transactions on Microwave Theory and Techniques*, vol. 38, no. 3, pp. 231–237, Mar. 1990.

[55] J. Randa, W. Wiatr, and R. L. Billinger, "Comparison of adapter characterization methods," *IEEE Transactions on Microwave Theory and Techniques*, vol. 47, no. 12, pp. 2613–2620, Dec. 1999.

[56] J. Hoffmann, P. Leuchtmann, A. Kretz, J. Ruefenacht, and R. Vahldieck, "Characterization of coaxial adapters for s-parameter measurements," in *Proceedings European Microwave Conference*, Oct. 2008, pp. 313–316.

[57] (2007) Agilent PNA microwave network analyzers data sheet. [Online]. Available: http://cp.literature.agilent.com/litweb/pdf/5988-7988EN.pdf

[58] I. Gradshteyn and I. Ryzhik, *Table of Integrals, Series, and Products*, A. Jeffrey, Ed. New York, USA: Academic Press, Inc, 1965.

[59] S. G. Samko, A. A. Kilbas, and O. I. Marichev, *Fractional Integrals and Derivatives*. Yverdon, Switzerland: Gordon and Breach, 1993, ch. 1 Fractional Integrals and Derivatives on an Interval, p. 9.

List of Symbols

Symbol	Description	Unit
α	angle	[1]
$\mathbb{A}$	set of errors of VNA and standards	[1]
a	outer radius of center conductor	[m]
a	transmission parameter	[1]
a	forward mode amplitude	[1]
A	complex constant	[1]
$\mathbf{A}$	coefficient matrix	[1]
β	complex angle	[1]
b	inner radius of outer conductor	[m]
b	reflection parameter	[1]
b	backward mode amplitude	[1]
B	complex constant	[1]
$\mathbb{C}$	complex numbers	[1]
c	velocity of light in free space	[m/s]
c	reflection parameter	[1]
csw	slot width for capacity computation	[m]
cs	finger shift for capacity computation	[m]
cd	finger diameter for capacity computation	[m]
cx	coordinate in slotted section	[m]
C	capacitance	$[1/\Omega \text{ s}]$
C'	capacitance per meter	$[1/\Omega \text{ s m}]$
δ	skin depth	[m]
Δ	derivative of error	[1]
d	distance	[m]
d	complex surface displacement	[m]

Symbol	Description	Unit
d	diameter	[m]
dh	hole diameter	[m]
dr	equivalent inner diameter	[m]
dc	center conductor diameter	[m]
dm	male pin diameter	[m]
η	least squares error	[1]
ϵ	real permittivity	[As/Vm]
$\underline{\epsilon}$	complex permittivity	[As/Vm]
$\vec{E}$	complex electric field vector	[V/m]
E	complex error	[1]
$E()$	estimator	[1]
f	frequency	[1/s]
fi	female inner chamfer	[m]
fo	female outer chamfer	[m]
$\vec{F}$	complex electromagnetic field vector	
F_0	real constant	[1]
γ	propagation constant	[1/m]
Γ	reflection coefficient	[1]
$\Gamma()$	Gamma function	[1]
$g()$	system function of VNA	[1]
$g'()$	system function of VNA for all standards	[1]
G	conductivity	[S]
G'	conductivity per meter	[S / m]
$G()$	inverted system function of VNA	[1]
h	roughness amplitude	[m]
h	transversal wave number	[1/m]
$\vec{H}$	complex magnetic field vector	[A/m]
$H^{(1)}()$	Hankel function of first kind	[1]
$H^{(2)}()$	Hankel function of second kind	[1]
I	current	[A]

Symbol	Description	Unit
j	imaginary unit	[j]
J_n	n-th Bessel function	[1]
k	integer number	[1]
k	wave number	[1/m]
l	integer number	[1]
l	length	[m]
L	inductance	[Ω/s]
L'	inductance per meter	[Ω/s m]
L_M	location of local maximum	[1]
L_{xxx}	random length variable	[m]
μ	mean value	[1]
μ	permeability	[Vs/Am]
m	integer number	[1]
mi	male inner chamfer	[m]
mo	male outer chamfer	[m]
n	integer number	[1]
$N(\mu, \sigma^2)$	Gaussian distribution	[1]
N	integer number	[1]
ω	radial frequency	[1/s]
π	Pi	[1]
ϕ	angle	[1]
∂	boundary	
$p()$	probability density function	[1]
p	period	[m]
pg	pin gap	[m]
P	power	[W]
q	integer number	[1]
q_n	polynomial factors	[1]
r	radius	[m]
r	stable raw S-parameters	[1]

Symbol	Description	Unit
r'	stable raw S-parameters of all standards	[1]
$\tilde{r}$	true raw S-parameters	[1]
R	resistance	[Ω]
R'	resistance per meter	[Ω/m]
R_{xxx}	random reflection variable	[1]
σ	variance	[1]
σ	conductivity	[S/m]
s	S-parameters of standard	[1]
s'	S-parameters of all standards	[1]
$\tilde{s}$	true S-parameters of standard	[1]
s'_d	known S-parameters of standards	[1]
$\bar{s}'_u$	estimate of standards' parameters	[1]
s'_u	unknown parameters of standards	
sl	slot length	[m]
sw	slot width	[m]
$\mathbf{S}$	S-matrix	[1]
S	S-parameter	[1]
$S()$	S-parameter function of standard	[1]
S	port plane	
$\mathbf{T}$	transmission matrix	[1]
U	voltage	[V]
$U_{v,s'}$	set of uncertainties	
$\mathbf{U}$	diagonal matrix	[1]
v	stable VNA parameters	[1]
$\bar{v}$	estimate of VNA parameters	[1]
$\tilde{v}$	true VNA parameters	[1]
var	variance	[1]
x	x-coordinate	[m]
$\vec{X}$	residual electromagnetic field	
y	y-coordinate	[m]

Symbol	Description	Unit
Y'	admittance per meter	[S/ m]
z	z-coordinate	[m]
Z_0	characteristic impedance	[Ω]
Z	linear combination of Hankel functions	[1]
Z'	impedance per meter	[Ω/m]
Z_s	surface impedance	[Ω]
Z	characteristic free space impedance	[Ω]
$\mathbf{Z}$	Impedance matrix	[Ω]
$\mathbf{Z}_{ref}$	Reference impedance matrix	[Ω]

List of Publications

Journal papers

P1 J. Hoffmann, P. Leuchtmann, J. Ruefenacht and R. Vahldieck, "A Stable Bayesian Vector Network Analyzer Calibration Algorithm," *IEEE Transactions on Microwave Theory and Techniques*, vol. 57, no. 4, pp. 869–880, Apr. 2009.

P2 J. Hoffmann, P. Leuchtmann, J. Ruefenacht and C. Hafner, "Propagation Constant of a Coaxial Transmission Line with Rough Surfaces," *IEEE Transactions on Microwave Theory and Techniques*, accepted.

Conference papers

P3 J. Hoffmann, P. Leuchtmann, J. Schaub and R. Vahldieck, "Computing Uncertainties of S-Parameters by Means of Monte Carlo Simulation," in *ARFTG Conference Digest*, vol. 69, Jun. 2007.

P4 J. Hoffmann, P. Leuchtmann and R. Vahldieck, "Pin Gap Investigations for the 1.85 mm Coaxial Connector," in *Proceedings European Microwave Conference*, pp. 388–391, Oct. 2007.

P5 ——, "Over-Determined Offset Short Calibration of a VNA," in *ARFTG Conference Digest*, vol. 71, Jun. 2008.

P6 J. Hoffmann, P. Leuchtmann, A. Kretz, J. Ruefenacht and R. Vahldieck, "Characterization of Coaxial Adapters for S-parameter Measurements," in *Proceedings European Microwave Conference*, pp. 313–316, Oct. 2008

Conference papers continued

P7 C. Boecklin, T. Kaufmann, J. Hoffmann, C. Fumeaux, R. Vahldieck, "Simulation of Corrugated Coaxial Cables using the Meshless Radial Point Interpolation Time-Domain Method," in *20th Int. Zurich Symposium on EMC Zurich 2009*, p. 3740, Jan 2009.

P8 J. Hoffmann, C. Hafner, P. Leidenberger, J. Hesselbarth, S. Burger, "Comparison of electromagnetic field solvers for the 3D analysis of plasmonic nano antennas," in *SPIE Proceedings*, pp. 73900J-73900J-11, Jun 2009.

Curriculum Vitae

Personal data

Name:	Johannes Hoffmann
Nationality:	German
Date of birth:	August 31, 1978
E-mail:	hoffmanj@ifh.ee.ethz.ch

Work and Academic Experience

08/2005 – present: **ETH Zürich**, Zürich, Switzerland
Laboratory for Electromagnetic Fields and Microwave Electronics
Teaching and Research Assistant

08/2004 – 05/2005: **Schlumberger**, Paris, France
Internship + Thesis: Contactless Energy Transmission

06/2000 – 08/2000: **Robert Bosch GmbH**, Feuerbach, Germany
Internship

09/1998 – 09/1999: **Behindertenwerkstätten Nagold**
Civil Service

Education

08/2005 – present: **ETH Zürich**, Zürich, Switzerland
Laboratory for Electromagnetic Fields and Microwave Electronics
Doctorate in Electrical Engineering

09/2003 – 05/2005: **École Nationale Supérieure des Télécommunications**, Paris, France
Double diploma programme

09/1999 – 09/2003: **University of Stuttgart**, Stuttgart, Germany
Diploma Studies of Electrical Engineering

09/1995 – 09/1998: **Technisches Gymnasium Nagold**, Nagold, Germany
High School